In presenting this thesis in partial fulfillment of the requirements for an advanced degree at Idaho State University, I agree that the Library shall make it freely available for inspection. I further state that permission for extensive copying of my thesis for scholarly purposes may be granted by the Dean of the Graduate School, Dean of my academic division, or by the University Librarian. It is understood that any copying or publication of this thesis for financial gain shall not be allowed without my written permission.

Signature ________________________

Date ____________________________

OPTIMIZATION OF ^{67}CU PRODUCTION FOR AN ELECTRON LINAC

by

Bindu KC

A dissertation
submitted in partial fulfillment
of the requirements for the degree of
Doctor of Philosophy in the Department of Physics
Idaho State University
Summer 2015

To the Graduate Faculty:

The members of the committee appointed to examine the dissertation of Bindu KC find it satisfactory and recommend that it be accepted.

Mahbub Khandaker,
Major Advisor

Douglas Wells,
Co-Advisor

Valeriia Starovoitova,
Co-Advisor

Daniel Dale,
Committee Member

George Imel,
Graduate Faculty Representative

I lovingly dedicate this dissertation to my family for their constant support and unconditional love.

Acknowledgments

First, I would like to thank my original major advisor, and now co-advisor, Dr. Douglas Wells for offering his input, guidance, and continuous help throughout my years of study. Despite the fact that he moved to another university, he managed to take some time out of his busy schedule and provided me distance guidance. He has been extremely supportive and has provided insightful discussions about the research.

I express my deepest gratitude to my major advisor Dr. Mahbub Khandaker for his immense assistance and guidance since taking on the task of being my local advisor. Discussions with him were invaluable and inspiring.

This work would not have been possible without the help, support, and encouragement of my co-advisor, Dr. Valeriia Starovoitova. I have learned many things both personally and professionally working under her guidance. I am grateful for her scientific advice and suggestions to help me in finding the necessary literature and patiently incorporating it into the writing of this thesis.

My gratitude also goes to my committee members, Dr. Daniel Dale and my graduate faculty representative, Dr. George Imel for their contributions to this dissertation.

During my time as a graduate student I have had tremendous assistance from a number of people. I could not have done most of my irradiation experiments without Jon Stoner. He provided great mentorship through all experiments and data analysis during my graduate research. Dr. Frank Harmon always had answers for my every science question. Dr. Khalid Chouffani helped me in understanding the electronics

of the radiation detection system I used, for my experiments.

All the staff and engineers at the Idaho Accelerator Center including Mike Smith, Tim Gardner, Mark Balzer, Kevin Folkman, Brian Berls, Chad O'Neill, John Ralph, Linda Egli, Reena Spradlin and JeNeal Dalley have always helped in various ways to move this project forward.

I would also like to acknowledge the help I received from my good friends and former students of Idaho State University Dr. Vakhtang Makarashvilli, Dr. Lali Tchelidge and Dr. Zaijing Sun. Thank you my wonderful friends Jasen, Olga, Roman, Mayir, Jack, Lisa, Nino and too many to include here, for providing support and friendship that I needed.

I am eternally grateful to my family: my parents Krishna and Bijaya K.C. for their endless love and support, my soul-mate and husband, Bibek Gautam, who has faith in me and my intellect and has stood by my side during my good times and bad times, my son Avighna Gautam, who brought smile to my face even when I was irritated and depressed, my siblings and in-laws who always believed in my dream and have been supportive and caring. I would like to take this opportunity to offer special thanks to my parents-in-law who are taking care of my little one back home while I work to fulfill my dream. My family is my world. Thank you all for making my world beautiful.

Contents

List of Figures

List of Tables

Thesis advisor
Mahbub Khandaker

Author
Bindu KC

Optimization of ^{67}Cu Production for an electron LINAC

Abstract

With the dynamic growth of radioimmunotherapy in cancer treatment, the demand for suitable alpha- and beta-emitting isotopes has significantly increased. ^{67}Cu is one of the best suited radioisotopes for immunotherapy due to its convenient half-life and beta energies. Gamma radiation from this radioisotope is widely acknowledged as potentially useful for Single Photon Emission Computed Tomography (SPECT). Despite its high potential in nuclear medicine, the lack of a reliable and steady supply has limited clinical trials.

We studied the photo-proton production of ^{67}Cu via ^{68}Zn(γ, p)^{67}Cu reaction using a photon beam from an electron linear accelerator at the Idaho Accelerator Center. Several parameters were investigated to maximize the ^{67}Cu yield including several electron beam parameters and the design and materials of the end station (an integrated converter and target unit). In particular, the optimum electron beam energy and current were found, the optimum converter design was developed, and an optimum zinc target shape was identified to maximize the specific activity of ^{67}Cu. The optimized ^{67}Cu yield was calculated to be 16 μCi/(g·kW·hr). Numerous experiments demonstrated that the measured ^{67}Cu activity is in good agreement with the predictions. Comparisons of these results with the results of other laboratories were conducted. Several possible issues using high power electron beams were investigated. Specifically, energy deposition into the bremsstrahlung converter and photo-production target was evaluated and the consequences on target heating were calculated and experimentally verified. In addition, radiolytic corrosion of various materials in the high radiation field was also studied via photon activation analysis.

Chapter 1

Introduction

1.1 Radionuclides in Nuclear Medicine

Nuclei of elements having the same number of protons but different masses due to different numbers of neutrons are called isotopes. Among over 2000 known isotopes [1], some isotopes are stable, but most are unstable and decay in the form of particle (α, β, n, fission fragments...) emission or electromagnetic radiation (γ). Unstable isotopes are referred to as “radioisotopes.” On earth some radioisotopes occur naturally, while others are produced artificially. Half-lives for various radioisotopes can range from a very small fraction of a second (for example, $\sim 10^{-23}$ sec for ^{7}H) to extremely long (for example $\sim 10^{24}$ years for ^{128}Te) [2].

Radioisotopes have numerous applications in nuclear medicine, agriculture, industry, homeland security, and fundamental research. Due to their widespread applications, the demand for radioisotopes is large and continues to grow with the identification of new uses.

Nuclear medicine is a branch of medicine that uses radiation to diagnose and treat a variety of conditions, including many types of cancers, heart diseases, and other disorders. The beginning of nuclear medicine dates back to 1924, when George de Hevesy, J.A. Christiansen and Sven Lomholt performed the first radiotracer studies in animals using Pb-210 and Bi-210. The first use of radiotracers on humans was done by Herman Blumgart and Otto Yens using Bi-214 to study blood circulation in patients. John Lawrence, in 1936, recognized the possibility of using radionuclides for cancer treatment by administering P-32 to treat a patient with leukemia [3]. In 1937, Joseph Gilbert Hamilton performed the first medical physiology study of the dynamics of sodium transport in the body [4]. Later, both diagnostic and therapeutic nuclear medicine progressed rapidly with the discovery of I-131, Tc-99m, Ir-192, and other radioisotopes.

Today, the majority (about 90%) of medical procedures involving the use of radioisotopes are diagnostic, while about 10% are therapeutic. Over 10,000 hospitals worldwide perform tens of millions of procedures per year, and this number is growing at about 10% annually [5].

Diagnostic or imaging techniques in nuclear medicine use either gamma- or positron-emitters. These radioactive tracers are usually short-lived nuclides linked to chemical compounds, forming radiopharmaceuticals. Various radiopharmaceuticals are used for imaging different functions of a variety of organs and tissues. Gamma rays emitted either directly by radioisotopes or as a result of positron-electron annihilation are detected by a “gamma camera,” which can take images from many different angles. By observing the radioisotope distribution in an organ, information is provided about the organ function.

The most common type of nuclear medical imaging is Single Photon Emission Computed Tomography (SPECT). This technique uses gamma rays directly emitted by a radiopharmaceutical. During SPECT scans, a gamma camera acquires multiple 2-D images of an organ from numerous angles. 3-D reconstruction from 2-D projections results in a complete organ image for reliable and accurate diagnosis. Radionuclides used for SPECT should emit gamma rays of sufficient energy to escape the body and be detected by commercial detectors. At the same time, they have to have a short enough half-life to decay soon after imaging is complete to minimize the dose received by the patient. The optimum SPECT-compatible radionuclides are γ-emitters with the energy range from 100 keV to 300 keV and half-lives in the range from a few hours to a few days [6].

Positron Emission Tomography (PET) is similar to SPECT in its use of radioactive tracers and detection of gamma rays. However, the tracers used for PET emit positrons, which in turn, annihilate with electrons causing two 511 keV photons to be emitted in opposite directions. A gamma camera detects these photons “coincident” in time and accurately locates the source of the positrons. Due to the different gamma energies, gamma camera detectors are often quite different for SPECT than for PET. Spatial resolution of PET diagnostics is significantly better ($\approx 5 - 7$ mm) than that of SPECT ($\approx 10 - 14$ mm) [6].

Application		Radionuclide	Half-Life	Decay	Target Organ
Diagnosis	PET	F-18	110 m	β^+	bone and breast cancer
		Ga-67	78 h	β^+	tumor imaging
		C-11	20 m	β^+	brain physiology
		Cu-64	12.7 h	β^+	genetic disease
		N-13	10 m	β^+	cardiac imaging
	SPECT	Tc-99m	6 h	γ	skeleton, heart, lungs, brain
		Lu-177	6.7 d	γ, β^-	lung, liver and breast cancer
		I-123	13 h	γ	thyroid cancer
		I-131	8 d	γ, β^-	thyroid cancer
		Tl-201	73 h	γ	coronary artery disease
Radiotherapy	Teletherapy	Co-60	5.3 y	γ, β^-	external beam therapy
		Cs-137	30 y	γ, β^-	external beam therapy
	Brachytherapy (seeds implantation)	Ir-192	74 d	β^-	cancer treatment
		Pd-103	17 d	β^-	prostrate therapy
	Brachytherapy (pharmaceuticals injection)	P-32	14 d	β^-	red blood cells
		Y-90	64 h	β^-	liver cancer
		I-131	8 h	γ, β^-	thyroid cancer
		Lu-177	6.7 d	γ, β^-	non-Hodgkin's lymphoma
		Bi-213	46 m	α	targeted alpha therapy

Table 1.1: List of some radionuclides commonly used in nuclear medicine [7].

Although the use of radioisotopes for therapy is less common than for diagnosis, it is nevertheless also widespread. According to the American Society for Therapeutic Radiology and Oncology (ASTRO), nearly two-thirds of all cancer patients receive radiation therapy during their treatment [8]. There are two branches of radiotherapy: teletherapy and brachytherapy.

Teletherapy is an external beam therapy, where the radiation is delivered from a source, either a radioactive source or an accelerator, outside the body. Depending upon tumor location, different energy and types of radiation are used for the teletherapy of cancer patients. Low energy beta radiation is used to treat skin cancers, whereas higher energy gamma radiation is required for deeper cancer treatment.

Brachytherapy, on the other hand, is an internal radiation therapy, where a radiation source is placed inside the patient's body, as close to the tumor as possible. Depending upon the methods of delivering radioisotopes to the body, brachytherapy may be classified into two types. Type I involves surgically implanting radioactive seeds or wires in the tumor area. The radioactive sources may or may not be taken out of the body, depending on their half-lives and the patient's condition. This technique is particularly effective for treating localized cancers such as breast or prostate cancers. Type II involves attaching radioisotopes to suitable biological carriers and injecting the radiopharmaceutical into patients. In both types, α or β^- emitting radionuclides are used due to their short mean free path in biological tissues and their high linear energy transfer [9]. Some commonly used medical radioisotopes are listed in Table 1.1.

1.2 ^{67}Cu Demand, Production, and Use

Copper has 29 known isotopes, of which 27 are radioactive. ^{67}Cu is among the longer-lived radioactive species with a half-life of 61.83 hours. It has 29 protons and 38 neutrons. The strongest gamma-lines from ^{67}Cu are 90 keV (7%), 93 keV (16%) and 185 keV (49%), of which the latter is suitable for imaging. ^{67}Cu also emits short range (maximum range in water $\sim$ 2.1 mm [10]) electrons with the mean energies of 51 keV (1%), 121 keV (57%), 154 keV(22%) and 189 keV (20%). When attached to peptides or monoclonal antibodies, these electrons have a sufficient range ($\sim$ few mm) to affect small tumors without damaging surrounding healthy tissues. Importantly, "pre-clinical and clinical studies have confirmed that ^{67}Cu is retained in tumors in greater amounts and for longer time than ^{131}I" [11] (which is currently the most common radionuclide used in radioimmunotherapy (RIT)), thus delivering greater radiation doses to the tumors. In addition, its moderate half-life results in lower systematic radiation doses received by the patient and working personnel, yet it is sufficient enough to allow relatively easy transportation of ^{67}Cu over fairly long distances.

^{67}Cu is one of the most attractive β^-/γ emitters with significant potential for application in both diagnostic and therapeutic nuclear medicine, or synchronized application of both. ^{67}Cu has shown exceptional results in studies of treatment of non-Hodgkin's lymphoma [12]. It could also be used to treat colorectal cancer, bladder cancer, arthritis and ovarian cancers. In addition, the energies of the gamma rays (91, 93, and 185 keV) that are produced by ^{67}Cu are suitable for SPECT diagnosis.

So far, ^{67}Cu availability has been too limited to support research or clinical use. In the 1990s, the Brookhaven Linac Isotope Producer (BLIP) at Brookhaven National Laboratory (BNL) and the Isotope Production Facility at the Los Alamos Neutron Science Center (LANSCE) at Los Alamos National Laboratory (LANL) produced ^{67}Cu by irradiation of zinc oxide (ZnO) using high-energy proton linear accelerators (linacs). Their production prior to 2001 was limited to 1 Ci/year. Demand was projected to increase from 10 Ci/year then to as much as 1000 Ci/year by 2020 [13]. These two laboratories could not meet the market demand because the linacs were scheduled for high-energy physics experiments and were not readily available for routine isotope production. Another ^{67}Cu producer, Trace Life Sciences, a commercial production facility in Texas, worked on ^{67}Cu radioisotope production and supply for seven years, starting from 2002, until the facility was shut down in 2009 due to serious safety and financial issues [14].

Multiple experiments involving irradiation of ^{68}Zn have been going on at BLIP with the goal of producing ^{67}Cu on a large scale, via the ^{68}Zn(p, 2p)^{67}Cu reaction. Investigation and development of photonuclear production of ^{67}Cu via ^{68}Zn(γ, p)^{67}Cu using electron linacs is also in progress at the Argonne National Laboratory (ANL) research group. So far, none of these facilities have succeeded in supplying high specific-activity ^{67}Cu regularly for clinical trials.

^{67}Cu is referred to as one of the high priority radioisotopes in the joint DOE-NSF Nuclear Science Advisory Committee (NSAC) report from 2009 [15] and is an ideal candidate for cancer therapy according to the Nuclear Energy Research Advisory

Council (NERAC) report also from 2009 [16]. While the properties of this isotope make it a highly promising candidate for radiotherapy, the lack of adequate supply has prevented its clinical trials. ^{67}Cu availability diminished even more after the shutdown of Trace Life Sciences. Thus, the demand for ^{67}Cu is high while the supply, as of today, is virtually non-existent.

^{67}Cu can be manufactured in several ways (see Table 1.2). The most commonly used method is proton activation of ^{68}Zn via ^{68}Zn(p, 2p)^{67}Cu, using a cyclotron or other proton accelerator. Alternatively, ^{67}Cu can be produced via the ^{67}Zn(n, p)^{67}Cu reaction. This route, however, requires a very high flux of fast neutrons, while nearly all nuclear reactors in the US have a thermal neutron spectrum. Moreover, nuclear reactors require extensive personnel and safety infrastructure to operate and have extremely high operating and decommissioning costs. Management of large amounts of radioactive waste is another crucial problem associated with nuclear reactors.

Proton accelerators, on the other hand, are powered by electricity rather than uranium fuel, and thus generate far less radioactive and hazardous waste. In general, such accelerators are comparatively inexpensive to build and to operate [17]; however, ^{67}Cu production requires highly energetic protons (more than 30 MeV), which substantially increases the cost. Also, the heat dissipation problem in any target associated with proton accelerators remains an issue which limits their current and, as a result, ^{67}Cu yield.

Photonuclear production of ^{67}Cu using linear accelerators is a promising alternative method to proton and neutron induced production methods. When high energy

Particle	Reaction	Peak cross section (σ), mb
p	^{68}Zn(p, 2p)^{67}Cu	6($E_P = 30...85$, MeV)
		24.8($E_P = 130...425$, MeV)
	^{70}Zn(p, α)^{67}Cu	15($E_P = 16$ MeV)
α	^{64}Ni(α, p)^{67}Cu	34($E_\alpha = 22$ MeV)
n	^{67}Zn(n, p)^{67}Cu	1.07($E_N = 1.5$ MeV)
γ	^{68}Zn(γ, p)^{67}Cu	11($E_\gamma = 22$ MeV)

Table 1.2: Main reactions for ^{67}Cu production [18]. Comparisons of the above listed production techniques based on cross sections are fundamentally misleading because each method is different in terms of physics and engineering limits and challenges (see explanation in text). For example, limitations in beam current/flux and target thicknesses are quite different for each technique.

photons are absorbed by a nucleus of the target material, the nucleus becomes excited and unstable. The unstable nucleus releases excess energy in the form of one or more particles $(n, p, \alpha, \beta, \gamma ...)$ and decays to a lower energy state. This process can be expressed as:

$$T + \gamma \rightarrow P + b, \tag{1.1}$$

where T represents the target nucleus, γ the incident radiation particle, a gamma ray, P the product nuclide, and b the emitted particle. The nuclear reaction representing the photo-production of ^{67}Cu thus can be expressed as:

$$^{68}Zn + \gamma \ \rightarrow \ ^{67}Cu + p \ . \tag{1.2}$$

The peak photonuclear reaction cross section is comparable to the peak cross section value of proton induced reactions as shown in Table 1.2 and Figure 1.1, and the photonuclear reaction occurs over a very broad energy range. Using electron linacs for the ^{67}Cu production is a convenient and relatively cheap method, which results in much less radioactive waste when compared to nuclear reactor techniques. Historically, photonuclear reactions have not been exploited for isotope production because of the low specific activity that is generally associated with this production process; however, the technique is well-known to be capable of the production of large quantities of certain radioisotopes [19, 20, 21, 22].

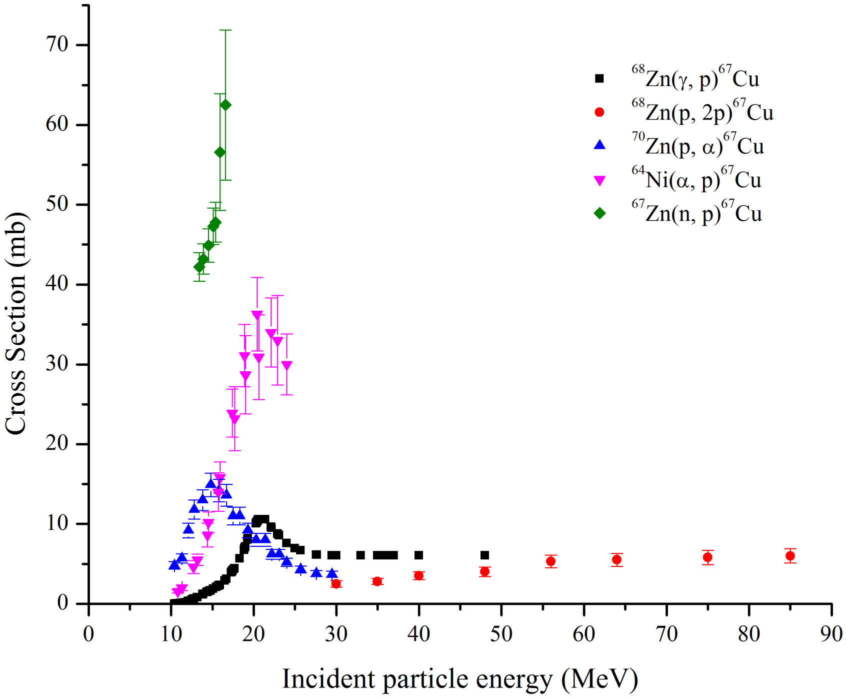

Figure 1.1: Comparison of cross sections for ^{68}Zn(p, 2p)^{67}Cu [23], ^{70}Zn(p, α)^{67}Cu [24], ^{64}Ni(α, p)^{67}Cu [25], ^{67}Zn(n, p)^{67}Cu [26], and ^{68}Zn(γ, p)^{67}Cu [27].

1.3 Specific Activity (SA) of Radioisotopes

The specific activity of a sample is defined as its activity per unit mass. Specific activity is expressed in Ci/gram or Bq/gram. It represents “radioactivity concentration,” and is one of the most important criteria of the quality of the radioisotopes that are prepared for medical procedures. When used as radiotracers or radio-therapeutic agents, radioisotopes are linked to bioconjugates, molecules that preferentially bind to cancer cells, for example peptides or antibodies. Due to the fact that cancer cells have a limited number of selective binding sites, an increase in impurity concentration may lead to blocking of these sites and, hence, to a reduction of selectivity [28]. Therefore, the radioisotopes that are prepared for labeling of bioconjugates should have high specific activity to minimize the interference of bioconjugates labeled with stable isotopes that provide no therapeutic value. The specific activity of a given sample is directly proportional to its activity (which, in turn, is proportional to the yield from the production process) and inversely proportional to its mass. To maximize the SA, one can:

- maximize the yield of the isotope of interest, or
- minimize the mass of other isotopes, both stable and unstable.
- exploit charged-particle reactions that enable chemical separation.

In any photon induced reaction, the yield of a radionuclide may be increased by increasing parameters that increase the production rate. The production rate density (transmutations per unit time per unit volume) of any reaction primarily depends on the photon flux, number of target nuclei, and reaction cross section (discussed in detail in Chapter 3). The reaction cross section for a particular reaction is governed by the nuclear structure of the target and daughter isotopes. Therefore, the energy-differential photon flux through the target and the target mass are the main parameters that can be changed to increase the yield of the photo-produced radionuclide.

The number of bremsstrahlung photons created and their energy-differential flux density, using a linear electron accelerator, depends on the electron beam parameters such as electron energy, beam current, beam divergence, and beam size. In addition, different converter materials have different electron to photon conversion efficiency [29]. Therefore, the design of the converter can also affect the photon flux. Finally, photon flux distribution through the target varies, so the size and shape of the target needs to be chosen carefully to maximize the integral flux and correspondingly the overall yield of the radioisotope.

Maximizing the beam current at a particular beam energy, and hence the power, helps maximize the yield; at the same time, it causes significant heat deposition in both the converter and the production target resulting in a temperature increase. This may lead to melting or even boiling of the target, converter, or setup components. Different water-cooling systems have been designed and used to remove the heat in linac targets. However, high radiation fields also induce additional problems, such as radiolysis of water, which promotes corrosion of target, converter, and beamline components.

1.4 Objectives

The purpose of this dissertation is to investigate the feasibility of the production of high specific activity ^{67}Cu via the ^{68}Zn(γ, p)^{67}Cu reaction. To achieve this purpose, the following objectives were completed and are addressed in this dissertation:

i) Find the optimum electron beam energy for photo-proton production of ^{67}Cu for the particular high-power electron linac used in the study, keeping in mind that electron beam energy affects the maximum beam current, and document the general techniques as it would apply to any electron linac;

ii) Optimize the bremsstrahlung converter (material and geometry) to maximize photon flux;

iii) Optimize the zinc photo-production target geometry to maximize photon flux through the target;

iv) Investigate high power issues, including:

- Energy deposition into the target and the consequent target heating
- Radiation induced radiolytic reactions

Having several interdependent parameters implies that optimization of one parameter, in turn, affects other parameters. Therefore, assessing “trade-offs” is necessary, rather than optimizing each parameter individually. Compromises have been made to achieve the best possible practical conditions for all afore mentioned issues.

Chapter 2

Theory

2.1 Photonuclear Reactions

Photonuclear reactions are reactions resulting from the absorption of photons by atomic nuclei. Typically, they are accompanied by emission of protons, neutrons, or a combination of these. The photo-absorption cross section, which is proportional to the reaction probability, depends on the incident photon energy. If the energy of the incoming photon is quite low, such as below a few MeV, the photon can only excite the nucleus into a low-energy single-particle or collective state that is below the particle emission threshold. The nucleus then returns back to the ground state by emitting gamma ray(s). If the photon energy is higher, about 10 to 30 MeV, nucleons might enter an excited state above the particle emission threshold. In that case, the nucleus may emit neutrons, protons, or both in addition to or instead of gamma rays. If the energy is very high (greater than 30 MeV), nucleon-nucleon exchange particles might participate in the excitation. Finally, above 140 MeV, nucleon excitation may occur, and mesons be produced. Photo-induced nuclear reaction theory can be better understood by looking at the absorption cross section in these four energy regions.

Region I: The Nuclear Resonance Fluorescence (NRF) Region ($E_\gamma \approx 0 - 8$ MeV)

For most nuclei, photons with energy below $\approx$ 8 MeV do not have sufficient energy to knock nucleons out. However, at certain discrete energies, the incident photon has just the right energy to excite a single nuclear level which can de-excite to its ground state by emitting gamma rays. The total absorption cross section in this region is represented by narrow resonance peaks known as Nuclear Resonance Fluorescence (NRF) peaks. Due to small peak width ($\leq$ eV) the integrated absorption cross section is low in this region [30].

Region II: The Giant Dipole Resonance (GDR) Region ($E_\gamma \approx 8 - 30$ MeV)

As the energy of the incoming photon increases, or equivalently the wavelength of the photon becomes smaller, the absorbed photon leads to collective excitation of many nucleons, with an excitation energy that is above the particle emission threshold. When the energy of the incident photon ranges from 8 to 30 MeV, the nucleus of a target atom typically responds to the excitation by a collective vibration of many nucleons giving rise to a broad resonance, the Giant Dipole Resonance (GDR) [30].

The GDR peak energy corresponds to the fundamental frequency for absorption of electric dipole radiation by the nucleus acting as a whole, and the GDR is qualitatively understood as the collective oscillation of neutrons against protons in the nucleus.

In the absence of exchange terms and velocity-dependent terms in the nuclear potential, the total integrated cross section is subjected to the Thomas-Reiche-Kuhn (TRK) sum rule [31] which is:

$$\int_0^\infty \sigma(E)dE = 60\frac{NZ}{A}\ \text{MeV}\cdot\text{mbarns}\ , \tag{2.1}$$

where N, Z, and A are respectively the neutron, atomic, and mass numbers.

The comparison of Eq. 2.1 with the experimentally obtained total integrated cross section shows that the electric giant dipole resonance makes the largest contribution to the total photon absorption cross section; while the contribution of other vibrational modes is generally small. The giant dipole resonance energy has an inverse relationship with the mass number of the nucleus [31]:

$$(E_0 \approx (40A^{-\frac{1}{3}}) + 7.5)\ \text{MeV}\ . \tag{2.2}$$

E_0 varies from about 24 MeV for ^{16}O to 13.5 MeV for ^{208}Pb.

In the semi-classical theory of the interaction of photons with nuclei, it is common to fit the cross section data with a Lorentz function [31]:

$$\sigma(E_\gamma) = \sigma_0\,\frac{E_\gamma^2\Gamma^2}{E_\gamma^2\Gamma^2 + (E_\gamma^2 - E_0^2)}\ , \tag{2.3}$$

where the Lorentz parameters E_0, σ_0, and Γ are the resonance energy, peak cross section, and full width at half maximum, respectively (see Figure 2.1). Γ varies between 4 and 8 MeV for medium and heavy nuclei.

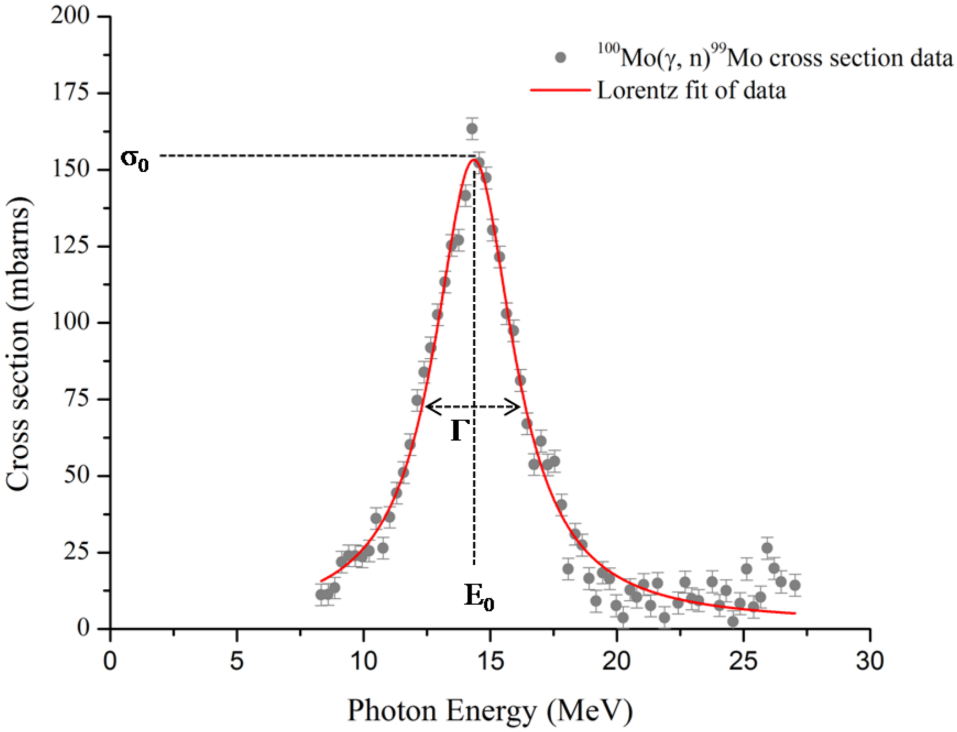

Figure 2.1: Cross section data−Lorentz fit for ^{100}Mo(γ, n)^{99}Mo [32].

After the photon is absorbed, the excited nucleus emits one or more neutrons, photons, and/or protons. Photo-absorption cross sections in the GDR region are relatively large (tens to hundreds of mbarns) and the resonance is quite wide (≈ 5 MeV) which is favorable for high transmutation yield.

Region III: Quasi-Deuteron (QD) Region ($E_\gamma \approx 30-140$ MeV)

A photon with energy above 30 MeV has a wavelength small enough (≈ 10 fm) to excite sub-nuclear structures. A photon's interaction with a neutron-proton pair (quasi-deuteron) inside the nucleus gives rise to direct emission of one or more nucleons (neutron or proton). This type of reaction is called Quasi-Deuteron Disintegration (QDD). The absorption cross section for QDD is low (few mbarns) as compared to the cross section in the GDR region, and can be found according to Levinger [33]:

$$\sigma_{QD} = L\frac{NZ}{A}\sigma_D(E_\gamma)\ , \tag{2.4}$$

where σ_{QD} is the Quasi Deuteron cross section, L is the Levinger factor, which varies smoothly as a function of atomic mass with L ≈ 6 in the mid-mass (A ≈ 60) region [34], N, Z, and A are neutron, atomic, and mass numbers, respectively, and σ_D is the photo-absorption cross section for deuteron.

Region IV: Photo-Meson Production (PMP) Region ($E_\gamma \geq 140$ MeV)

A photon with energy higher than 140 MeV (the rest mass of pion) has a very small wavelength (≈ 1 fm). Such high energy photons can excite single nucleons and produce π-mesons ($\pi^\pm$, π^0). Resonance-like structures are observed in the photo-absorption cross section in the energy range of 200 to 400 MeV. These resonances are called Baryon Resonances (BR) and this energy region is referred to as the Photo-Meson Production Region (PMPR). The total absorption cross section rises again due to this resonance-like photo meson production. A schematic representation of the total photo-absorption cross section showing the four different regions is shown in Figure 2.2.

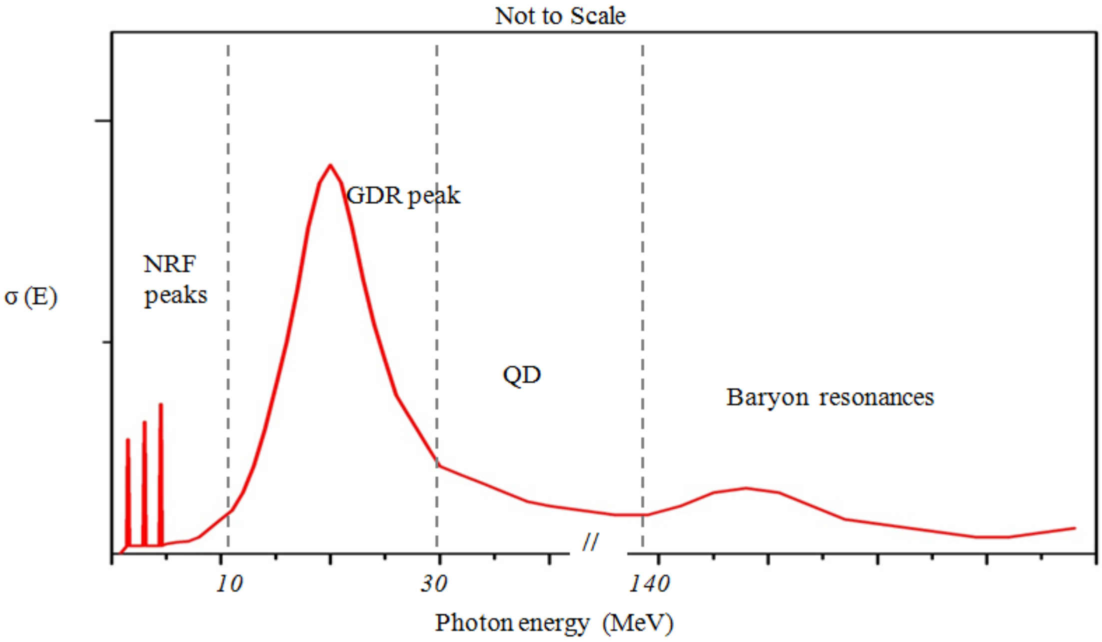

Figure 2.2: Schematic representation of photo-absorption cross section for different energy regimes. Y-axis is not to scale, to enable qualitative display of photonuclear reaction features for cross sections that range over many orders of magnitude, and for a very broad spectrum of nuclei.

2.2 Bremsstrahlung Converter

Bremsstrahlung (a German word for "braking radiation") is electromagnetic radiation produced by a high energy charged particle deflected (accelerated) in the electric field of another charged particle, such as an electron or an atomic nucleus. A bremsstrahlung "converter" is a material which produces bremsstrahlung when high energy electrons strike it, thereby, "convert" their energy into photons. Typically, converters are made from materials with high atomic number because the efficiency of bremsstrahlung conversion increases with the atomic number, proportional to Z^2 [35]. It also increases with the energy of the incident electron. To maximize transmutation rate, the bremsstrahlung converter should produce a maximum of high-energy bremsstrahlung photons above $\approx$ 10 MeV. A thick converter may be thick enough to stop high energy incident electrons and prevent the photo-production target from excessive heating by absorbing low energy electrons, which would otherwise deposit a large portion of their energy into the target and cause potentially damaging heating. If the converter is thin, only a small number of electrons will contribute to bremsstrahlung production, whereas the majority of the electrons of the electron beam pass through the converter material. Increasing the converter thickness increases the number of electrons interacting with converter nuclides and thereby increases the photon production. Further increase of the thickness will eventually decrease the photon flux, as it will be attenuated by the converter material. At the same time power deposition increases as the converter thickness increases. Therefore, it is important to optimize the converter thickness to maximize the bremsstrahlung efficiency, while minimizing the target heating.

2.3 Electron Beam Current–Energy Correlation

The number of electrons interacting with the converter for bremsstrahlung production is determined by the electron beam current and time of irradiation. Assuming that the electron beam energy and all other parameters are constant, radioisotope yield scales linearly with current. Thus, the highest possible beam current would result in the highest photon flux and the highest radioisotope yield. However, this is not the case for Radio Frequency (RF)-driven linear accelerators, or any accelerator. Energy from the RF field is converted to kinetic energy of accelerated electrons. Thus, conservation of energy requires that as the electron beam current increases, the RF electromagnetic field gradient must decrease. This process is called "beam loading," and results in a simple approximate relationship between electron beam energy and electron beam current:

$$E_T = E_0 - \pi I_{peak}\ \mathrm{MeV}\ , \tag{2.5}$$

where E_0 is the unloaded energy gain of accelerating electrons, E_T is the resultant energy gain due to the beam loading, and πI_{peak} represents energy reduced after beam loading, which is a product of accelerator total shunt impedance π and peak beam current I_{peak}.

The linear accelerator used in this study is composed of two 2856 MHz RF sections. The first section is a standing wave, side-coupled structure that bunches and

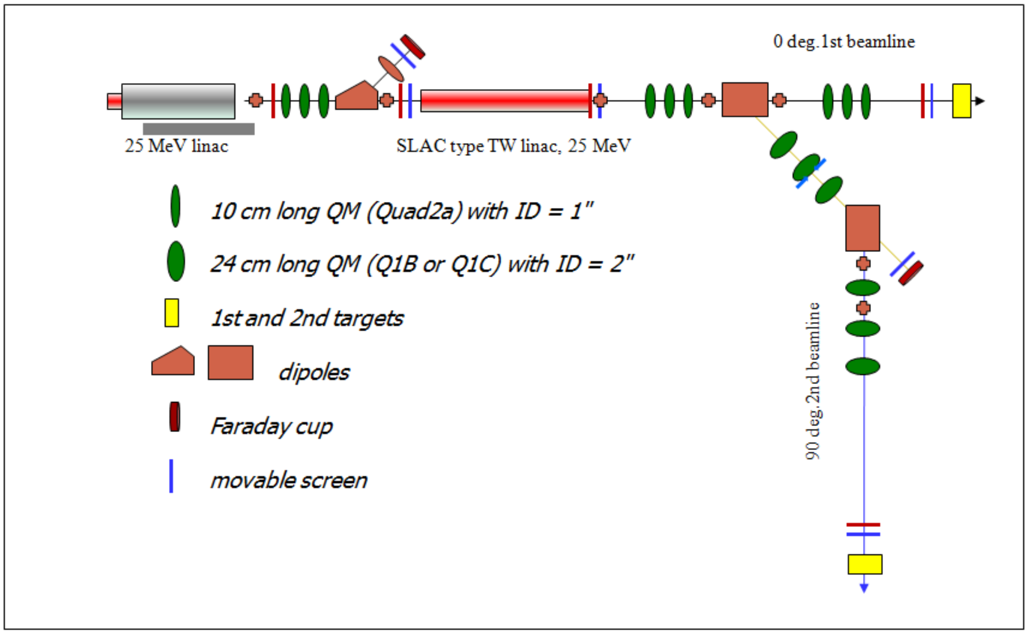

Figure 2.3: Layout of the linear accelerator used for the photonuclear production of radionuclides at the IAC. [Courtesy of Dr. Yu Jong Kim]

accelerates the beam to 25 MeV (unloaded) and injects it into the second section, which is a 25 MeV SLAC-type traveling wave accelerator. Each section is provided with microwave power from separate 5 MW peak-output klystrons. The schematic layout of the electron linear accelerator used in this study is shown in Figure 2.3. The total unloaded output energy is expected to be around 50 MeV, with an energy reduction of 0.118 MeV per mA of peak beam current after beam loading. The beam load function calculated from the measured characteristics of the accelerator guides is:

$$E_T = 52.3 - 118.3\, I_{peak}\ \text{MeV}\ . \tag{2.6}$$

Figure 2.4 shows the load line for the linear accelerator used in this study. When

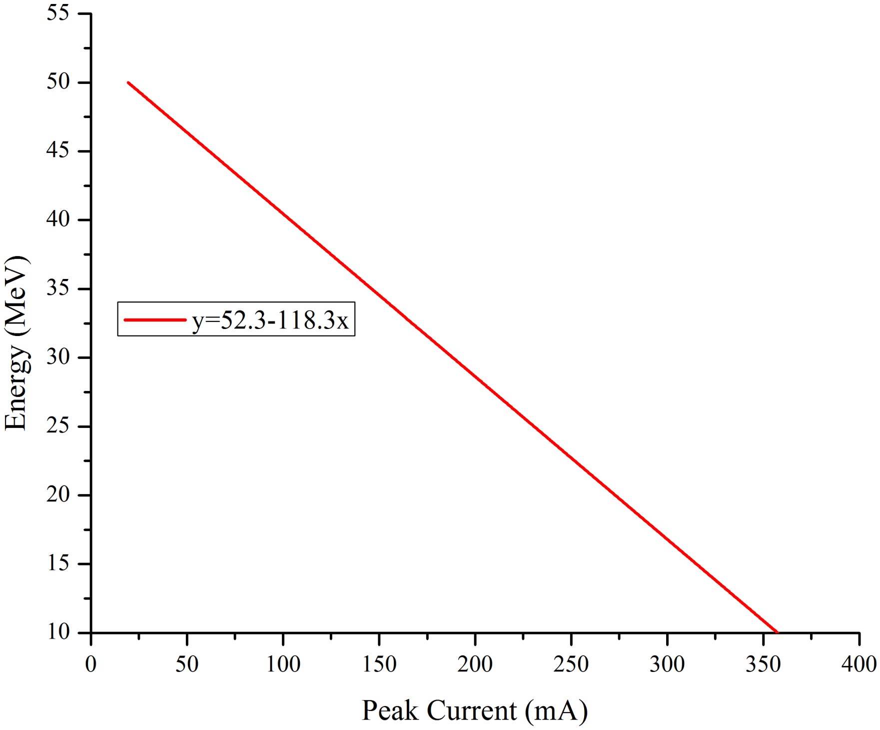

Figure 2.4: Load line plot for the electron linac with 5 MW RF input power to each acceleration section.

$I_{peak} \rightarrow I_{max}$, there are no photons of adequate energy to induce photonuclear reactions. Similarly, when $I_{peak} \rightarrow 0$, the proportion of photons above activation energy threshold is high, but there are so few photons that the activity induced is negligible. Thus, there is an optimum choice of current and beam energy to maximize transmutation rate and thus, maximize radioisotope production yield. These optimum values can be found by comparing the radionuclide yield for a variety of sets of beam energies and currents, while using the load-line constraints for the accelerator in question.

2.4 High Power Electron Beam Issues

2.4.1 Target Heating

A photo-production target is subjected to not only irradiation from photons of sufficient energy to cause nuclear conversion, but also to potential irradiation from primary and secondary electrons from the beam. Such a target has to deal with the power delivered by both incident electrons and photons. Since the radioisotope yield is proportional to the incident beam power for fixed energy, the power density from gammas and secondary electrons in the target must be maximized to increase the isotope production yield. At the same time, the target volume should be limited to keep the photon flux high within the target, which results in an increase of thermal power density. If the melting and boiling points of target materials are low, the target can melt or even boil relatively easily unless sufficient cooling is provided. Hence, the study and evaluation of the heat transfer mechanism between the target, the target holder, and the surrounding is crucial. An effective cooling system is absolutely necessary to avoid excessive target heating.

During irradiation the target will absorb power from the electrons and photon beams. For a given heat flux, the resulting temperature distribution in the target and target holder depends primarily on the thermal contact resistance between the target-holder interface [36], and the temperature of the surrounding cooling surface. The higher this resistance is, the larger the temperature drop will be from the target to the holder. In the case of materials metallurgically bonded to one another, the resistance is low, implying that heat can flow easily between the two.

The heat transfer mechanism from the target to the holder and to the surrounding flowing air involves three different components, namely: conduction, convection and radiation. Conduction in metals takes place largely due to the movement of free electrons through the lattice. The flow of internal energy from a region of higher temperature to a region of lower temperature is done by the interaction of the adjacent particles in the intervening space. The rate of heat transfer by conduction through a cylindrical wall for two metallic concentric cylinders can be calculated using Fourier's law of conduction:

$$\dot{Q}_{conduction} = \frac{2\pi L k (T_i - T_o)}{\ln \frac{r_o}{r_i}} \, , \tag{2.7}$$

where k is the thermal conductivity of a given material, L is length of the cylinders, r_i and r_o are inner and outer radii of the two concentric cylinders, and T_i and T_o are corresponding temperatures at inner and outer radii, respectively.

During the convection process, heat is transferred from one point to another by flowing gas or liquid as a result of macroscopic motion of the fluid. For a tube in contact with a flowing fluid, the heat flux is proportional to the temperature difference between the tube wall and bulk of the fluid as described by Newton's law of cooling:

$$\dot{Q}_{convection} = Ah(T_f - T_s) \, , \tag{2.8}$$

where $Q_{convection}$ represents heat transfer due to convection, and A is the area of the tube surface at temperature T_s in contact with the moving fluid at temperature T_f.

The convective heat transfer coefficient h strongly depends on the fluid properties, roughness of the solid surface, and the type of the fluid flow (laminar or turbulent). An important, but tricky part of the convection problem is to find the heat transfer coefficient for a given situation. For the majority of external forced convection problems, an empirical approach is employed. "In the empirical approach, a controlled laboratory experiment is performed, and the data are correlated in terms of the applicable dimensionless parameters" [37]. For example, the correlation may be of the form:

$$Nu = C(Re)^m(Pr)^n \, , \tag{2.9}$$

where Nu, Re, and Pr are dimensionless numbers known as the Nusselt, Reynolds, and Prandtl numbers, respectively, and C, m, and n are empirical constants. All the pertinent information−surface geometry, laminar or turbulent flow conditions, and coolant fluid properties are contained within the dimensionless parameters and they are constant in the correlation.

For a circular cylinder cross-flow, the average convective heat transfer coefficient is related to Nusselt number by the relation [38]:

$$\overline{h} = \frac{\overline{Nu}k}{D} \, , \tag{2.10}$$

where k is thermal conductivity of the fluid (coolant) at a given temperature and D is the diameter of the cylinder. The Nusselt number for turbulent flow is given by the Churchill and Bernstein equation [38]:

$$\overline{Nu} = 0.3 + \frac{0.62Re^{\frac{1}{2}}Pr^{\frac{1}{3}}}{[1+(\frac{0.4}{Pr})^{\frac{2}{3}}]^{\frac{1}{4}}}\left[1+\left(\frac{Re}{282000}\right)^{\frac{5}{8}}\right]^{\frac{4}{5}} . \tag{2.11}$$

Similarly, for a cylinder in cross-flow, the Reynolds number is defined by [38]:

$$Re = \frac{U_f D}{\nu} , \tag{2.12}$$

where U_f is the velocity and ν is the kinematic viscosity of the fluid.

Finally, the radiative heat transfer mechanism is the transfer of heat through electromagnetic waves. The amount of energy emitted depends strongly upon the absolute temperature of the radiator. The basic law of radiation derived by Stefan and Boltzmann gives the rate of heat transfer due to radiation [38]:

$$\dot{Q}_{radiative} = A\sigma\epsilon(T_h^4 - T_c^4) , \tag{2.13}$$

where A is the surface area of the radiator, σ is the Stefan Boltzmann constant ($\approx 5.67 \times 10^{-8} W m^{-2} K^{-4}$), and ϵ is the emissivity coefficient of the object ($0 < \epsilon < 1$ depending on the type of material and the temperature of the surface). T_h and T_c are the absolute temperatures of hot and cold (surrounding) surfaces.

2.4.2 Radiolysis of Water

Water is the most wide-spread coolant in numerous nuclear facilities due to its excellent heat transfer properties (high specific heat, low viscosity, easily pumped) and availability [39]. However, the interaction of energetic neutrons, charged particles or photons with water causes water molecules to be ionized or excited. As energetic particles deposit energy along tracks, a number of reactions occur and produce a variety of intermediate and stable water products. This phenomenon is known as radiolysis of water (see Figure 2.5).

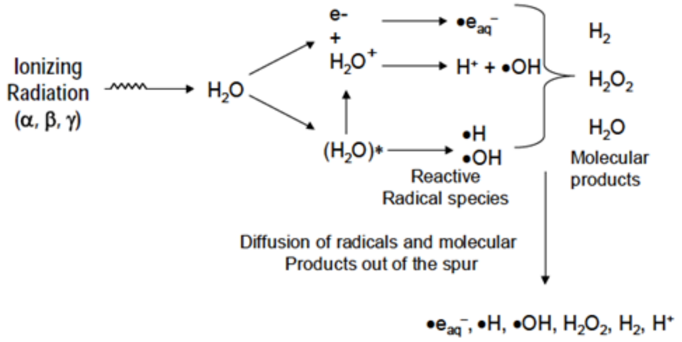

Figure 2.5: Steady state radiolysis of water product [40].

Radiolysis of water plays a crucial role in corrosive processes occurring at the liquid-solid interface in the presence of ionizing radiation. It acts as a corrosive agent. During the radiolysis, radical and stable products, such as: H_2, O_2, H_2O_2, $\cdot$OH, H, e^{-aq} (hydrated electron), HO_2, O_2^-, HO_2^-, OH^-, H^+ are formed [41]. The yields of these final products depend on the nature of the original energetic particle. These highly oxidizing (e.g., $\cdot$OH, H_2O_2) and highly reducing (e.g., e^{-aq}, O_2^-) products can significantly influence the corrosion kinetics. Corrosion may lead to a deterioration of functional properties of construction materials of a target or the target holder. Accelerator components, such as wave guides, electron beam windows, and bremsstrahlung converters are routinely cooled by water. The most common construction metals used in the accelerator components are aluminum, copper, tungsten, titanium, tantalum, and stainless steel. In a high radiation environment, water-cooling of these metals and alloys poses the risk of corrosion. The contamination of accelerator parts by radioactive corrosion products may cause serious damage during the operation of an accelerator. Corrosion may also lead to contamination of photonuclear production targets, thereby potentially affecting specific activity.

Chapter 3

Simulation and Experimental Methods

The process of simulation, method of experimental verification, and data acquisition will be discussed in this chapter. Monte Carlo simulations of radiation interactions with matter, including photonuclear reactions, to determine isotopic yields and the simulation of particle energy deposition were performed using a Monte Carlo particle transport code called MCNPX.

3.1 Monte Carlo N-Particle eXtended (MCNPX) Simulation

The Monte Carlo N-Particle eXtended (MCNPX) software developed at Los Alamos National Laboratory (LANL) is a radiation transport code that tracks almost all particles relevant to nuclear physics over a wide range of energies. The program tracks each of the particles from their creation and/or their elevated kinetic energy throughout their "life-time" until they are terminated (absorbed, escaped, etc.) or drop below energies capable of ionization. Probability distributions are randomly sampled to determine the outcome at each step. Due to its ability to handle complex geometries, flexible tally structures, extensive nuclear database for cross section data, and broad energy range, the code has been extensively used for modeling and simulation of nuclear physics processes and applications. Interactions of neutrons with matter are described in a range from 10^{-11} MeV to 20 MeV with data up to 150 MeV for some nuclides. Interactions of electrons with matter are described in a wide range from 1 keV to 1 GeV, and photonuclear processes are described for photons with energy from 1 keV to 100 GeV [42]. The program can be used in both single and coupled transport modes, for example, neutron mode or neutron-photon mode.

An MCNPX input file contains three groups of command lines called cards. The cards provide a description of the problem including the geometry (cell card and surface card), material description, source location and characteristics, and specification of desired tally types (data card). An example of an MCNPX input file is shown in Figure 3.1.

A cell is a three-dimensional object bounded by surfaces. The cell card has the format of the form: *j m d geom.*, where *j* is the cell number, *m* is the material number as specified in data card, *d* is the material density and *geom* is the geometry

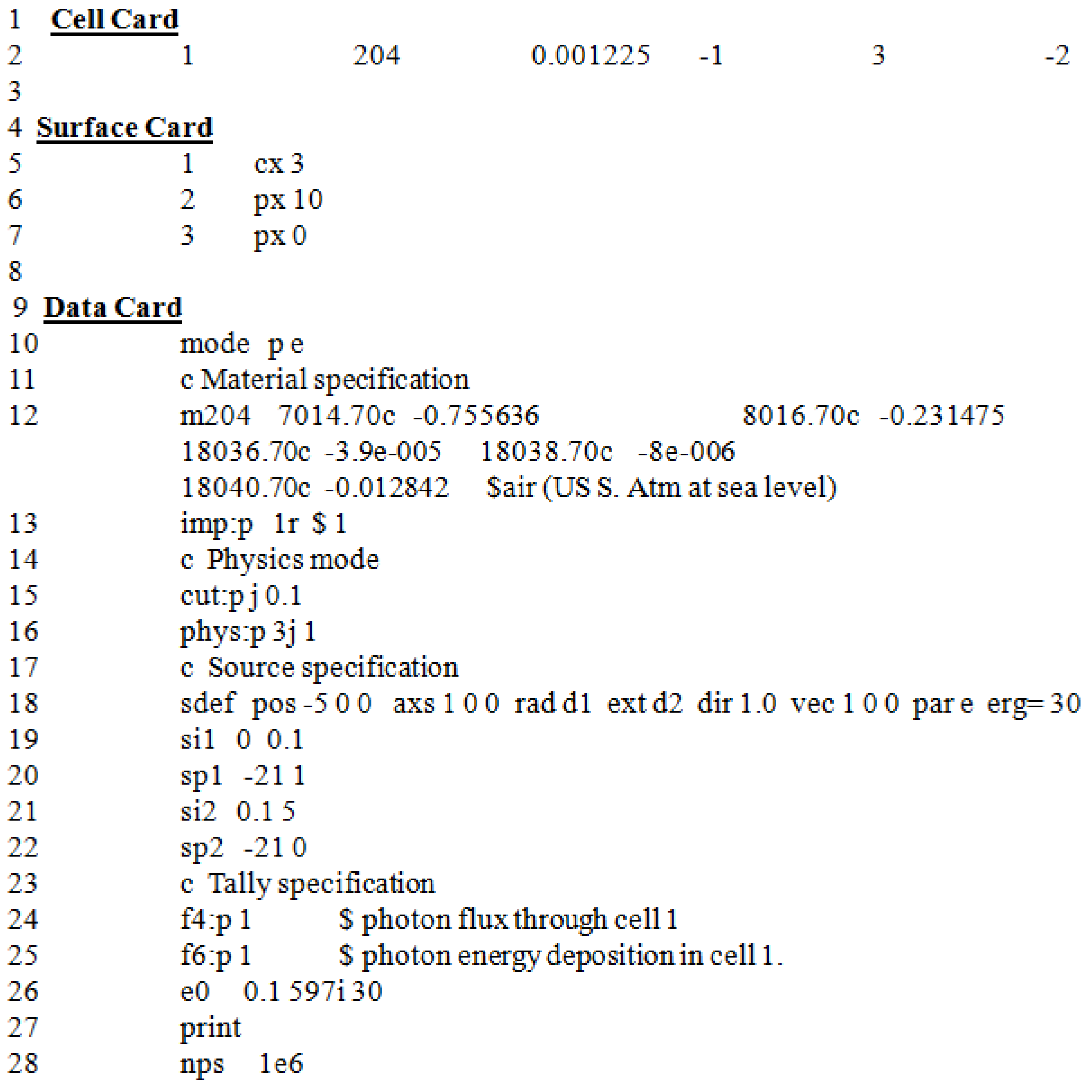

```
1  Cell Card
2             1          204          0.001225    -1          3          -2
3
4  Surface Card
5             1     cx 3
6             2     px 10
7             3     px 0
8
9  Data Card
10           mode  p e
11           c Material specification
12           m204   7014.70c  -0.755636                   8016.70c   -0.231475
             18036.70c  -3.9e-005     18038.70c    -8e-006
             18040.70c  -0.012842     $air (US S. Atm at sea level)
13           imp:p   1r  $ 1
14           c  Physics mode
15           cut:p j 0.1
16           phys:p 3j 1
17           c  Source specification
18           sdef  pos -5 0 0   axs 1 0 0  rad d1  ext d2  dir 1.0  vec 1 0 0  par e  erg= 30
19           si1   0  0.1
20           sp1   -21 1
21           si2   0.1 5
22           sp2   -21 0
23           c  Tally specification
24           f4:p 1          $ photon flux through cell 1
25           f6:p 1          $ photon energy deposition in cell 1.
26           e0    0.1 597i 30
27           print
28           nps     1e6
```

Figure 3.1: An MCNPX input file format.

specification (coming from the surface card), which consists of assigned surface numbers with Boolean operators (e.g., union, intersection, and complement) to specify different combinations of the surfaces. Lines 1−3 in Figure 3.1 represent a cell defined by surfaces 1, 2, and 3 in the surface card.

Surface cards are the parameters of surfaces that bound a cell. A surface card (lines 5 − 7 in Figure 3.1) has the format of the form: *j a list.*, where *j* is the surface number, *a* is the surface mnemonic (e.g., px−plane perpendicular to X-axis, cx−cylinder on the X-axis), and *list* represents the dimensions of the surface defined (in centimeters).

The data card is the core part of the MCNPX input file which specifies the problem to be simulated. General data card specifications are listed in Table 3.1. MCNPX can be run in several different modes depending upon the particles of interest. In the example shown in Figure 3.1, mode p e is used (line 10) meaning that only photons and electrons are considered in the simulation. All the simulations for this dissertation were run in photon-electron-neutron mode, since these are the particles of interest for the photonuclear production of isotopes. The material specification block gives the material number as specified in the material library, the atomic number, atomic mass and the weight/atomic fraction of each element in the material. Air (m204) is used as an example (line 12 in Figure 3.1) with atomic number, atomic mass, and weight

	MCNPX card name
1. mode,	MODE
2. cell and surface parameters,	IMP:N,P,E
3. energy physics cutoff,	PHYS
4. source specification,	SDEF
5. tally specification,	Fn, En
6. material specification, and	Mn
7. problem cutoffs.	NPS

Table 3.1: A description of data cards.

fraction of all its constituents. Cell parameters specify relative cell importances in the sample problem (line 13 in Figure 3.1). If the importance is zero in a certain cell, then the program terminates particles as soon as they reach this cell.

The physics card controls the physics aspect of the simulations. Different physics processes can be turned on and off depending on the problem. For example, we turned on all the electromagnetic processes including the photoelectric effect, Compton scattering, pair production, X-ray and bremsstrahlung production, secondary electron production, and coherent scattering. In addition to all of these, photonuclear physics was also turned on (line 16 in Figure 3.1). If the photonuclear reaction option is turned on, the photonuclear interaction table is accessed for cross section data but, in the case of the absence of such cross section data in the table, MCNPX uses nuclear models to calculate missing cross sections [43].

A source definition (SDEF) card is one of the four available methods to define a source in MCNPX. It defines the basic source parameters including particle type, particle energy, position and direction, time, and starting cell number. In the example shown in Figure 3.1, a monoenergetic beam of 30 MeV electrons is emitted along the X-axis. Source geometry is further described using source information (si) and source probability (sp) commands (lines $19 - 22$ in Figure 3.1). A complete list of MCNPX input files used in this work is presented in Appendix A.

Tally cards are used to specify the output of the MCNPX simulation. Various tallies (described in Table 3.2) related to particle current, particle flux, and energy deposition can be employed. The mesh tallies are also available for visualization purposes. Three-dimensional Rectangular/Cylindrical/Spherical (R/C/S) mesh needs to be defined and particle fluxes, dose rates, energy deposition, et cetera, can be tracked through the mesh. For example, the f4: p tally can be used to calculate an average photon flux through a cell, and the f1: p tally can be used to calculate the total number of photons striking a surface. Similarly, the f6: e tally can be used to compute the electron energy deposition into a cell. Likewise, rmesh1: p flux and rmesh3: p tallies can be used to compute photon flux and photon energy deposition in a rectangular mesh, respectively. The problem cutoff cards are used to specify parameters

Tally Mnemonic	Description
F1: N/P/E	Surface current
F2: N/P/E	Flux averaged over a surface
F4: N/P/E	Flux averaged over a cell
F5a: N/P	Flux at a point or ring detector
F6: N/P/NP	Energy deposition averaged over a cell
F7: N	Fission energy deposition averaged over a cell
F8: N/P/E	Energy distribution of pulses created in a detector
(R/C/S) MESH1: N/P/E	Average flux, fluence or current mesh tally
(R/C/S) MESH2: N/P/E	Source mesh tally
(R/C/S) MESH3: N/P/E	Energy deposition mesh tally
(R/C/S) MESH4: N/P/E	Point detector or DXTRAN mesh tally

Table 3.2: MCNP tallies [44].

to terminate execution of the MCNPX. Several different ways exist to terminate in

MCNPX, including energy cutoff, particle history cutoff, particle weight cutoff, and computer time cutoff. The energy cutoffs (line 15, Figure 3.1) and particle history (NPS) cutoffs (line 28, Figure 3.1) were utilized to minimize the run time in all the simulations for our work. For example, cut: p j 0.1 (line 15, Figure 3.1) signifies that MCNPX should terminate all the photons with energy below 0.1 MeV. Similarly, source particles history was limited to 10^6 so that the program stops after tracking 10^6 source electrons.

The output of MCNPX is a long text file, which includes a list of the input file, a "problem summary" of particle creation and loss, tallies and the output tables with relative errors. The statistical rigor of the MCNPX result may be quantified using the Figure of Merit (FOM), which is defined by Eq. 3.1 [45], where R is the tally relative error and T is the computing time:

$$FOM = \frac{1}{R^2T} \; . \tag{3.1}$$

Since $R^2 \propto \frac{1}{N}$, where N is the total number of histories, and $T \propto N$, for a well converged simulation, the FOM converges to a constant. MCNPX creates a tally fluctuation chart after each tally in the output file to provide the detailed information about the quality of the results. It has ten statistical tests which can be used to assess tally convergence, including the R, FOM, Variance of Variance (VOV), and slope as a function of the number of history runs. The tally result is statistically valid only if it passes all ten statistical tests.

3.2 Activity Calculation

During the process of irradiation, the number of product nuclei (N) is growing as the target nuclei are activated. However, because product nuclei are radioactive with a decay constant λ ($= \frac{\ln 2}{T_{1/2}}$), they also undergo radioactive decay at the same time, therefore causing N to decrease simultaneously. These two processes of production and decay compete with each other to determine N. The variation of the number of product nuclei is described by the differential equation:

$$\frac{dN}{dt} = R - \lambda N \, , \tag{3.2}$$

where R is the production rate of the product nuclei. At the beginning of irradiation, the number of product nuclei is presumably zero. With this initial condition, the solution of Eq. 3.2 is:

$$N(t) = \frac{R}{\lambda}(1 - e^{-\lambda t}) \, . \tag{3.3}$$

At the end of irradiation period t_i, the total number of product nuclei is:

$$N(t_i) = \frac{R}{\lambda}\,(1 - e^{-\lambda t_i}) \, . \tag{3.4}$$

The activity of the product nuclide at the end of irradiation is given as:

$$A(t_i) = \lambda N(t_i) = R\,(1 - e^{-\lambda t_i}) \, . \tag{3.5}$$

The production of product nuclide ends immediately with the end of the irradiation. After the end of the irradiation period, only the decay process exists and the number of product nuclei decreases exponentially. Therefore, the activity of the product nuclide after the decay period t_d measured from the end of irradiation is given by:

$$A(t_i, t_d) = R\,(1 - e^{-\lambda t_i})\, e^{-\lambda t_d}\;. \tag{3.6}$$

The production rate (R) of the active product nuclei in the target depends on the number of target nuclei present in the given target mass, and the photon flux ($\phi(E_\gamma, \vec{r})$) - cross section ($\sigma(E_\gamma)$) overlap integral:

$$R = \int_{vol} \int_{E_{th}}^{E_{max}} N(\vec{r})\sigma(E_\gamma)\phi(E_\gamma, \vec{r})\, dE_\gamma\, d^3r\;. \tag{3.7}$$

In Eq. 3.7, $N(\vec{r})$ is the number of target nuclide per unit volume, d^3r is the volume element of the target, $\phi(E_\gamma, \vec{r})$ is the energy differential photon flux expressed in the units of $[cm^{-2}\, s^{-1}\, MeV^{-1}]$, $\sigma(E_\gamma)$ is the cross section for the particular photoreaction (with threshold energy E_{th}), and E_{max} represents the maximum energy of bremsstrahlung photons which matches the electron beam energy. Combining equations 3.6 and 3.7, the activity of the product nuclei can be written as:

$$A(t_i, t_d) = (1 - e^{-\lambda t_i})\, e^{-\lambda t_d} \int_{v} \int_{E_{th}}^{E_{max}} N(\vec{r})\sigma(E_\gamma)\phi(E_\gamma, \vec{r})\, dE_\gamma\, d^3r\;. \tag{3.8}$$

The number of target nuclides in the given mass m is calculated as:

$$N_{target} = \frac{m \cdot N_a \cdot h}{A_r}\,, \tag{3.9}$$

where N_a is Avogadro's number (mol^{-1}), h is natural abundance of the target isotope, and A_r is the relative atomic mass of the target isotope ($\frac{gram}{mole}$).

There are no high quality exclusive ^{68}Zn(γ, p)^{67}Cu reaction cross section data over the broad energy range of interest. To calculate ^{67}Cu yield we used the evaluated cross section function adapted from KAERI simulation with GNASH code [27]. The photon flux through the target was sampled in 50 keV width energy bins using the MCNPX code. The average number of electrons per second was calculated for a given electron beam power and energy. A MATLAB program was written to calculate the ^{67}Cu yield. The program evaluates the integral (Eq. 3.7) by multiplying photon flux and cross section bin by bin from the reaction threshold energy (9.9 MeV) to the maximum photon energy and computes the activity using Eq. 3.8 (in μCi) for a given sample mass, time of irradiation, and beam power. This MATLAB program can be found in Appendix C.

3.3 Calculation of Zinc Target Temperature

The MCNPX-simulated energy deposition was used as input to calculate the zinc-target temperature. The target material was contained in an alumina crucible, which was cooled by compressed air blown on its outer surface. The primary source of energy deposition and heating was electrons reaching the target. A less significant amount (less than 20% of total) of heat came from photons. Thermal equilibrium is reached when the rate of heat deposition into the crucible is equal to the rate of heat dissipated by it. At equilibrium,

$$\dot{Q}_{in} = \dot{Q}_{out} \ . \tag{3.10}$$

The rate of amount of heat deposited can be expressed as:

$$\dot{Q}_{in} = \dot{Q}_{convection} + \dot{Q}_{radiation} \ , \tag{3.11}$$

or

$$\dot{Q}_{in} = Ah(T_f - T_s) + A\sigma\epsilon(T_h^4 - T_c^4) \ , \tag{3.12}$$

where T_f, T_s, T_h, and T_c are defined in Section 2.4. Eq. 3.12, for our case can be written as:

$$\dot{Q}_{in} = A\overline{h}(T_{air} - T_{alumina}) + A\sigma\epsilon(T_{alumina}^4 - T_{surrounding}^4) \ , \tag{3.13}$$

where $\dot{Q}_{in}$ is the MCNPX simulated power deposited, A is the surface area of the alumina crucible, and T_{air}, $T_{alumina}$, and $T_{surrounding}$ are temperatures of air, alumina crucible, and the surrounding, correspondingly. The emissivity coefficient ϵ for alumina was obtained from the emissivity table [46]. The convective heat transfer coefficient $\overline{h}$ was calculated for the forced convection caused by air blowing on the crucible surface by using Eq. 2.10, where the thermal conductivity “k” for alumina and the Prandtl number (Pr) were obtained from the tabulated data [47]. The Nusselt number $\overline{Nu}$ was determined by using Eq. 2.11, and the Reynolds number (Re) was calculated by using the relation:

$$Re = \frac{U_f D}{\nu} \; . \tag{3.14}$$

Here the air velocity U_f was calculated from the air compressor maintained at an air pressure of 50 psi (3.44 bar). The flow rate of air through a pipe of 0.95 cm in diameter at applied pressure of 50 psi was found to be 7 liters/sec [48]. Using this flow rate, air velocity was calculated to be 100 meters per second. The kinematic viscosity of the air, ν, at room temperature was found to be $1.5 \times 10^{-2}\text{cm}^2/\text{s}$ from the tabulated data [47]. With the crucible's external diameter 2.5 cm, the Reynolds number was estimated as,

$$Re = \frac{100 \times 0.025}{1.5 \times 10^{-6}} = 1.66 \times 10^{5} \; . \tag{3.15}$$

This value for the Reynolds number is in the turbulent regime, so the Nusselt number was calculated using the Churchill and Bernstein equation (Eq. 2.11). With the Prandtl number for air at $23\,^{\circ}\text{C} = 0.712$, Equation 2.11 gives,

$$Nu_D = 306.9 \; .$$

Now, the convective heat transfer coefficient between the air flow and the crucible's outer surface was determined by,

$$\overline{h} = \frac{\overline{Nu}k}{D} = 316\, Wm^{-2}K^{-1}\,. \tag{3.16}$$

Thus, Eq. 3.13 was solved for $T_{alumina}$. Since heat is transferred from the alumina crucible to the zinc target via conduction, we found T_{zinc} using the following equation:

$$\dot{Q}_{in} = \dot{Q}_{conduction} = \frac{2\pi Lk(T_{zinc} - T_{alumina})}{\ln \frac{r_{alumina}}{r_{zinc}}}\,. \tag{3.17}$$

3.4 Sample Preparation, Irradiation and Activity Measurement

3.4.1 Sample Preparation

To prepare the target, natural zinc shot was loaded into the alumina (Al_2O_3) crucible (target container) as shown in Figure 3.2 (left). Alumina was used as the target holder material because of its low chemical reactivity, hardness, low porosity, high melting point (2072 °C) and virtual absence of induced long-lived radioactivity. The crucible was then placed in the tube furnace to melt the zinc (see Figure 3.3). The tube furnace has an 8″ long hot zone with a 2″ diameter alumina casing for fully enclosing the tube. An inert gas line was connected to the chamber to prevent the oxidation of zinc. The entire system was maintained between 20 and 30 mtorr and subsequently flushed $2 - 3$ times with argon gas before heating the tube furnace. Inside the tube furnace, zinc was melted down at 550 – 700 °C. The zinc target before and after melting is shown in Figure 3.2. The majority of experiments were conducted with 99.99% or 99.9% pure natural zinc, although even higher purity is preferred in order to maximize the ^{67}Cu specific activity.

Figure 3.2: 99.99% 40 gram zinc shot in 2 cm × 2 cm alumina cup (left), zinc shot after melting (right).

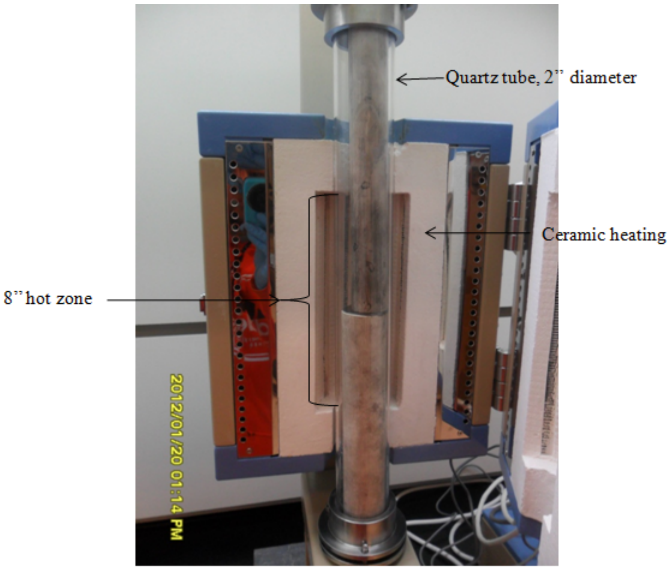

Figure 3.3: Tube furnace with 2″ diameter quartz tube casing for fully enclosing the tube [49].

3.4.2 Target Irradiation

The alumina crucible loaded with zinc was irradiated using a design performance 50 MeV, 10 kW linac at the Idaho Accelerator Center facility (IAC). It was placed about one centimeter away from the bremsstrahlung converter consisting of three 1.5 mm thick water-cooled tungsten plates (see Figure 3.4). Accelerated electrons hit the tungsten converter and produce bremsstrahlung photons as described in Section 2.2. A laser light source was used for checking the target alignment with the beam axis so that the beam was directed at the center of the target. To verify the beam energy, it was switched to the diagnostic beam line using dipoles of known characteristics which acted as an energy scanner of the beam. The in-line beam current was measured using an inductive pick-up loop (shown in Appendix D).

After the irradiation, the sample was left in the accelerator vault for several hours until short-lived radionuclides (e.g., ^{63}Zn, ^{65}Ni, ^{62}Cu) decayed so that the radiation exposure to working personnel was below the safety limits. A typical experimental setup for target irradiation is shown in Figure 3.4.

3.4.3 Activity Measurement and Analysis

The measurement and analysis of activity of the various radionuclides induced in the photon-activated sample was done using a gamma spectrometer. The setup consisted of a high purity germanium detector (HPGe), pre-amplifier, spectrometer amplifier, analog-to-digital converter (ADC), multi-channel analyzer (MCA), and computer with data acquisition software installed. The spectrometry setup used in

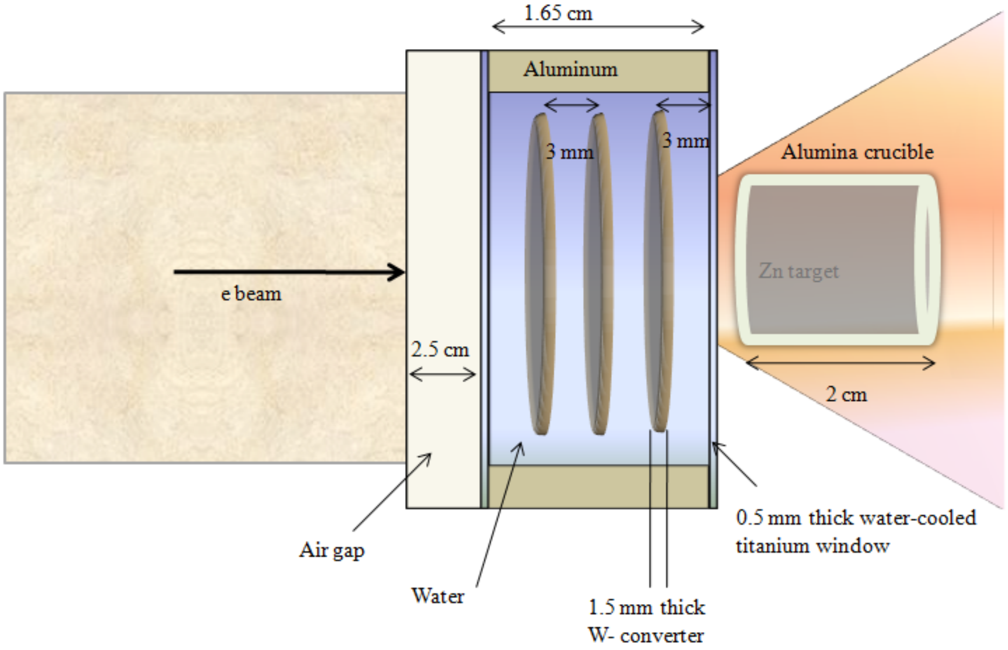

Figure 3.4: A schematic of the experimental setup.

this study is shown in Figure 3.5. We used an Ortec GEM25P4-70 type HPGe detector cooled with liquid nitrogen. Normally, semiconductor detectors are cooled to cryogenic temperatures because of the small band gap energy of the semi-conducting

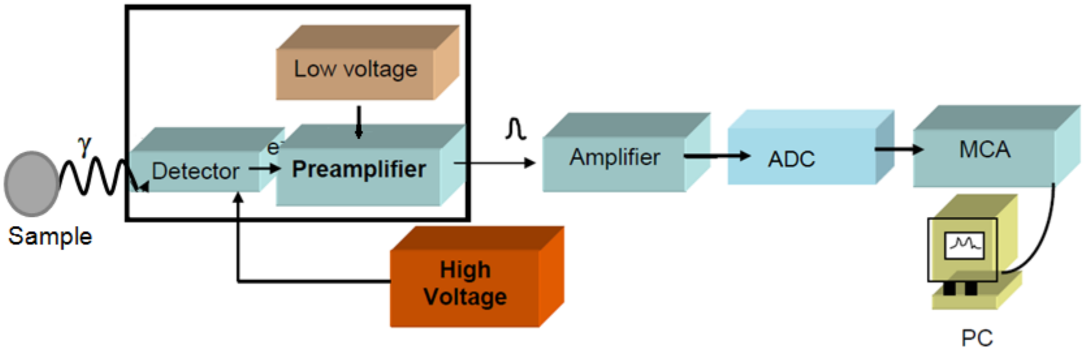

Figure 3.5: Block diagram of the gamma spectroscopy system.

materials (0.67 eV for Ge) which produces a large thermally-induced leakage current leading to a substantial background signal [35]. Depending upon the energy of photons emitted from radioactive sample, a photon interacts with the Ge crystal via the photoelectric effect, Compton scattering, or pair-production mechanisms, creating a number of electron-hole pairs. An externally applied electric field separates the pairs before they recombine so that the electrons drift towards the anode of the HPGe detector, while the holes drift to the cathode. The charge collected by the electrodes produces a current pulse, whose integral is proportional to the total charge ionized by the incident particle and can be used to measure the deposited energy.

Radioactive sources	Half-life	Energy (keV)
Co-57	279 d	122, 136.5
Ba-133	10.5 y	80.9, 356
Cs-137	30 y	661.7
Mn-54	312.3 d	834.8
Co-60	5.3 y	1173.2, 1332.5
Na-22	2.6 y	1274.5

Table 3.3: Radioactive calibration sources used for energy and efficiency calibration of the HPGe detector.

Before spectroscopic measurements were done, the detector was calibrated to determine the correspondence between the energy of the photon and the channel number of the ADC. Energy calibration of the detector is usually done using a set of standard sources (see Table 3.3). A polynomial fit of calibration data gives the energy calibration for the detector system.

The pre-amplifier is the first signal processing unit which is connected as close as is feasible to the detector to lower the capacitive loading. It minimizes the noise produced by the detector and hence enhances the energy resolution capacity of the spectrometer. The amplifier amplifies the signal coming from the pre-amplifier and is responsible for shaping the output pulse and performing the pile-up rejection. The signal is then fed into the ADC, which digitizes the output analog signal of the spectrometer amplifier. The digital signal is then matched to a given channel on the multichannel analyzer and sent to the computer, where this final digital signal is analyzed. The software used for the collection of spectra and analysis at the IAC is MPANT.

Figure 3.6: Sample positions in front of the HPGe detector.

Activated samples can be placed at several predetermined positions in front of the detector nozzle. These positions are lettered A through R, position A being 0.5 cm away and the position R being 100 cm away from the detector as shown in Figure 3.6. The efficiency curves of the detector at different positions were constructed for different energies using sources of known activities (see Table 3.3). The fitting function used for generating the efficiency curve is given by [50]:

$$\eta(E_\gamma) = \frac{1}{\left(\frac{a}{E_\gamma^c} + \frac{b}{E_\gamma^d}\right)} , \tag{3.18}$$

where a, b, c and d are the fitting parameters.

For example, for position K (30 cm away from the detector), the constants were found to be the following:

$$a = (3.64 \pm 1.51) \times 10^8 \text{ keV} ,$$

$$b = (12.5 \pm 0.61) \text{ keV} ,$$

$$c = (3.09 \pm 0.09) ,$$

$$d = (-0.76 \pm 0.007) .$$

The efficiency curve at position K is shown in Figure 3.7. Similar curves were constructed for all the positions.

During a gamma spectroscopy measurement, the detector counts the number of gammas that hit the detector and leave all their energy in it. That detection rate

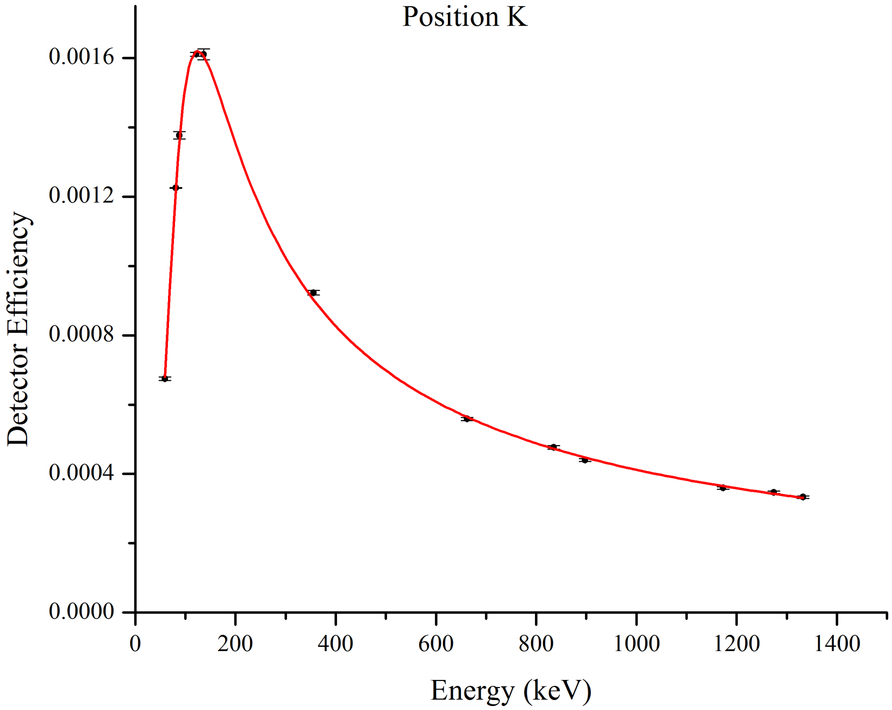

Figure 3.7: Detector efficiency for position K. Error bars represent the random (counting) statistical error.

divided by the efficiency yields the gamma emission rate. Dividing that by the branching ratio yields the decay rate. Since the activity decays exponentially with time, as shown in Figure 3.8, it can be found at any instant of time as:

$$A(t) = A_0\, e^{-\lambda t}\,, \tag{3.19}$$

where A_0 is the initial activity at the end of the irradiation.

If the measurement started at time t_1 and stopped at t_2, then the total number

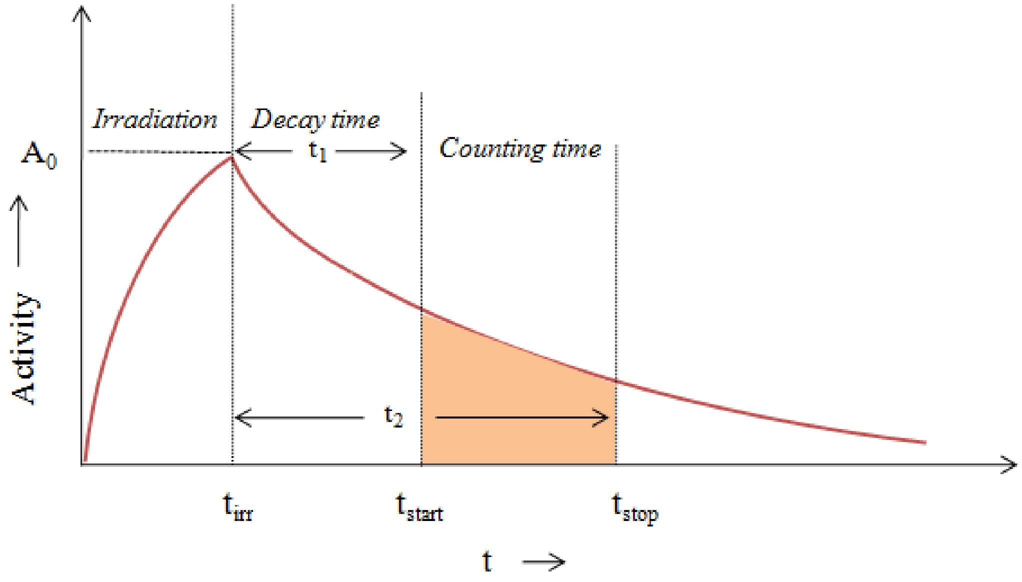

Figure 3.8: Radioactivity of a radionuclide as a function of time.

of disintegrations within the counting time $\Delta t = t_2 - t_1$ is:

$$\int_{t_1}^{t_2} A_0 \, e^{-\lambda t} dt = \frac{A_0}{\lambda}(e^{-\lambda t_1} - e^{-\lambda t_2}) \, . \tag{3.20}$$

This is related to the total number of counts C seen by the germanium detector by the following relation:

$$\frac{C}{BR \cdot \eta} = \frac{A_0}{\lambda}(e^{-\lambda t_1} - e^{-\lambda t_2}) \, , \tag{3.21}$$

where BR is the branching ratio (or emission probability) of the photon of a given energy and η is the detector efficiency. The activity of radionuclide at the end of irradiation can be calculated as:

$$A_0(t) = \frac{C \cdot \lambda}{BR \cdot \eta \, (e^{-\lambda t_1} - e^{-\lambda t_2})} \, . \tag{3.22}$$

In equation 3.22, the uncertainty from half-life λ, branching ratio BR, and the time parameters (t_1 and t_2) usually can be ignored. The uncertainty in the detector efficiency for 185 keV (the predominant energy from ^{67}Cu) is less than 1% (see Figure 3.7). Thus, the uncertainty in the ^{67}Cu activity originated primarily from the random (counting) statistical error in net counts C, which can be propagated as:

$$\frac{\delta A}{A} = \sqrt{\left(\frac{\delta C}{C}\right)^2} = \frac{\delta C}{C}\ . \tag{3.23}$$

3.5 Measurement of Zinc Temperature

To measure the production rate and yields, natural zinc metal was melted and made into a slug inside an aluminum oxide crucible. To measure the zinc temperature, a K-type thermocouple (OMEGA KMQXL-125 with a reported calibration error of 1%) was inserted about 1 cm deep into the zinc target through a hole drilled in it, as shown in Figure 3.9. As zinc samples were activated using various electron beam powers, their temperatures were measured using the thermocouples. The thermocouple was connected to a Signal Conditioning (SC-2345) connector which measures the potential difference between two junctions of the thermocouple. The output of the SC connector was coupled to the CPU of a computer where a system-design platform and development environment application package LabVIEW was installed. A LabVIEW program was written to convert the potential difference between the two junctions of the thermocouple into the temperature difference using the Seebeck formula (Eq. 3.25) [51], and displayed the temperature of the hot end of the thermocouple as a function of irradiation time:

$$s = \frac{dV}{dT} \ , \tag{3.24}$$

$$T_h = T_0 + \frac{dV}{s} \ , \tag{3.25}$$

where "T_0" is the reference temperature, dV is the potential difference, and s is the thermoelectric sensitivity (also known as the Seebeck coefficient) of the thermocouple material. The reference (cold) end of the thermocouple was maintained at room temperature during the irradiation. The estimated zinc target temperatures were compared with the experimentally determined temperature, measured at various electron beam powers.

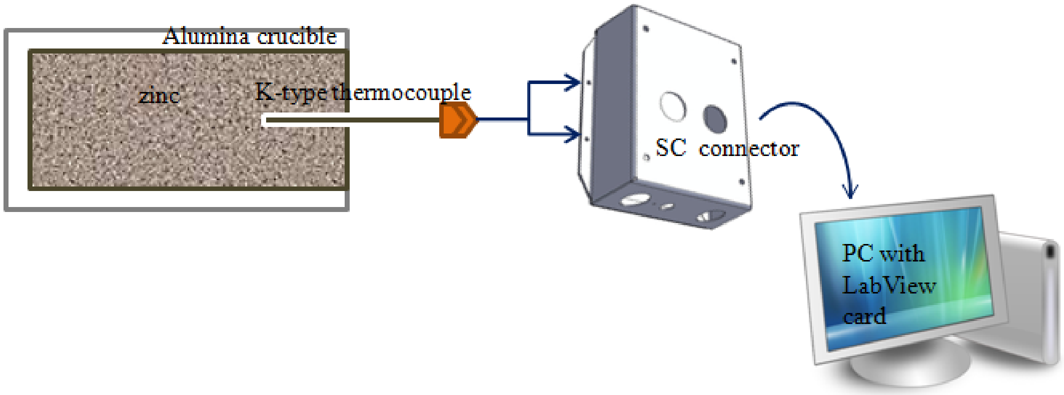

Figure 3.9: Temperature measurement of the zinc slug using a thermocouple.

3.6 Corrosion Measurement

The direct methods of corrosion evaluation involve various techniques such as Electrochemical Impedance Spectroscopy (EIS) [52], Scanning Electron Microscopy (SEM), followed by Energy Dispersive X-ray Spectroscopy (EDS) [53], and trace element analysis using ICP-MS/ICP-OES [54], which measures the thickness of the oxide layer on the metal surface and corresponding corrosion products' mass. The most common indirect measurement technique involves yield measurement of H_2 gas and H_2O_2, which are the most stable radiolytically produced oxidizing species [55]. In order to study the radiation enhanced corrosion on metals, we used Photon Activation Analysis (PAA), a sensitive technique, which allows measuring ppb to ppm levels of most elements in the periodic table [30]. To measure the radiolytically induced corrosion of metals, a set of foils (Al, Cu, stainless steel, Ta, Ti, W, and Zn) were irradiated in test tubes filled with deionized water for 1000 watt-hours. A 10 cm thick aluminum brick was placed in front of the tubes to prevent their heating. A blank water sample was also activated under the same condition. The total dose each of the samples received was estimated to be about 45 kGy. The activation setup is shown in Figure 3.10.

After the activation, the foils were removed from the tubes and their activity was measured using an HPGe detector. Radioactive water from all the tubes were combined and poured into a new, non-activated vial and counted for approximately 46 hours, after 21 hours of cooling after the end of irradiation. Immediately after the gamma spectrum of the mixed sample was measured, the activated blank sample of water was also counted for 67 hours. Gamma spectra were obtained following the methods described in Section 3.4. The net counts for the energy peaks from isotopes of interest, contributed by various irradiated metal foils, were evaluated by

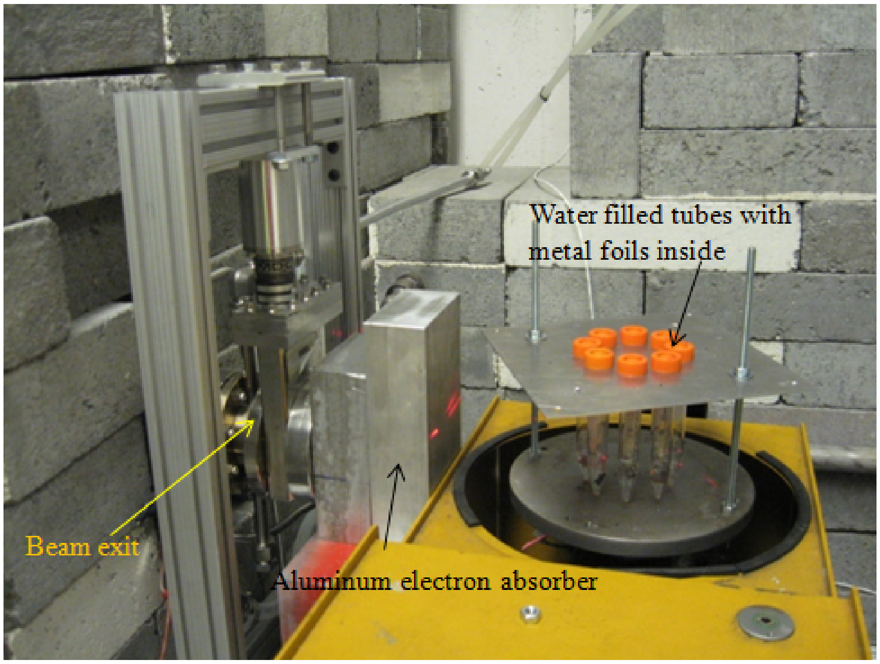

Figure 3.10: Activation setup for the photon activation of various metal foils.

subtracting background from the mixed sample as well as from the blank sample, as described below in detail.

- **Internal background subtraction**

A photon spectrum from each product nuclide is the superposition of background spectrum (primarily due to the Compton effect and background radioactivity) and the photo-peak, described in terms of a Gaussian curve. To determine the net area of the full energy signal, the background must be subtracted. Gaussian fits on all the peaks of interest were done as shown in Figure 3.11. The FWHM (full width at half of maximum) was obtained for each peak and used to calculate the number of channels in the region of interest. For example, for the 93 keV energy peak corresponding to

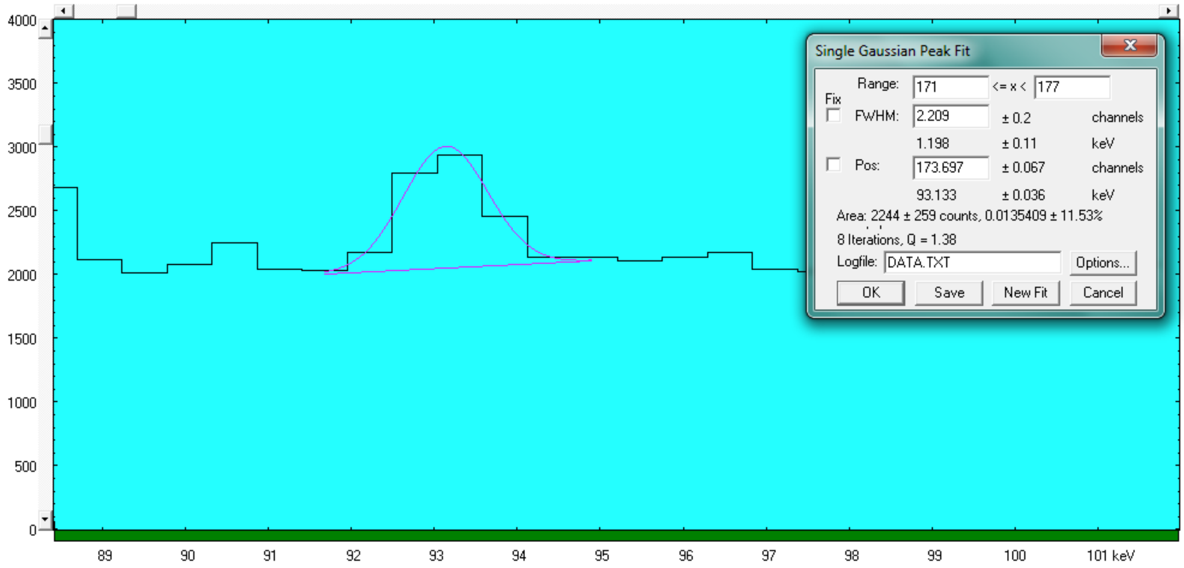

Range: 171 <= x < 177
☐ FWHM: 2.209 ± 0.2 channels
1.198 ± 0.11 keV
☐ Pos: 173.697 ± 0.067 channels
93.133 ± 0.036 keV
Area: 2244 ± 259 counts, 0.0135409 ± 11.53%
8 Iterations, Q = 1.38
Logfile: DATA.TXT

Figure 3.11: 93 keV energy peak corresponding to ^{180m}Ta in the mixed sample.

^{180m}Ta:

$$FWHM = 1.198 \text{ keV} = 2.209 \text{ channels} . \tag{3.26}$$

The standard deviation "σ" of a Gaussian is related to its FWHM as:

$$FWHM = 2.35\,\sigma = 2.209 \text{ channels} , \tag{3.27}$$

$$\sigma = \frac{2.209}{2.35} = 0.94 \text{ channels} \approx 1 \text{ channel} . \tag{3.28}$$

The area under the region of interest ($E_{peak} \pm 3\,\sigma$) would cover 99.8% of the total area under the curve. Therefore, six channels were used for the region of interest for this particular peak. Similar calculations were done for all the peaks.

For the energies where no significant peak was observed, a "forced summation of peaks" technique was used to find the "net counts." Gross counts on half of the

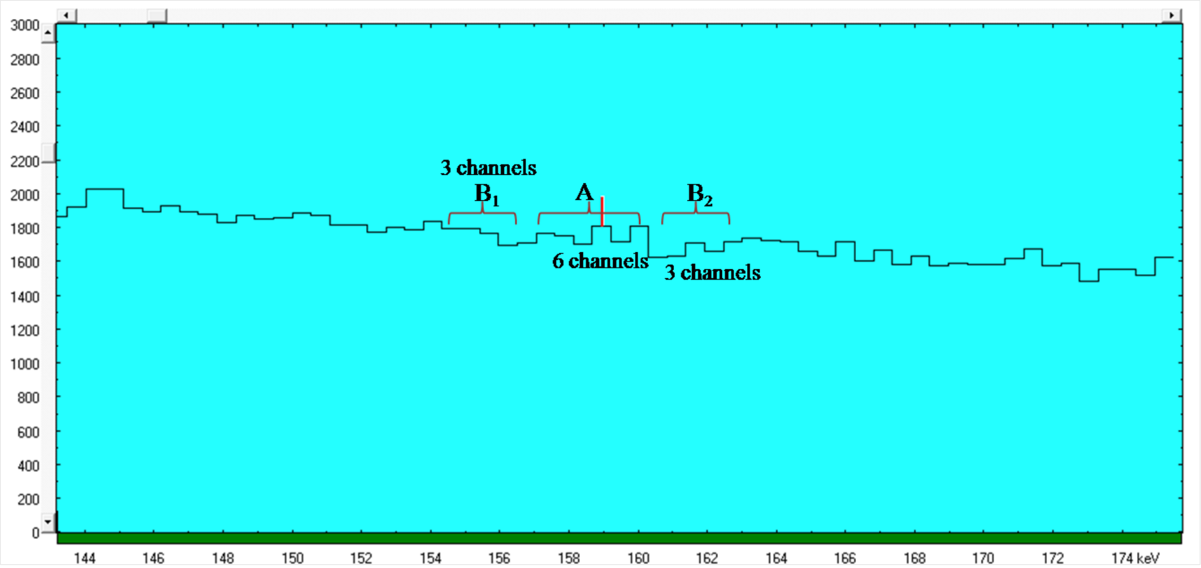

Figure 3.12: Side-band correction for the 159 keV energy peak corresponding to ^{47}Sc in the mixed sample.

band on each side of the central band were taken (see Figure 3.12). The gross sum of background counts was subtracted from the central gross counts to get the net counts in the "peak." Note that the "net number of counts" could be zero or even negative in this case. The net count calculations for 159 keV energy corresponding to ^{47}Sc is shown below as an example.

- **<u>Net Count Calculation</u> (for 159 keV)**

Gross counts for mid band (6 channels) $(A) = (1700 \pm \sqrt{1700}) + (1810 \pm \sqrt{1810}) + (1719 \pm \sqrt{1719}) + (1811 \pm \sqrt{1811}) + (1623 \pm \sqrt{1623}) + (1629 \pm \sqrt{1629})$

$= (1700 \pm 41.2) + (1719 \pm 42.5) + (1719 \pm 41.5) + (1811 \pm 42.5) + (1623 \pm 40.3) + (1629 \pm 40.4)$

$= (1700 + 1810 + 1719 + 1811 + 1623 + 1629) \pm \sqrt{(41.2)^2 + (42.5)^2 + (41.5)^2 + (42.5)^2 + (40.3)^2 + (40.4)^2}$

$= 10292 \pm 101$

Likewise:

Left three channels gross count $(B_1) = 5231 \pm 72.3$

Right three channels gross count $(B_2) = 5084 \pm 71.3$

Net Count $(N_1) = A - (B_1 + B_2) \pm \sqrt{(\delta A^2 + \delta B_1^2 + \delta B_2^2)}$

$= 10292 - (5231 + 5084) \pm \sqrt{(101)^2 + (72.3)^2 + (71.3)^2)}$

$= -23 \pm 143$

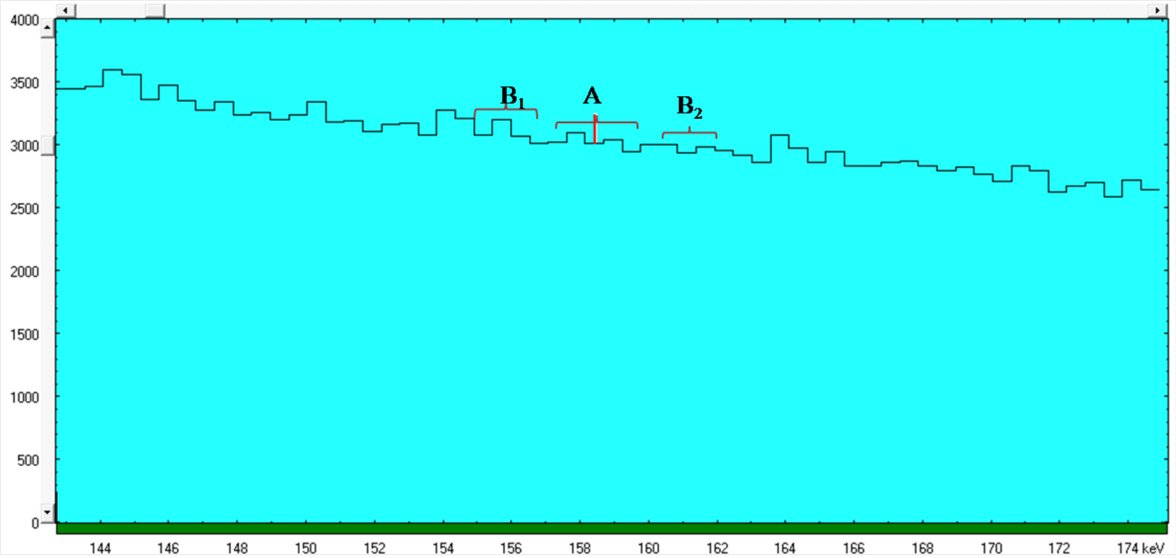

Figure 3.13: Side band correction for the 159 keV energy peak corresponding to ^{47}Sc in the blank sample.

Since the blank and mixed samples were counted for different time periods, the counts from the blank sample were time corrected (corrected for the counting time of mixed sample) to be compared with the mixed sample.

- **Counting time correction**

Counting time for the blank sample $(T_b) = 242742$ seconds

Counting time for the mixed sample $(T_m) = 165701$ seconds

Time correction factor $(K) = \frac{T_m}{T_b} = \frac{165701}{242742}$

Original counts from the blank sample $= C_b$

Time corrected counts for the blank sample $= C_b \times K$

After that the “net count” was evaluated in the same manner discussed above:

Net Count $(N_2) = 126 \pm 144$

Total net counts $(N_1 - N_2) = -149 \pm \sqrt{(143^2 + 144^2)}$

$= -149 \pm 203$

Chapter 4

Results and Discussions

4.1 Optimization of Beam Parameters

4.1.1 Yield as a function of electron beam energy (for constant current)

The electron beam energy is one of the critical beam parameters for determining the production yield of photo-produced radionuclides. It was shown in Chapter 3 that radioisotope yield is proportional to the integral of the product of photon flux '$\phi(E)$' and the reaction cross section '$\sigma(E)$' (see Eq. 3.8), and both of these functions are energy dependent. To investigate the effect of electron beam energy on the photonuclear production yield of radionuclides at constant beam current, we used the MCNPX radiation transport code to simulate the photon flux through a natural zinc target using various beam energies. ^{67}Cu activities were evaluated following the methods described in Section 3.2. Figure 4.1 (left) shows the results of the MCNPX simulations of photon flux through a 40 gram natural zinc target, placed 1 cm away from the 4.5 mm thick tungsten converter (details on the converter will be given in Section 4.2). The simulated flux was multiplied by the ^{68}Zn(γ, p)^{67}Cu cross section (shown in Figure 4.1, left). The areas under the resulting peaks (seen in Figure 4.1, right) represent the photon energy-dependent parts of the yield. As the energy of the electron beam increases, the yield initially grows quickly, but eventually its growth slows down. Monte Carlo simulations of ^{67}Cu yield were benchmarked with yield

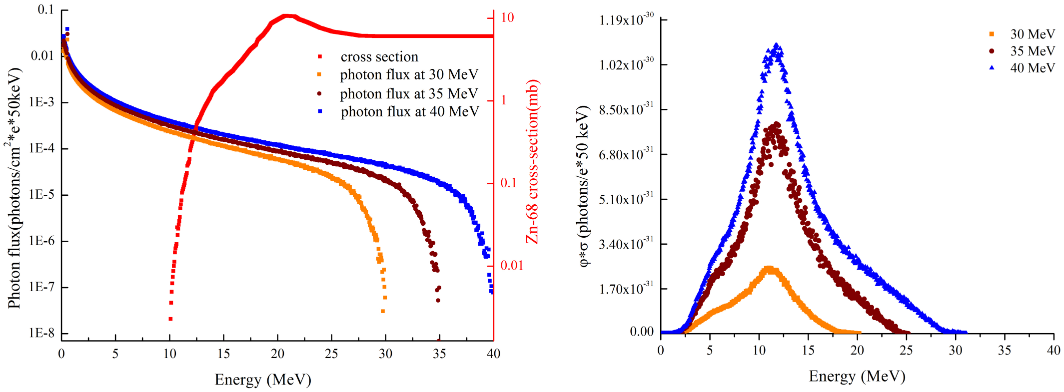

Figure 4.1: Left: ^{68}Zn(γ, p)^{67}Cu cross section and photon flux for different electron beam energies, right: product of flux and cross section ($\phi(E_\gamma \cdot \sigma(E_\gamma))$ for different energies, and fixed electron beam current.

measurements performed at the IAC. A 40 gram natural zinc target was placed 1 cm away from the bremsstrahlung converter and irradiated using $30 - 43$ MeV electron beams. A water-cooled tungsten converter was used as the bremsstrahlung source. ^{67}Cu yields were measured using a gamma spectroscopy system as described in Section 3.4.

Energy (MeV)	Peak current (mA)	Rep. rate (Hz)	Pulse width (μs)	Average current (μA)
30	49	10	7	3.4
35	40	30	2.4	2.9
38	50	120	4.4	26
41	49	120	4.2	25
42	48	120	4.2	24
43	47	120	4.2	24

Table 4.1: Electron beam parameters used for the experimental verification of ^{67}Cu yields using various beam energies.

Figure 4.2 shows the ^{67}Cu yield for various electron beam energies, assuming one hour of irradiation. A constant current of 100 μA was used for the simulations. Experimental data were obtained using different average currents (see Table 4.1) and normalized to 100 μA current for comparison. As can be seen from Figure 4.2, ^{67}Cu yield increases nearly linearly with electron beam energy up to about 38 MeV and slowly saturates at higher energy. The uncertainties of the measured ^{67}Cu yields did not exceed 5%. The divergence of the calculated and measured ^{67}Cu production yield is possibly due to the error in beam parameters (for example, electron beam current, energy spread, beam divergence, beam steering etc.), which increases with increasing beam energy. This is because the electron beam itself loses its integrity at the end of load-line in terms of emittance and energy dispersion. Also, the nature of the ^{68}Zn(γ, p)^{67}Cu cross section, which falls off above the giant dipole resonance energy region (see Figure 4.1), is another possible reason for the flattening of the measured ^{67}Cu yield.

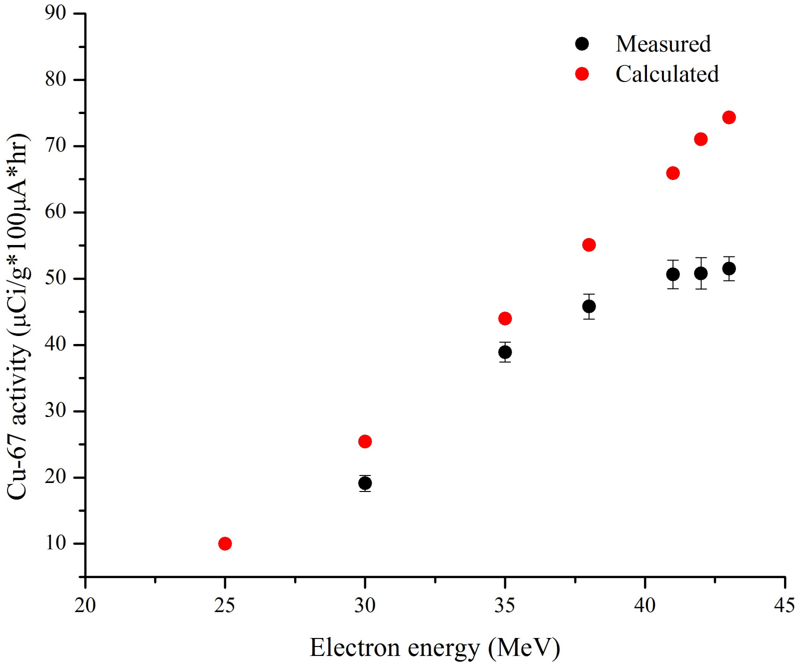

Figure 4.2: Activity of ^{67}Cu as a function of electron beam energy normalized by mass, current and time of irradiation. The error bars in the activity values represent the random (counting) statistical errors. The divergence of the two curves may arise from increasingly poor electron beam emittance, energy dispersion, steering, current measurement, or all of the above. These issues are discussed in Section 4.1.4.

4.1.2 Yield as a function of electron beam current (for constant energy)

Assuming that all other beam parameters are constant including the electron energy, the ^{67}Cu yield must depend linearly on the electron beam current. However, the condition of constant beam parameters is not attainable with physical beams. To evaluate the yields as a function of beam current we simulated the photon flux through a 40 gram natural zinc target placed 1 cm away from a 4.5 mm thick bremsstrahlung converter and calculated the specific activity of ^{67}Cu for various beam currents. The results of the simulations are shown in Figure 4.3. To increase the isotope production rate, one needs to maximize the electron beam current. However, as we will see in the next section, there are limitations on the current increase, and on the beam quality as a function of beam current.

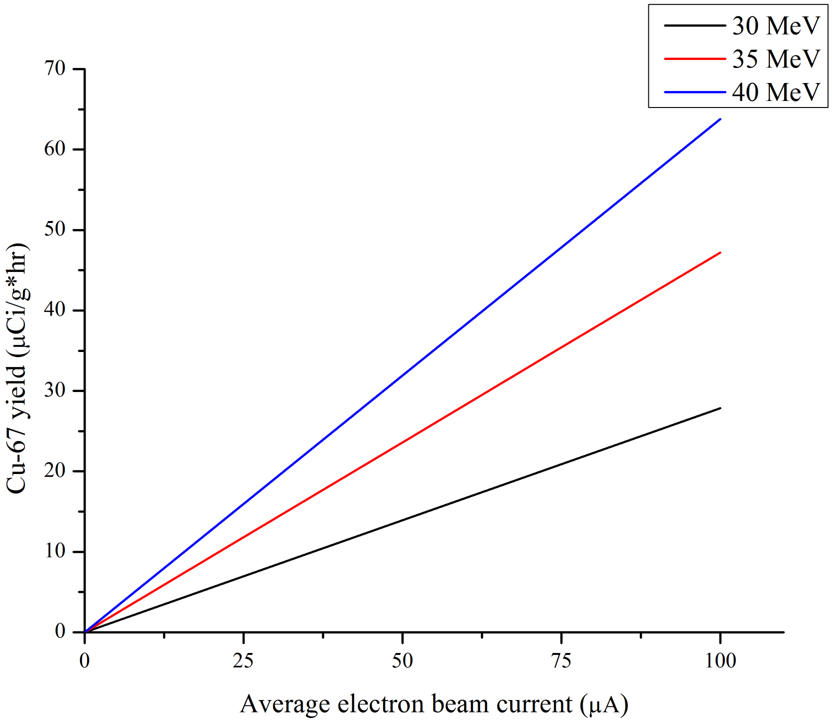

Figure 4.3: ^{67}Cu yield as a function of electron beam current for various beam energies as calculated from simulations.

4.1.3 Beam loading constraint and resulting optimum energy and current of electron beam

As can be seen from Figures 4.2 and 4.3, both electron beam energy and current need to be maximized to maximize the ^{67}Cu yield. However, the load characteristics of RF-driven electron linacs as discussed in Section 2.3 do not allow simultaneous increase of both parameters. Thus, we need to find an optimum energy/current regime to provide the maximum yield of ^{67}Cu. In order to do this, we first calculated the peak beam current using the beam load function for different beam energies. The results of these calculations are summarized in Table 4.2.

Assuming the average beam duty factor−the fraction of time the beam is "on"−to be 0.1%, the average current and the average power were calculated from the peak current for each given electron beam energy. For example, a 38 MeV "loaded" beam energy corresponds to the peak beam current of 121 mA. Assuming a 0.1% duty factor, the corresponding average current is 121 μA. The average power is therefore:

$$\begin{aligned} P_{average} &= 38\ \mathrm{MeV} \cdot 121\ \mathrm{mA} \cdot 0.1\% \\ &= 38 \times 10^{6}\ \mathrm{V} \cdot 121 \times 10^{-3}\ \mathrm{A} \cdot 0.001 \\ &= 4.6\ \mathrm{kW}\ . \end{aligned} \tag{4.1}$$

Once the average current is known, the ^{67}Cu yield can be calculated for each energy value following the methods described in Section 3.2. Such calculations were done for

Electron beam energy (MeV)	Peak current (mA)	Average current (assuming a 0.1% duty factor) (μA)	Average power (assuming 0.1% duty factor) (kW)	^{67}Cu yield (μCi/g $\cdot$ hr)
25	231	231	5.76	24.2
30	188	188	5.65	47.9
32	172	172	5.49	58.7
35	146	146	5.11	65.1
38	121	121	4.59	68.1
41	95.5	95.5	3.91	65.9
42	87.1	87.1	3.65	61.7
43	78.6	78.6	3.38	55.6
47	44.8	44.8	2.32	44.1
50	19.4	19.4	0.970	22.4

Table 4.2: Electron beam parameters obtained from the load line (Figure 2.4) of 50 MeV linac at the IAC using various beam energies and the simulated ^{67}Cu yield.

energies ranging from 25 MeV to 50 MeV (see Table 4.2). The data points of the ^{67}Cu yield were fitted with a Gaussian function. The peak of the curve was chosen as the optimum energy, and its corresponding current was chosen as the optimum current. The result shows that the calculated optimum energy for ^{67}Cu production with the 50 MeV linac housed at the IAC is 37.4 ± 0.2 MeV (see Figure 4.4). The error in the energy reported is the standard error. The corresponding optimum current is 126 ± 3 μA. To benchmark our simulations, a number of zinc activation experiments were performed. According to the measured activity values, the optimal beam energy for

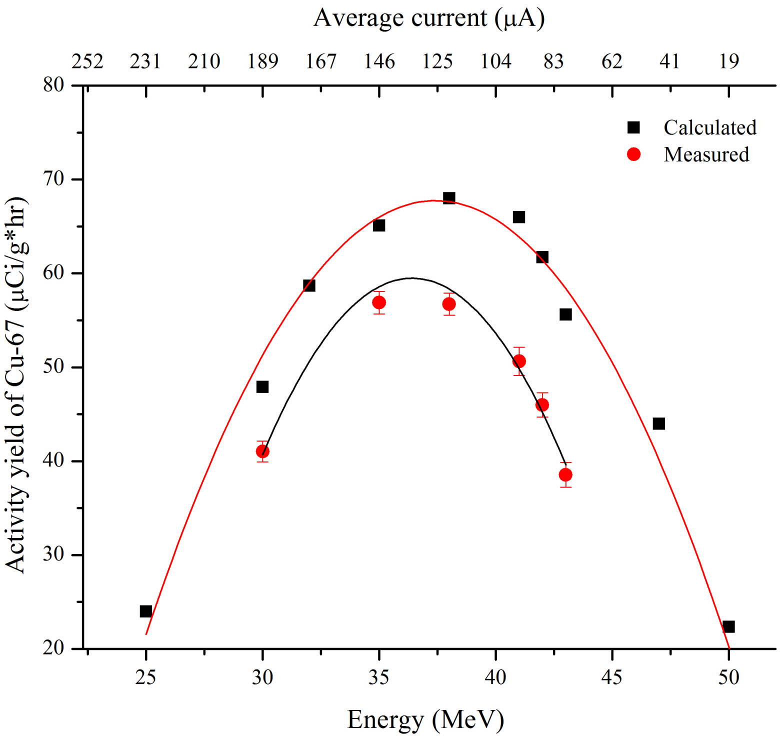

Figure 4.4: Simulation and experimental results of ^{67}Cu yield with load-line constraint. The error bars in the activities are the counting statistical errors only.

the accelerator used for the photo-production of ^{67}Cu is 36.4 MeV, with the standard error of 0.2 MeV (see Figure 4.4). The corresponding optimum current would be 134 ± 1 μA [1]

The experimentally determined ^{67}Cu yields (see Figures 4.2, and 4.4) are $15-35\%$

---

[1] The percentage error in the optimum energy

$$= \frac{\delta E}{E} \times 100 = \frac{0.24\,\text{MeV}}{36.4\,\text{MeV}} \times 100 = 0.6\%$$

Therefore from Equation 2.6, the uncertainty in the peak current

$$= 0.006 \times 134\,\mu A = 0.88\,\mu\text{A} \approx 1\,\mu\text{A}$$

less than the MCNPX-predicted values. Several contributing sources were investigated for this difference between calculated and measured values.

1. High quality exclusive ^{68}Zn(γ, p)^{67}Cu cross section data over the entire energy range of interest does not exist. The difficulty with such experiments lies in the difficulty of

    i) getting low-energy recoil protons to exit the target with minimal energy loss,
    ii) cleanly detecting protons in a spectrometer with good energy resolution,
    iii) getting monochromatic photon beams, and
    iv) while also requiring coincidences between these protons and the "tagged" photon-producing electrons.

    Because of this data-gap, we used a theoretically modeled cross section published by the IAEA in their "Handbook of Photonuclear Data" [27]. Unfortunately, the IAEA theoretical cross section has no published uncertainty, and no experimental data is available with which to compare. One could, in principle, compare the IAEA model calculations of other nuclei and/or other exclusive reactions with experimental data, but the paucity of such charged-particle data leaves considerable room for uncertainty. Instead, we argue that we should compare to other inclusive photon activation measurements and simply note that, in principle, an error in the IAEA calculation could cause a significant discrepancy between simulated and experimental results.

2. Beam current was not measured on the target itself, but rather estimated from the currents measured at the bremsstrahlung converter. Therefore, biased beam-current measurement could contribute to the error in the experimentally measured yields per current.

3. For the simulations, the electron beam was assumed to be a monoenergetic pencil beam. The emittance, the energy spread of electrons in the beam and the "mis-steer" of the beam were all assumed to be zero. In practice, such ideal conditions for electron beam cannot be met. Real electron beams have energy spread, thickness, emittance, and non-zero divergence. In addition, the target and/or electron beam can be misaligned. In the next section we will discuss how the beam quality and target alignment can affect the yield of ^{67}Cu.

4.1.4 Beam quality effect on the yield

All the simulations discussed in Section 4.1.1 – 4.1.3 assumed a monochromatic 40 MeV pencil beam with zero divergence that was centered on the target axis. Real electron beams always have energy spread, spatial distribution, non-zero emittance and divergence and are not perfectly centered. To investigate how beam quality affects the photon flux, and, as a result ^{67}Cu activity, numerous MCNPX simulations were performed. Our goal was to compare photon fluxes through a 40 gram natural zinc target using different electron beam characteristics.

Beam spot size

We started with varying the beam spot size (diameter), assuming a monochromatic 40 MeV cylindrical electron beam with uniform charge distribution and zero divergence (see Figure 4.5).

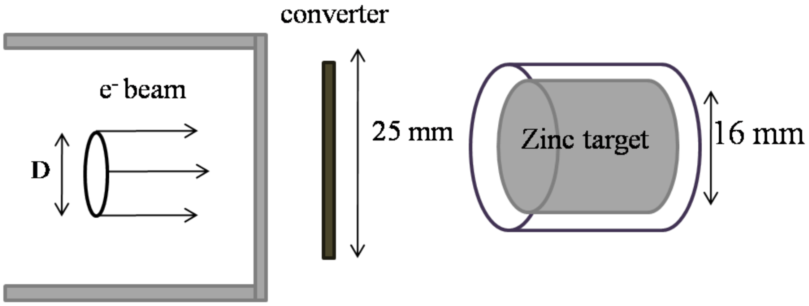

Figure 4.5: Schematic of the electron beam spot diameter.

Figure 4.6 shows the ^{67}Cu activity as a function of beam spot size. The ^{67}Cu yield for realistic 8 mm diameter beam size decreases by around 5% from the yield for a pencil beam. However, doubling the beam spot size (so it becomes equal to the zinc target diameter, 16 mm) decreases the yield by about 22%. Once the beam size becomes comparable to the diameter of the converter (2.5 cm), the yield drops to about half of the yield produced by the pencil beam. This observed pattern of ^{67}Cu yield derives from the fact that more bremsstrahlung photons miss the photo-target as the size of electron beam increases, which results in less photonuclear transmutation inside the target.

To measure the size of the electron beam, we placed glass plates right behind the beam window and briefly exposed them to the electron beam. As high energy

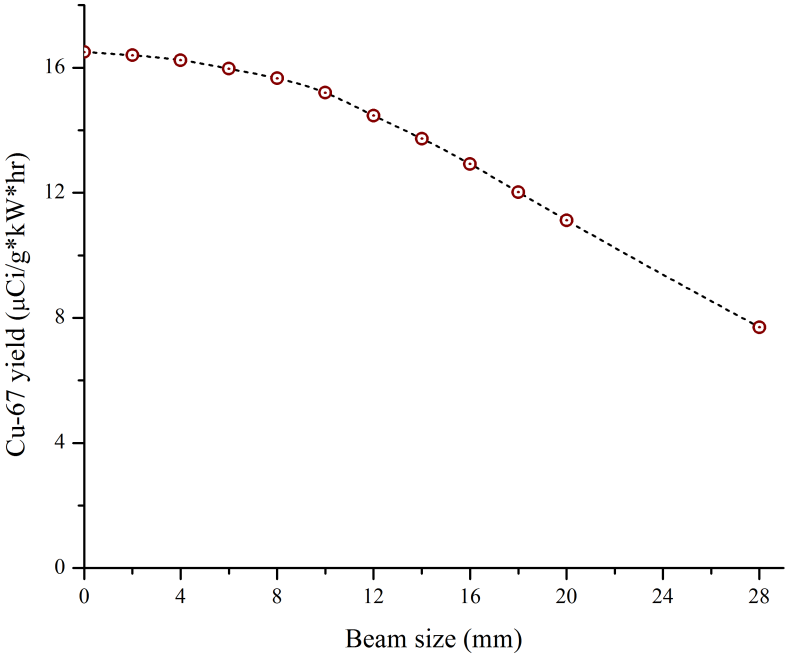

Figure 4.6: ^{67}Cu yield as a function of the beam spot diameter. Typical beams from this accelerator are approximately 1 cm in diameter.

electrons interact with glass, it darkens noticeably. The size of the dark spot approximately represents the size of the beam. The exposed glass plate was scanned using a scanner and the beam spot was measured. The resulting image was processed using image processing software "Image J," and the beam profile was obtained. Beam size measurements were performed several times and the beam size was found to be in the range of 6 − 8 mm. Figure 4.7 shows a typical scan of the glass plate exposed to 40 MeV electron beam (left) and the corresponding beam profile (right). The beam diameter was found to be about 8 mm.

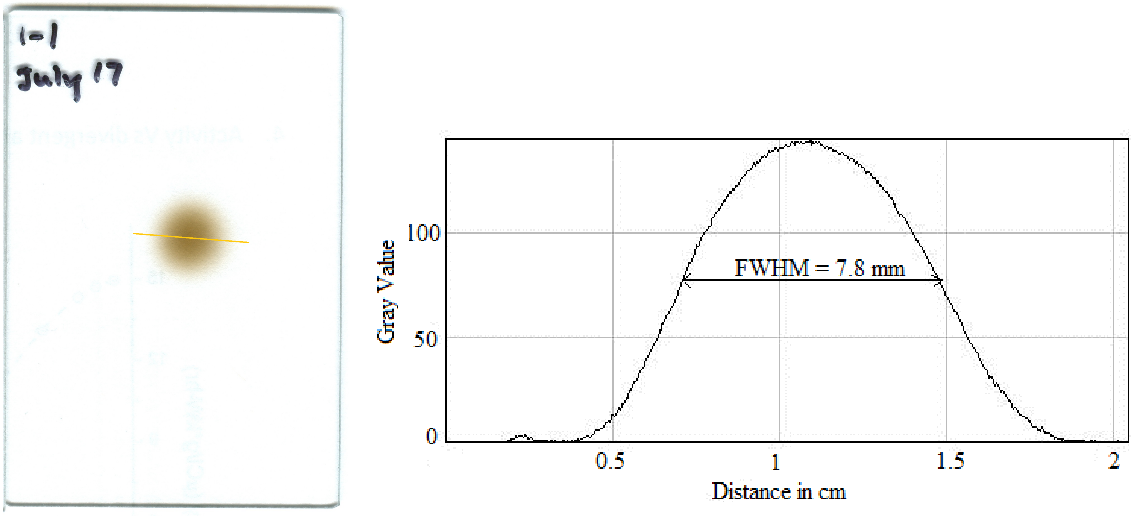

Figure 4.7: An example of the typical beam size. Left: Glass plate exposed to electron beam, right: electron beam profile.

Beam angular divergence

Next, we investigated the effect of beam divergence 'θ' on ^{67}Cu yields. Electron beams diverge due in part, to the repulsive force between similarly charged particles. Most of the emittance of an electron beam originate at the thermionic source. Beam divergence is the product of the angular dispersion and the beam size at the interaction point. In the simulation we varied beam divergence angle, considering a 40 MeV cylindrical electron beam with 6 mm beam spot size (see Figure 4.8). Using the photon flux obtained from the MCNPX simulation the ^{67}Cu yield was calculated. Figure 4.9 shows ^{67}Cu activity as a function of the electron beam divergence. When the beam divergence angle grows, a large fraction of forward boosted bremsstrahlung photons miss the target, hence decreasing the production yield. The drop in the ^{67}Cu yield is less than 5% when the beam divergence is increased from zero to 3 degrees.

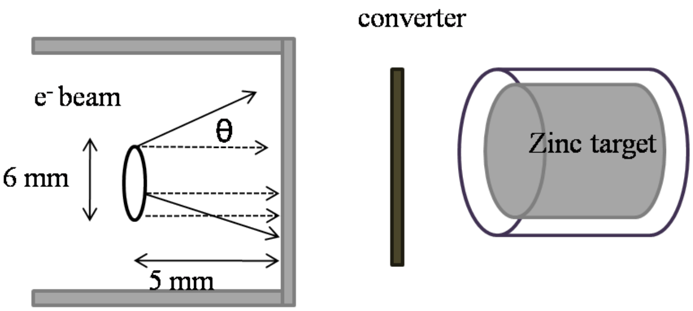

Figure 4.8: Variation of electron beam divergence.

However, further increase in divergence decreases the yield significantly (for example, about 50% at $\theta = 10$ degrees).

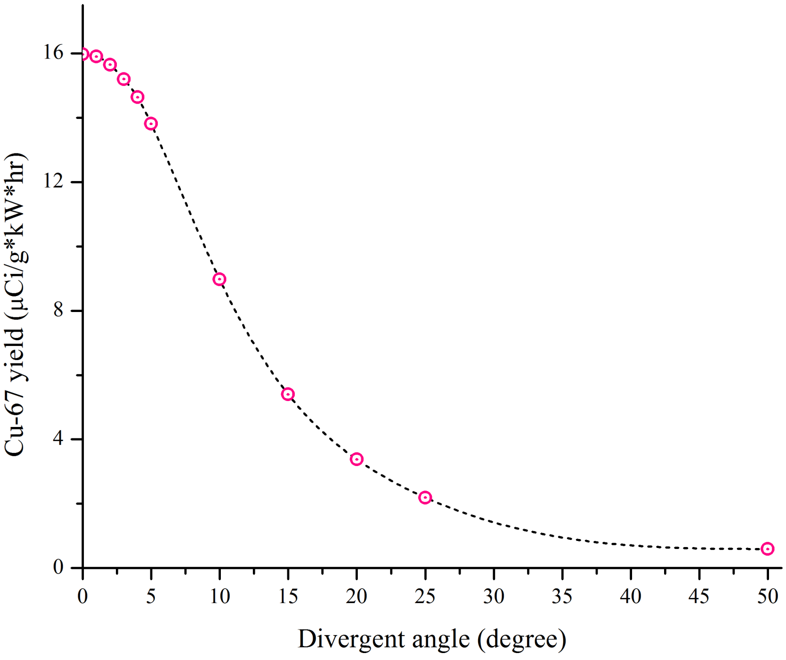

Figure 4.9: ^{67}Cu yield as a function of the beam angular divergence. Post-exit window angular divergence of electron beams from medical linacs are typically in the $2 - 4°$ range [56].

Beam energy spread

Beam energy spread is another important quality parameter of the electron beam. A small energy spread corresponds to a nearly monoenergetic beam. However, obtaining a monoenergetic electron beam is not trivial for room temperature linacs. The longitudinal space charge effect within the electron bunch causes some beam spreading. More importantly RF wave timing and phasing with respect to the beam can result in increased energy spread. In addition, electrons are injected at the source at all phases of the RF, resulting in many electrons out of ideal phase.

The energy spread for various beam energies of the electron beam was measured by using a slit system in combination with dipole magnets. By adjusting the dipole strength, the electron beam was scanned and the current at each end of the slit was measured using a Faraday cup. The spectrum of energies of distributed electrons in the beam was fitted using a Gaussian function (see Figure 4.10). For example, for the 50 MeV linac housed at the IAC the energy spread for the beam whose current peaked at 40 MeV was measured to be 6 ± 0.5 MeV which is about 15% of peak energy. Photon flux simulations were performed for a 40 MeV monoenergetic electron beam and a 40 MeV electron beam with 15% energy spread, assuming a 6 mm beam spot size and zero divergence (note that electron beam spot size was measured in the range of $6-8$ mm, and we used the smallest value). The monochromatic beam produced 15.9 μCi/g·kW·hr of ^{67}Cu whereas, for the electron beam with 15% energy spread the activity dropped to 15.6 μCi/g·kW·hr (by about 2%).

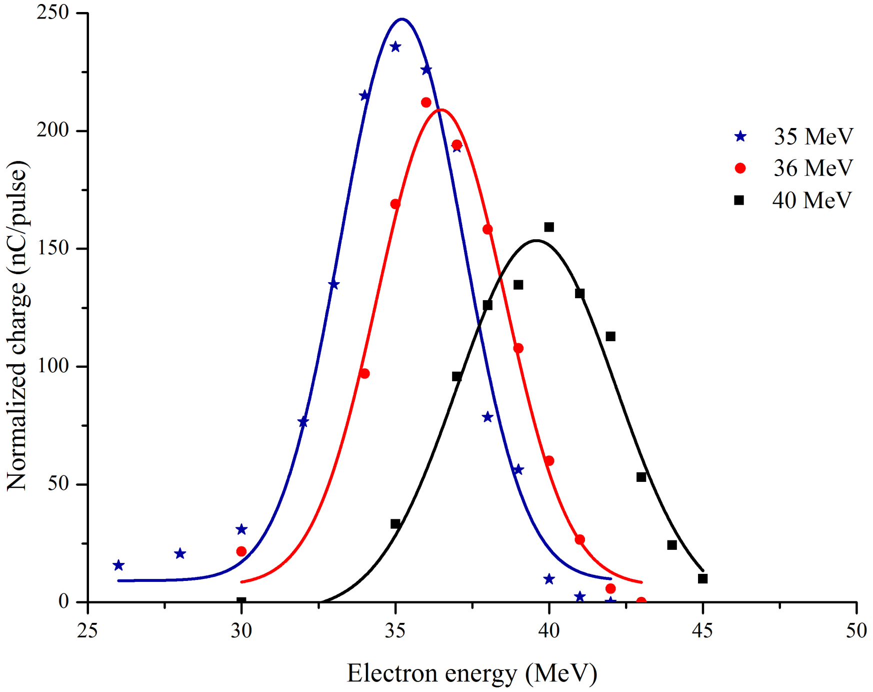

Figure 4.10: Electron beam energy profile at various nominal electron beam energies.

Beam center offset

Shifting the electron beam from the optical axis of the setup also affects the yield of ^{67}Cu. We investigated the effect of beam misalignment on ^{67}Cu yield by simulating the electron beam shift in the transverse direction (normal to the axis). A 6 mm thick 40 MeV monoenergetic electron beam with zero divergence was considered for the simulation (see Figure 4.11). ^{67}Cu yield was calculated using the simulated photon flux as described in Section 3.2.

Figure 4.12 demonstrates the effect of the beam shifting from the zinc target (16 mm in diameter) axis on ^{67}Cu yield. The yield drops by 1% when beam is shifted

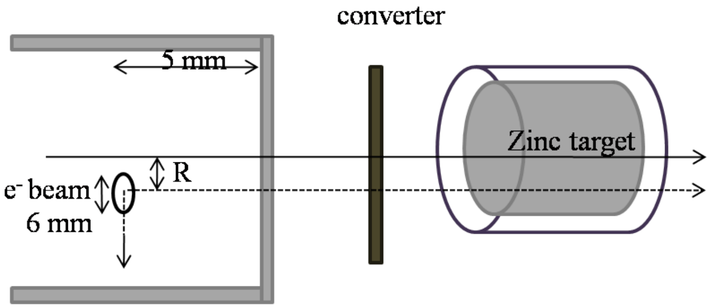

Figure 4.11: Electron beam shift in the transverse direction.

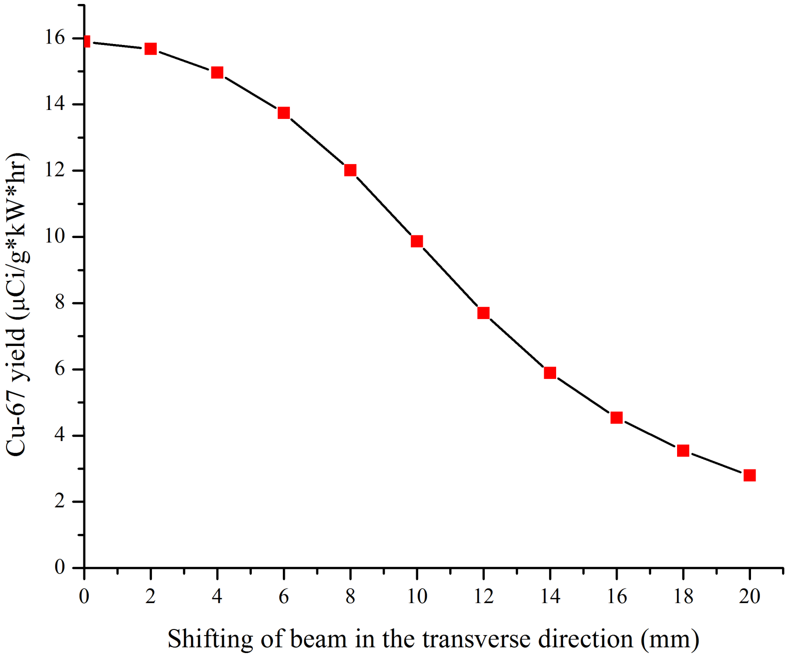

Figure 4.12: ^{67}Cu yield as a function of beam/target shift.

by 2 mm. Shifting the beam by 4 mm drops the yield by 6%. When the beam is misaligned by 7 mm, ^{67}Cu yield decreases significantly (more than 20%). This shows that when the central axis of the beam is shifted from that of the zinc target by a small distance (2 mm) compared to the size of the target (radius−8 mm), only a small fraction of forward boosted bremsstrahlung photons miss the target, hence the drop in the ^{67}Cu yield is less significant (1%). The drop in yield increases with an increase in the beam shift. However, the yield does not drop to zero even when the shift is comparable to, or larger than, the size of the target. This is because of the bremsstrahlung cone that spreads radially outward from the beam axis.

Since we do not have measured data on beam misalignment, the average offset in beam from the center of the target was approximated to be 5 mm based on experiences gained on IAC linacs in similar experiments. Similarly, the angular divergence of beam was approximated to be 3 degrees. Based on the approximated and known beam parameters (beam spot size−8 mm, and energy spread−15%) the net expected "reasonable" reduction in the ^{67}Cu production was calculated to be ≈ 20% (see Table 4.3).

Beam parameters		% reduction in ^{67}Cu production
misalignment from the target center	5 mm	8
spot size	8 mm	5
energy spread	15%	2
angular divergence	3 degree	5
Net reduction		20

Table 4.3: Expected reduction in ^{67}Cu production caused by realistic beam-quality offsets in ideal beam. The "realistic" factors are explained in the text.

The above simulations show the effects of beam quality factors on the production rate of ^{67}Cu. Depending upon the degree of deviation from the ideal beam, the loss in production can be higher. In addition to the reasons described in Section 4.1.3, especially biased beam-current measurement, the uncertainty in the beam parameters is another major potential source which may account for 20−30% discrepancy between measured and predicted production rate of ^{67}Cu.

4.2 Optimization of Bremsstrahlung Converter

To convert kinetic energy of electrons into high density photon flux, high Z materials are typically used. The physics behind the optimization of the converter material and geometry is given in Section 2.2. Our goal was to find the best possible design to maximize photon flux through the target and minimize its heating. To model the photon flux (with energy above 9.9 MeV, which is ^{68}Zn(γ, p)^{67}Cu reaction threshold) through a 2 cm × 2 cm cylindrical natural zinc target, we used MCNPX. In addition, we simulated energy deposition from both electrons and photons in a 2 cm wide (diameter) variable thicknesses converter as well as in the target. A 40 MeV 25 µA electron beam was assumed for the simulations.

Typical bremsstrahlung converter materials include tungsten, tantalum, platinum, lead, and gold. Their properties are summarized in Table 4.4. Because of its high atomic number, high density (19.3 $\frac{g}{cm^3}$), and very high melting point ($T_m = 3422\,°\mathrm{C}$), we chose tungsten as a converter material.

Figure 4.13 shows an MCNPX-visual editor screenshot of particle interactions inside a tungsten converter and zinc target. A bremsstrahlung converter stops most of the electrons striking it; however, there are always some transmitted electrons in

Element	Atomic number (Z)	Density (g/cm^3)	Melting point (°C)
Tantalum (Ta)	73	16.69	3017
Tungsten (W)	74	19.25	3422
Platinum (Pt)	78	21.45	3215
Gold (Au)	79	19.3	1064
Lead (Pb)	82	11.34	327

Table 4.4: Physical properties of some commonly used bremsstrahlung converter materials.

the emergent bremsstrahlung. These are the primary electrons for thin converters. For thick converters, most of these are secondary electrons created by high-energy bremsstrahlung photons deep inside the target. The energy distribution of photons inside the zinc target is shown in Figure 4.14. Most of incident photons have low energy.

The Monte Carlo simulation results of GDR photon flux through the target and the energy deposition in both the converter and the target are summarized in Table 4.5 and in Figure 4.15.

The maximum photon flux corresponds to a 1.5 mm thick converter, and, as the converter thickness increases, it drops gradually. Also, as the converter thickness increases the energy deposition in the converter increases, but energy deposition in the target decreases. For example, increasing the thickness of the converter from 1.5 mm to 4.5 mm caused the GDR photon flux to drop by about 18%, energy deposition in the converter rise by almost a factor of four, and the energy deposition in the target

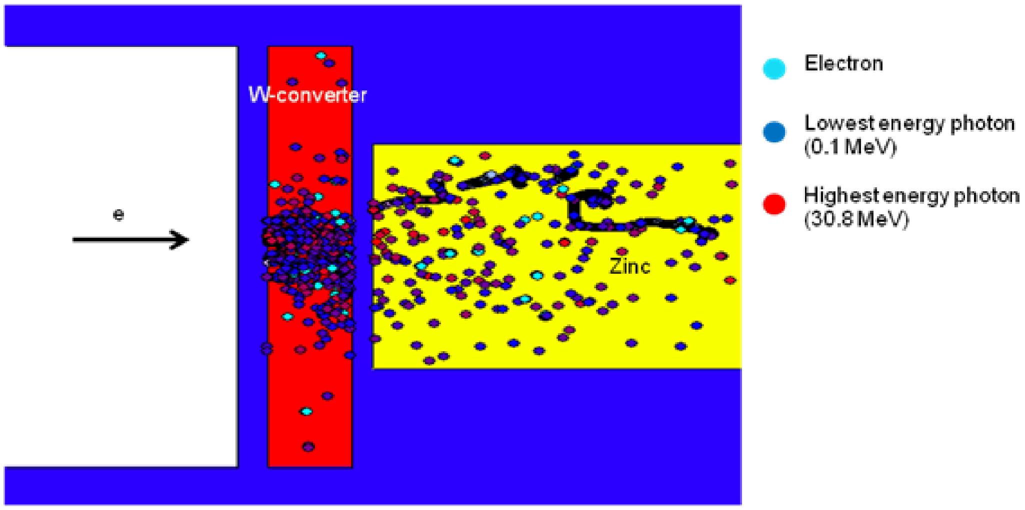

Figure 4.13: Particle interactions with the W-converter and zinc target, created by MCNPX. A dot represents the point where a particle stops inside the target.

drops by about 60%. Compared to tungsten, the melting temperature of zinc is very low (420 °C). Therefore, to avoid the potential consequences of a liquid zinc target, it is reasonable to decrease the energy deposition in the target. Considering the heating and possible melting of the target posed by large energy deposition in it, we chose to forgo some yield for lower energy deposition. As a result of this compromise, 0.45 cm was chosen as the thickness for the tungsten converter.

The average range of fast electrons in dense material can be crudely estimated by the empirical formula [35]:

$$R = \frac{E}{2\rho}\,, \tag{4.2}$$

where R is electron range in cm, E is electron energy (MeV) and ρ is material density (g/cm^3). Not shown is a unity-valued conversion constant of 1 g/(MeV-cm^2) in Eq. 4.2. Therefore, the average range of a 40 MeV electron in tungsten can be estimated

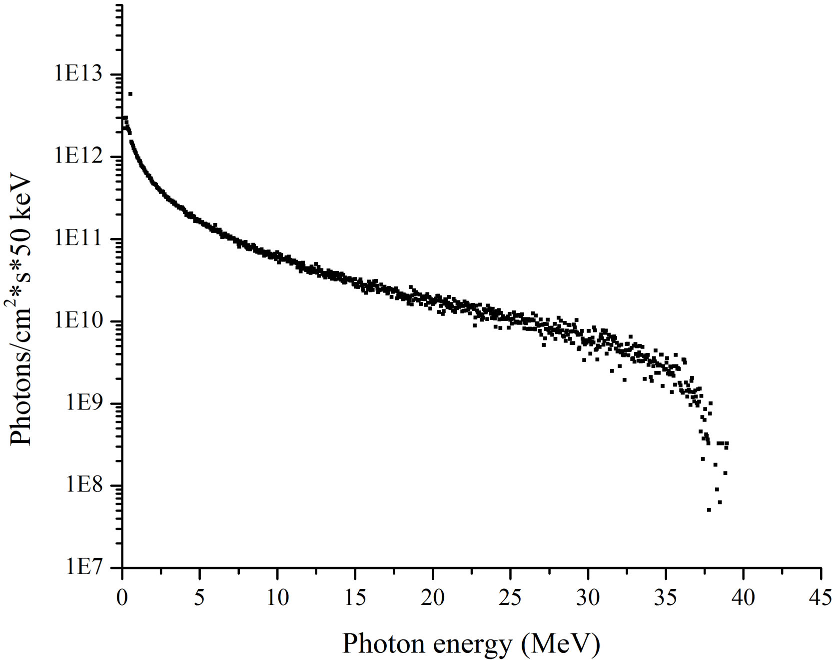

Figure 4.14: Energy distribution of the photon flux inside 2 cm x 2 cm cylindrical zinc target. Energy bins are 50 keV.

as:

$$R = \frac{40}{2 \times 19.3} = 1.03 \text{ cm} . \tag{4.3}$$

A converter thickness of 0.45 cm, therefore, corresponds to about 44% of the mean range of electrons in the tungsten. Our result falls in the range suggested by M. J. Berger et al. in [29]. They claim that the bremsstrahlung efficiency reaches a maximum dose per electron for a converter thickness between $40 - 50\%$ of the mean range of electron in the material.

In order to reduce the heat load in the converter and improve cooling efficiency, we

Converter thickness (mm)	GDR photon flux (photons/cm^2·s) at 25 μA beam current	Energy absorbed in zinc target per 40 MeV incident electron (MeV/g)	Energy absorbed in converter plate per 40 MeV incident electron (MeV/g)
0.5	2.32×10^{13}	0.470	0.430
1	2.44×10^{13}	0.422	0.463
1.5	2.48×10^{13}	0.376	0.502
2	2.47×10^{13}	0.331	0.542
2.5	2.43×10^{13}	0.288	0.579
3	2.34×10^{13}	0.248	0.607
3.5	2.24×10^{13}	0.212	0.625
4	2.12×10^{13}	0.180	0.631
4.5	2.03×10^{13}	0.154	0.628
5	1.87×10^{13}	0.132	0.618

Table 4.5: Energy deposition in a 2 cm x 2 cm W-converter and the 2 cm x 2 cm zinc target for various converter thicknesses, at 40 MeV electron beam energy and 25 μA beam current.

decided to increase its surface area by splitting one thick disc into three thinner ones. In the final design three tungsten discs, each 0.15 cm thick and 2.5 cm in diameter were spaced equally by 3 mm wide channels (as shown in Figure 3.4) and cooled with water continuously flowing through the converter assembly.

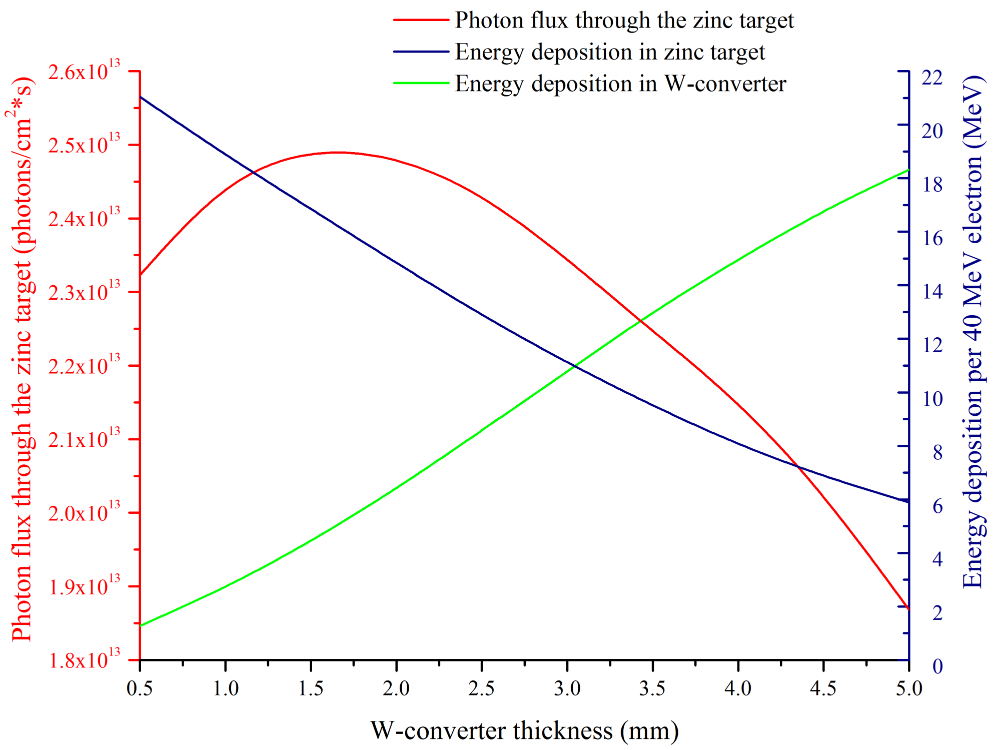

Figure 4.15: Photon flux through the zinc target, tungsten converter heating and zinc target heating as a function of the converter thickness. Note the suppressed zero on the Y-axis.

4.3 Optimization of Zinc Target Geometry

4.3.1 ^{67}Cu Distribution in the Zinc Target

The photon flux intensity decreases significantly as distance from the converter increases. This is due to the angular divergence of the bremsstrahlung photon beam. This effect is even more pronounced if photons travel through a dense medium, because of significant attenuation. Figure 4.16 shows the ^{67}Cu photo-production distribution in a 6 cm wide 6 cm long cylindrical zinc target. A 6 cm × 6 cm × 0.1

cm rectangular mesh consisting of 3600 pixels was created inside the zinc target on the electron beam axis. Photon flux through each pixel was calculated assuming a 40 MeV electron beam incident on 4.5 mm thick tungsten converter, as described in Section 4.2.1. The ^{67}Cu production rate in each pixel was found by multiplying the photon flux by the ^{68}Zn(γ, p)^{67}Cu cross section. A keyword MFACT was used followed by numerical entry 1, for linear interpolation to assess the cross section in MCNPX. The ^{67}Cu distribution was obtained by multiplying the production rate by the number of ^{68}Zn atoms in 1 mm^3 of natural zinc.

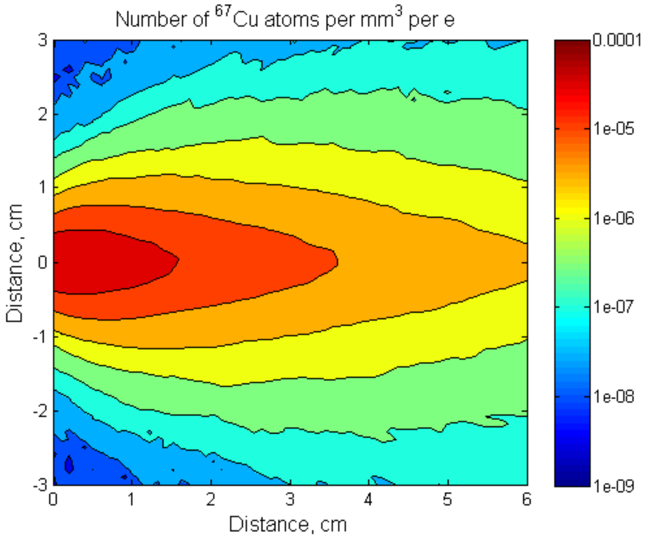

Figure 4.16: ^{67}Cu photo-production distribution in a natural zinc target.

To experimentally verify the longitudinal ^{67}Cu distribution inside the zinc target, we used 22 zinc discs (1 mm thick, 2 cm in diameter) as shown in Figure 4.17. They were put into an aluminum crucible, and placed approximately 1 cm downstream of the converter. The activation was done with a 41 MeV 2.6 μA beam (pulse width−9 μsec, repetition rate−3 Hz, and peak current−98 mA). The average beam power was 108 W. ^{67}Cu measured activities together with the results of the simulations are plotted in Figure 4.18. The experimental results were found to be $20 - 25\%$ less than predictions. The disagreement between measurement and calculation could possibly come from both uncertainties and biases in many sources. These include reaction cross section (which is a theoretical estimate), beam parameters in the simulation (which are not well known), current measurement (the IAC Faraday cup is not well-designed to accurately measure the absolute current), statistical error in simulation, and so on.

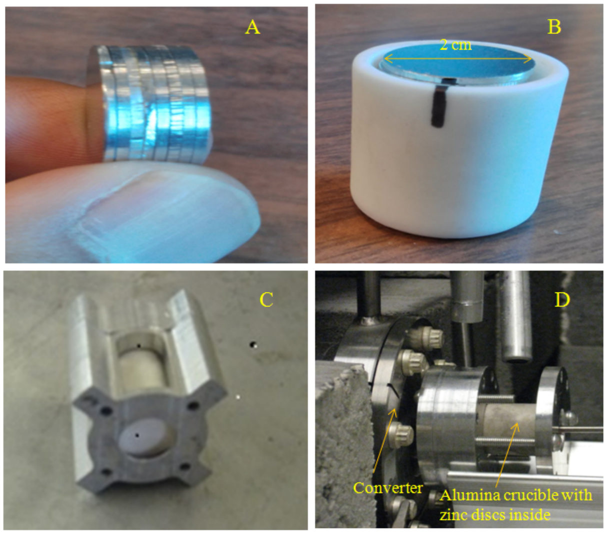

Figure 4.17: Sample preparation stages for ^{67}Cu distribution experiment showing zinc discs (A), same discs in aluminum crucible (B), crucible in the aluminum target holder (C), and the whole assembly installed next to the converter (D).

To study the radial distribution of ^{67}Cu activity, a zinc foil (0.1 mm thick, 4 cm in diameter) was activated using a 40 MeV 200 W electron beam for 30 minutes. The center of the zinc foil was marked on both sides of the foil before the activation. After the activation, radiography imaging was performed on the foil. The beam

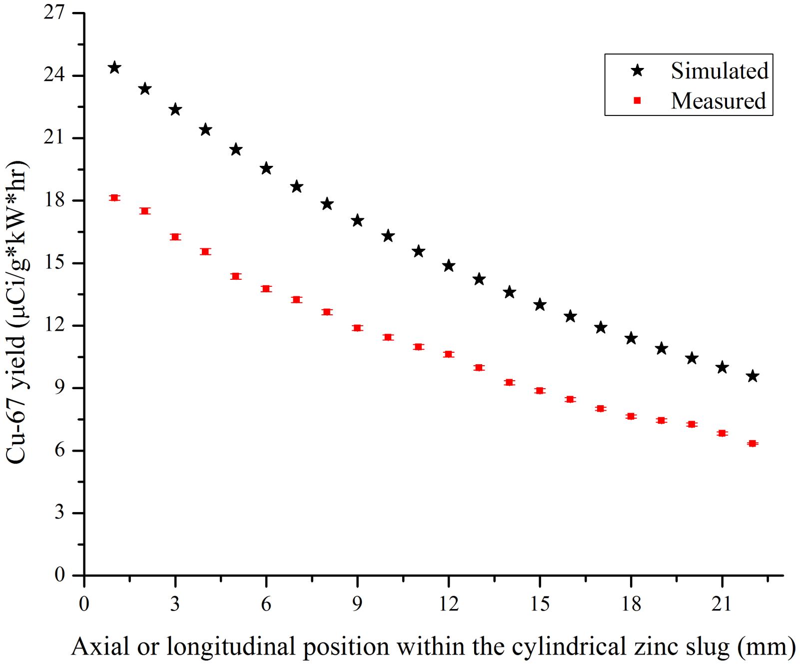

Figure 4.18: MCNPX-simulated and experimentally measured yield of ^{67}Cu in 1 mm thick, 22 zinc discs. The errors in the activity values are the measurement statistical errors as described in Section 3.4.3.

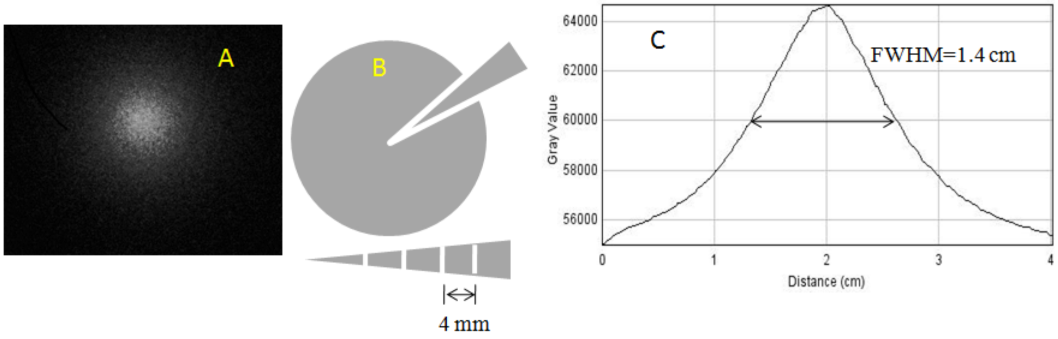

Figure 4.19: Radiographic image of irradiated zinc foil (A), small strip cut out of the zinc foil (B), and photon beam profile (C). Note that photon beam is considerably wider than electron beam due to multiple scattering and bremsstrahlung angular distribution.

spot center was found to be centered on the foil from the radiography, as shown in Figure 4.19, which confirmed good target alignment. A small strip was cut out of the foil which in turn was cut in five smaller segments each being 4 mm long (see Figure 4.19). The ^{67}Cu activity of each segment was measured and activities of disks of different radii were calculated using this data. The calculated and measured activities of zinc foils of various radii are shown in Figure 4.20. The discrepancy between calculated and measured activity is about 30% for r=4 mm, and it decreases as the target radius increases. For radius of a 2 cm the discrepancy virtually vanishes. In the simulation the electron beam was assumed to be a monoenergetic pencil beam

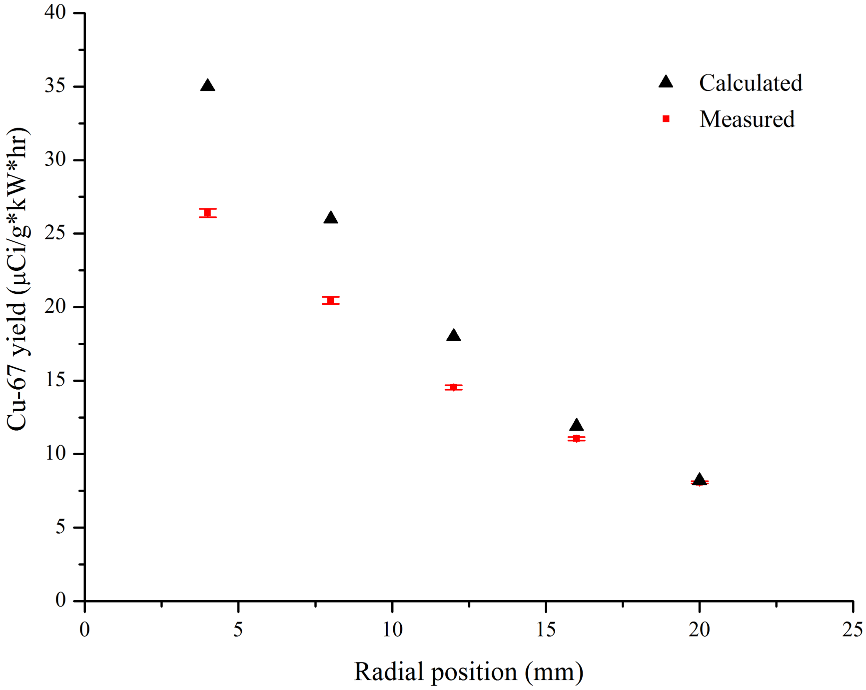

Figure 4.20: ^{67}Cu yield as a function of the zinc foil radius. Error bars represent the random (counting) statistical errors.

with zero divergence. The result displayed in Figure 4.20 suggests that the size and the angular divergence of electron beam are unlike the ideal beam assumed in the simulation and are the most likely cause of the disagreement. The result suggests that the primary beam is wider, both spatially and in angle, than assumed.

4.3.2 Optimized Cylindrical Geometry

Cylindrical symmetry of the setup and ^{67}Cu distribution in the target material imply that one should use a cylindrical shape for the zinc target. To find the optimum ratio of the radius of the target to its height, different possible dimensions of cylindrical zinc targets of different masses were studied. The radius to height ratio of the cylinder that would give the highest specific activity of ^{67}Cu was assessed by comparing the ^{67}Cu yields for a range of values of radii and heights for a given target mass. Figure 4.21 shows the ^{67}Cu activity yields as a function of the ratio of radius to height for different target masses: 40, 60, 80, and 100 gram. The optimum ratio of radius to height was found to be in the range of $0.27 - 0.29$ for all masses. To investigate the target optimization problem in more detail, we constrained our work to a 40 gram mass, which was chosen based on its ease of integration with existing IAC targets. The optimized radius and height for the 40 gram cylindrical zinc target was found to be 0.8 cm and 2.8 cm respectively, and their ratio to be 0.28.

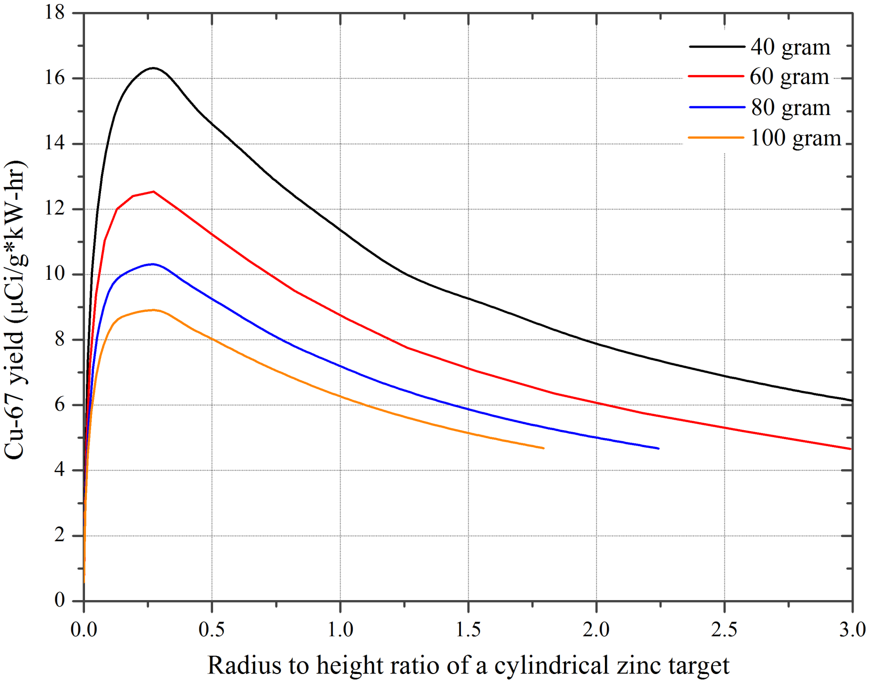

Figure 4.21: ^{67}Cu yield as a function of radius to height ratio of target zinc cylinder. Monte Carlo simulations were done for a 40 MeV electron energy of zero emittance at 1 kW beam power.

4.3.3 Optimum Geometry of Zinc Target

In Section 4.3.2 we discussed an optimum cylindrical target and found that the maximum ^{67}Cu yield corresponds to the target's ratio of radius to height being approximately 0.28. The cylindrical shape of the target was influenced by the cylindrical symmetry of the electron beam and was chosen for its simplicity. However, several other shapes with cylindrical symmetry were considered, namely semi-ellipsoid, sphere, and conical frustum. The average photon flux through these targets were simulated to find the optimal target shape which would result in a maximum ^{67}Cu yield.

Optimization of each assessed geometry consisted of finding the optimum set of the characteristic variables (base and top radii for a conical frustum, semi-principal axes for a semi-ellipsoid, and radius for a sphere). Each of the examples is explained in detail below.

Conical Frustum

The volume of a conical frustum with the base radius R, top radius r, and height h is given by:

$$V = \frac{\pi h}{3}(R^2 + r \cdot R + r^2)\,, \tag{4.4}$$

so that:

$$h = \frac{3V}{\pi(R^2 + r \cdot R + r^2)}\,. \tag{4.5}$$

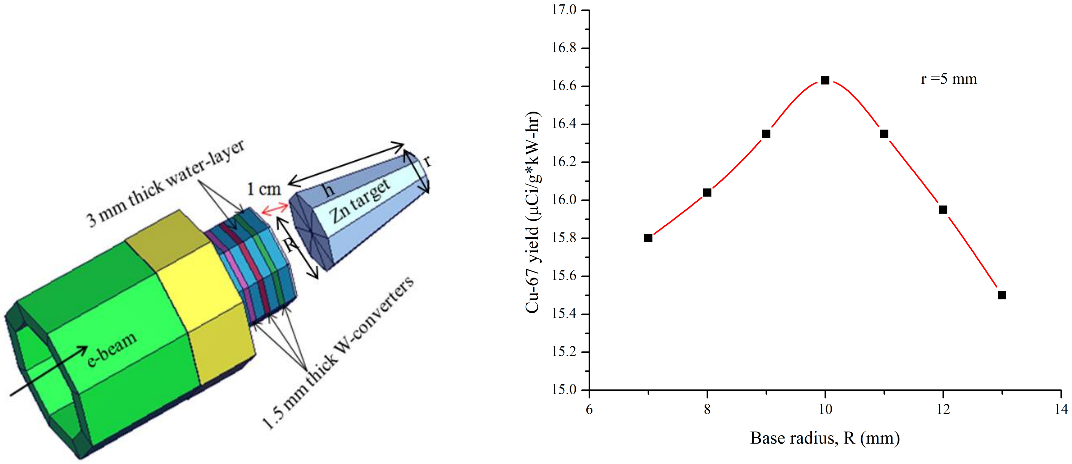

Figure 4.22: Geometry optimization of zinc target. Left: Monte Carlo simulated W-converter and conical frustum zinc target, right: ^{67}Cu yield for the conical frustum with top radius 5 mm and variable base radius and height.

Since ^{67}Cu photo-production density in the target material is higher at the base of the frustum than at the top (see Figure 4.16), changing the base radius would affect the yield more than changing the top radius. Therefore, we varied the base radius of the conical frustum for a constant volume of zinc target keeping the top radius constant. We started with 4 mm for the top radius and evaluated the ^{67}Cu yield in frustums with various base radii and heights. Similar calculations were also done for the frustums with top radii equal to 5 mm, 6 mm and 7 mm. Among all the considered dimensions, two conical frustums with R=4 mm, r=11 mm and h=29.5 mm and, with R=5 mm, r=10 mm and h=30.5 mm gave the similar yields as shown in Table 4.6. A conical frustum resulting maximum yield is shown in Figure 4.22.

Top radius, r (mm)	Base radius, R (mm)	Height, h (mm)	^{67}Cu Yield (μCi/g·kW·hr)
4	10	34.2	16.56
	11	29.5	16.61
	12	25.7	16.32
5	9	34.5	16.35
	10	**30.5**	**16.63**
	11	26.6	16.35
6	8	36.1	16.11
	9	31.2	16.38
	10	27.3	15.97
7	7	36.3	15.76
	8	31.6	16.04
	9	27.7	15.21

Table 4.6: Yield calculation for conical frusta with various top and base radii corresponding to zinc mass of 40 gram.

Semi-ellipsoid

The volume of a semi-ellipsoid with semi principal axes a and b, and vertical axis (the axis of symmetry) c, is given by:

$$V = \frac{2}{3}\pi abc\,. \tag{4.6}$$

Due to the cylindrical symmetry of the electron beam, we assumed one of the semi principal axes to be equal to vertical axis (b=c), giving the target the oblate shape. Thus, Eq. 4.6 can be rewritten as:

$$V = \frac{2}{3}\pi ab^2\,. \tag{4.7}$$

The ^{67}Cu yield was calculated for a set of semi-ellipsoids with constant volume, but different values of a and b to find the geometry corresponding to the maximum yield. Among evaluated dimensions a semi-ellipsoid with the semi major axis $a = 33$ mm, and semi minor axis $b = 9$ mm gave the highest ^{67}Cu yield as shown in Table 4.7.

Sphere

^{67}Cu yield for a zinc sphere of volume 5.6 cm^3 (40 gram) placed about 1 cm away from the water cooled tungsten converter was calculated (see Figure 4.24) and compared with other geometries.

The results of the simulations for the spherical target together with optimum

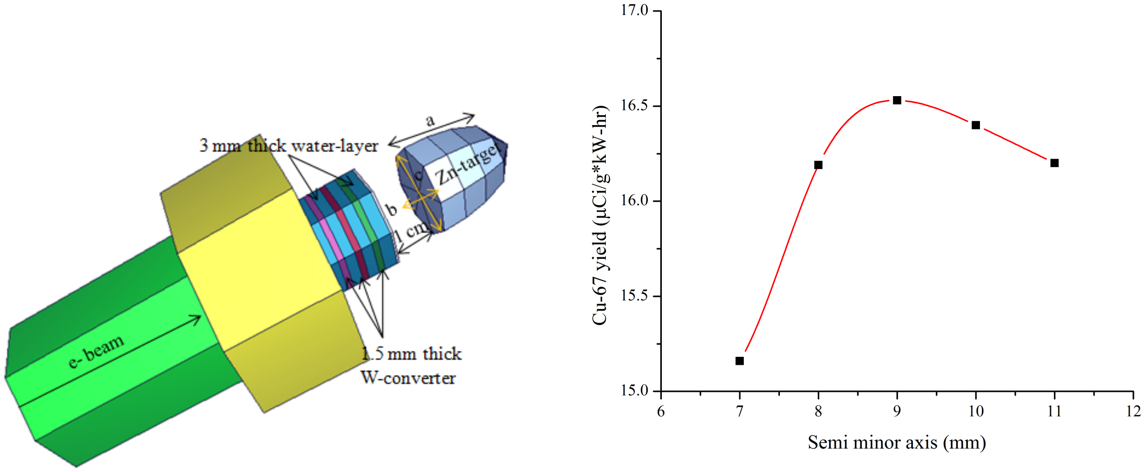

Figure 4.23: Geometry optimization of zinc target. Left: Monte Carlo simulated W-converter and semi-ellipsoidal zinc target geometry, right: ^{67}Cu yield for the semi-ellipsoid with semi minor and vertical axis equal to 9 mm and variable semi major axis.

Semi major axis (mm)	Semi minor axis (mm)	^{67}Cu Yield (μCi/g·kW·hr)
54.5	7	15.2
41.2	8	16.2
33	**9**	**16.5**
26.7	10	16.4
22	11	16.2

Table 4.7: Yield calculation for semi-ellipsoids with different values of semi-major and semi-minor axes corresponding to zinc mass of 40 gram.

dimensions of cylinder, semi-ellipsoid, conical frustum, and sphere are listed in Table 4.8. Among all the geometries sampled, the optimized conical frustum and semi-ellipsoid resulted in about $3-4\%$ higher yields than that of the cylinder, while the

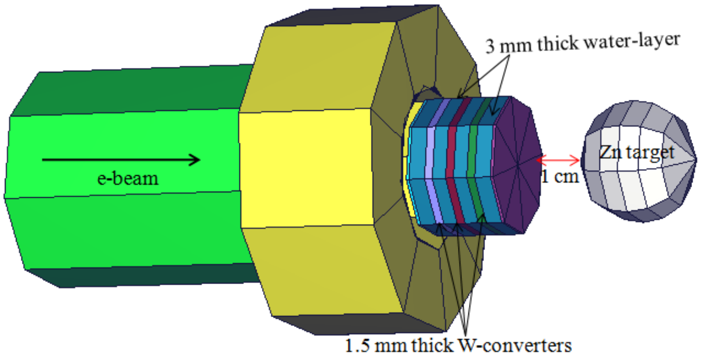

Figure 4.24: Monte Carlo simulated tungsten converter and spherical zinc target.

spherical target produced 7% less yield than that of the cylinder. Taking into account the engineering cost and difficulties in making complex targets and target holders, the increase in the yield was considered to be insignificant. Therefore, the cylinder was chosen as the optimum target shape.

Target shape	Characteristic variables	^{67}Cu activity (μCi/g·kW·hr)
Cylinder	radius: 8 mm height: 28 mm	16
Conical frustum	base radius: 10 mm top radius: 5 mm height: 30.5 mm	16.6
Semi-ellipsoid	semi-major axis: 33 mm semi-minor axis: 9 mm vertical axis: 9 mm	16.5
Sphere	radius: 11 mm	14.9

Table 4.8: ^{67}Cu specific activities for the optimized zinc target geometries.

A Similar study of target optimization for ^{67}Cu photo-production was done by Sean Howard et al. [57] using an analytical approach. Howard et al. found for a

40 gram zinc target, that a semi-ellipsoid was the highest ^{67}Cu yield resulting target shape over all the geometries sampled. The optimized semi-ellipsoid and conical frustum resulted in 2% higher yield than that of the cylinder in Howard's work which is close to our result. We found the optimal radius to height ratio for cylindrical target (40 − 100 gram) in the range of 0.27 − 0.29, which is slightly higher than that reported in Howard's work (0.2 − 0.23). Differences in the simulation set-up and the geometry of electron beam, which results in different photon distribution in the target and hence the ^{67}Cu distribution, may explain the difference between two results. Also, our simulation used 4.5 mm thick water-cooled tungsten converter to produce bremsstrahlung photons from a 40 MeV cylindrical electron beam, whereas a Gaussian shaped electron beam along with thinner (2 mm) converter was used in Sean's calculation.

Depending on the desired specific activity and the target material purity, the mass of the target should be chosen carefully since the specific activity of the resulting radioisotope is affected by the target mass. In this study, target optimization was done for 40 grams of zinc. Similar optimization procedures can be done for other masses as well.

4.4 High Power Issues

4.4.1 MCNPX Simulation of Energy Deposition

It was shown in Section 4.1.2 that optimum operating parameters of the IAC high power linac for photo-production of ^{67}Cu are 36.4 MeV and 134 μA, which corresponds to 4.8 kW of beam power. Dealing with such a high power electron beam may easily result in melting or even vaporizing the converter and/or the target, so careful thermal analysis of the system is absolutely necessary. The energy deposition tally (f6) in MCNPX code was used to calculate energy deposited by both electrons and photons in the water cooled tungsten converter (0.45 cm thick and 2.5 cm wide) and the zinc target. Although we simulated the energy deposition in a 40 gram zinc target, experimentally the desired mass of 40 gram was not obtained because of experimental limitations during melting of zinc and slug making process which produced a 41 gram zinc target. Therefore, thermal analysis was conducted for a 41 gram zinc target. A 41 gram zinc target inside an alumina crucible was placed 1 cm away from the converter as shown in Figure 3.4. A significant portion of the electron beam power ($\approx$ 65%) was deposited in the converter assembly. While about 14% of the power was deposited in the zinc target, the remaining 21% of the power was deposited in cooling water, air, and other end station components. Electrons contribute to nearly 70% of the target heating. Table 4.9 summarizes the distribution of deposited power in the three plates of tungsten converter, alumina crucible, and zinc target.

The mesh tally of MCNPX for energy deposition was used to calculate the radial

	1st W-plate	2nd W-plate	3rd W-plate	Alumina crucible	Zinc target
Absorbed energy density (MeV/g)	0.491	0.727	0.627	0.079	0.142
Power (%)	17	25	22	3	14

Table 4.9: Energy deposition in the components of the target assembly.

distribution of energy deposition in the zinc target, which is 1.6 cm × 2.8 cm (see Figure 4.25). To estimate the axial distribution of energy deposition, we calculated the energy deposited into thin slices of zinc target (see Figure 4.26). The front layer of the target is subjected to higher power density due to stopping of short range electrons.

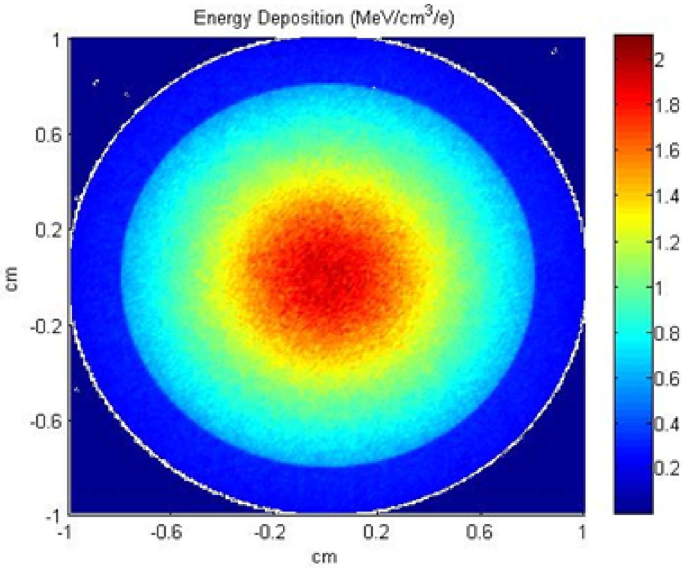

Figure 4.25: Energy deposition on the zinc target's front face from a 40 MeV electron beam.

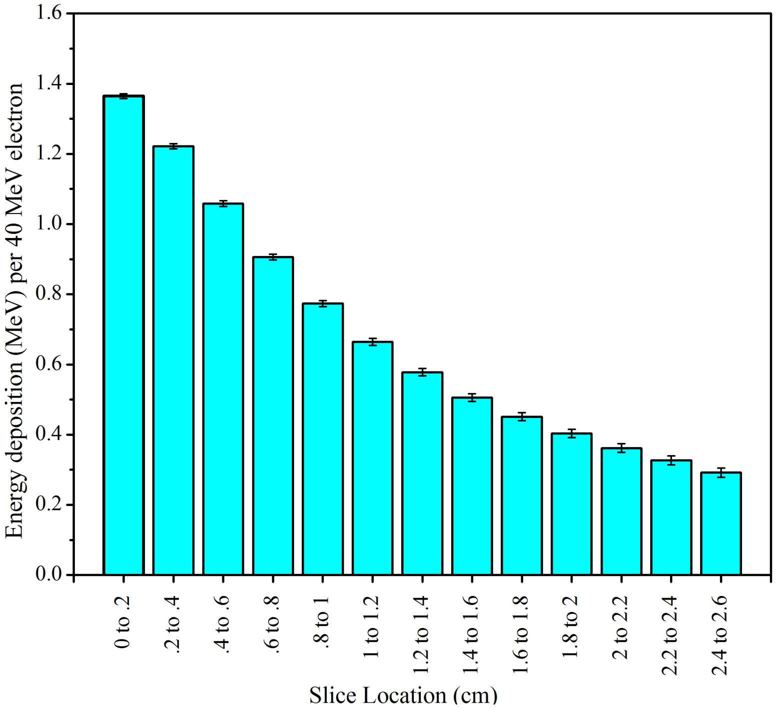

Figure 4.26: Axial distribution of the zinc target heating from a 40 MeV electron beam.

4.4.2 Zinc Target Temperature Measurement and Validation of MCNPX Heat Deposition

To verify the results of the energy deposition simulations, the temperature of the zinc target was measured using a K-type thermocouple inserted into the zinc target during the irradiation as described in Section 3.5. Because the temperature measurement took two days to complete, data were taken on two different days with two different electron beam "tunes." Although we wished to study the energy deposition in the converter and the target unit at 40 MeV to be consistent with our simulations, because of the limitation of the IAC linac, the desired energy was only approximately obtained for all measurements. Therefore, temperature measurements were done for beam energies in the range of $40 - 44$ MeV at different beam powers ranging from 1 kW to 3 kW, rather than single 40 MeV electron beam energy of the simulation. A summary of the electron beam parameters for the experiments is given in Table 4.10. The screenshot of the LabVIEW program shows the real-time measurement of zinc target temperature (see Figure 4.27).

Energy (MeV)	Peak current (mA)	Rep. rate (Hz)	Pulse width (μs)	Average current (μA)	Average power (kW)
44	47	120	4.12	23.3	1.02
40	48.5	180	3.16	27.6	1.10
44	47	120	6.18	34.8	1.53
44	47	120	8.24	46.5	2.04
40	50	180	6.31	56.8	2.27
41	49	180	7.89	69.6	2.85
42	49	180	8.2	72.3	3.04

Table 4.10: Beam parameters in temperature measurement experiment. Note the beam energy variations due to linac tuning limitations.

A simple heat loss calculation was done using the initial rate of temperature drop immediately after the beam was turned off. Thermodynamic steady state is reached when the rate of heat gained by the target is equal to the heat lost by it. For

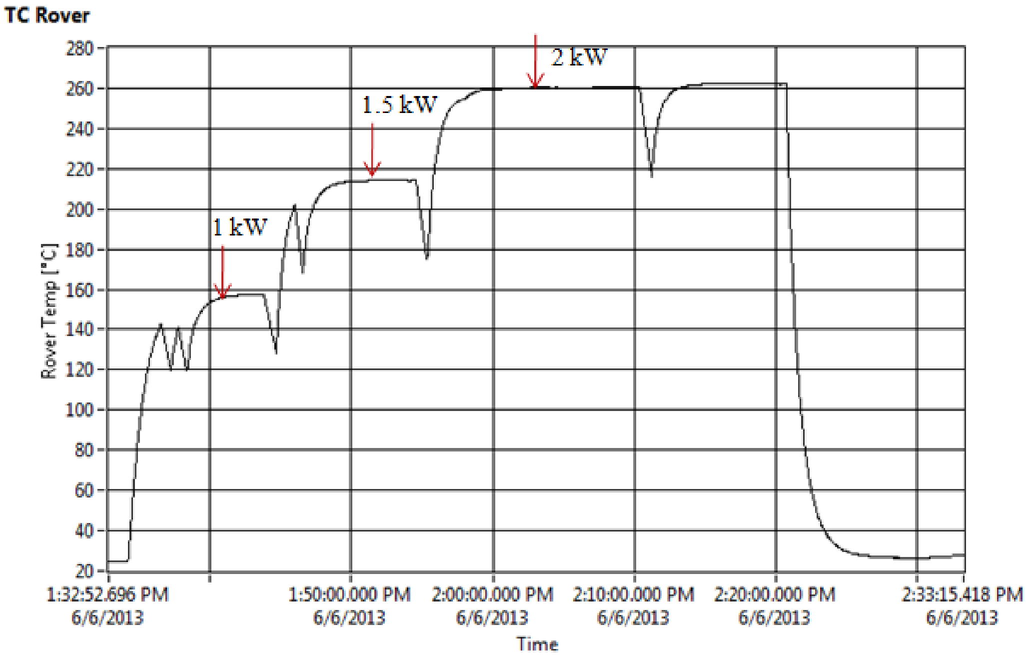

Figure 4.27: Temperature profile of zinc target at various beam powers for a 44 MeV electron beam.

the following calculations we considered our target to include both the zinc and the alumina crucible, since alumina has high thermal conductivity and there was good thermal contact between zinc and alumina. At the thermal steady state, the rate of net amount of heat received by the target from the beam is equal to the heat lost to the surrounding. This is given by:

$$\dot{Q}_{in} = \dot{Q}_{out} = mC\frac{\Delta T}{\Delta t} \ , \tag{4.8}$$

$$\dot{Q}_{out} = (\dot{Q}_{out})_{zn} + (\dot{Q}_{out})_{Al_2O_3} = m_{zn}C_{zn}\frac{\Delta T_{zn}}{\Delta t} + m_{Al_2O_3}C_{Al_2O_3}\frac{\Delta T_{Al_2O_3}}{\Delta t} \ , \tag{4.9}$$

where m, C, and ΔT are mass, specific heat capacity and change in temperature of the system respectively. During one second after the beam was turned off, the

T_{air} (°C)	$T_{surrounding}$ (°C)	Alumina surface area (m^2)	$\overline{h}$ ($W/m^2{\cdot}K$)	σ ($W/m^2 \cdot K^4$)	ϵ
23	25	2.95×10^{-3}	316	5.67×10^{-8}	0.9

Table 4.11: Physical parameters used to calculate the temperature of alumina crucible.

temperature changed from 262 °C to 254 °C so that $\Delta T = 8\,°\text{C}$. The specific heat capacity for zinc and alumina (aluminum oxide) are 0.39 J/g/°C and 0.88 J/g/°C respectively. For a 41 gram of zinc and 19 gram of alumina, Eq. 4.9 gives:

$$\dot{Q}_{out} = 41 \times 0.39 \times (262 - 254) + 19 \times 0.88 \times (262 - 254) = 262 \text{ J/second} \ . \quad (4.10)$$

Hence, the rate of energy deposition in the target is 262 J/second.

The fraction of the total beam power absorbed by the target (including zinc and alumina) is estimated as:

$$\frac{262 \text{ Watt}}{\text{total beam power}} = \frac{262 \text{ Watt}}{2000 \text{ Watt}} = 0.13 = 13\% \ . \quad (4.11)$$

This estimate is close to MCNPX simulated value (see Table 4.9, 17% power deposition in zinc target and alumina). The simulated power deposition in the target unit is 23% higher than that estimated from measured temperature. This is consistent with our earlier photo-production results. Therefore, it appears that beam divergence, beam emittance, beam energy spread, and misalignment of beam all work to reduce the power deposition in the target. This also supports the claim that we made earlier that these beam-quality offsets in electron beam from the ideal beam is an important cause for the consistent discrepancy between our prediction and measurements.

Using Eq. 3.13, the temperature of alumina crucible ($T_{alumina}$) was calculated for various beam powers, assuming that 13% of the total accelerator power was deposited in the target assembly. The physical parameters used to solve the equation are tabulated in Table 4.11. Using the value of $T_{alumina}$ found from Eq. 3.13, the zinc temperature was calculated using Eq. 3.17 for different beam powers. The estimated zinc target temperatures are compared with the experimentally determined temperature, which are measured at various electron beam powers and are in good agreement (see Table 4.12 and Figure 4.28).

Total beam power (Watt)	Calculated $T_{alumina}$ (°C)	Calculated T_{zinc} (°C) $P_{in} = 13\% P_{total}$	Measured T_{zinc} (°C)	$\delta T_{zinc} = [\frac{T_{meas.} - T_{calc.}}{T_{calc.}}] \times 100\%$
1022	161	168	157 ± 2	7
1103	171	178	169 ± 2	5
1531	228	237	214 ± 2	10
2044	278	290	262 ± 3	10
2271	309	322	310 ± 3	4
2873	375	392	372 ± 4	5
3038	395	413	390 ± 4	6

Table 4.12: Calculated and measured temperature of alumina and zinc target at various electron beam powers.

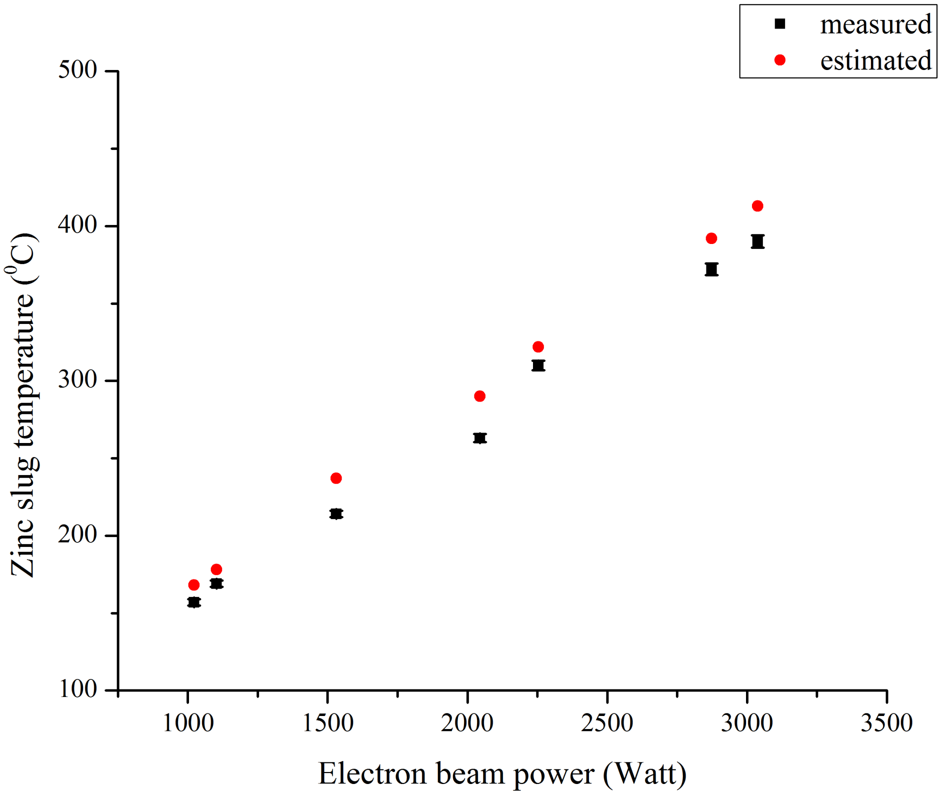

Figure 4.28: Calculated and measured zinc target temperatures at various beam powers and electron beam energies as listed in Table 4.10. The error bars in temperatures represent the systematic errors of the thermocouple used for the temperature measurement.

4.4.3 Radiolytic Corrosion

To address radiolytic corrosion caused by high power electron beams, we irradiated Al, W, Ta, Cu, Zn, Ti and stainless steel foils in water as described in Section 3.6. After the irradiation the foils were removed, and the remaining water was collected. To measure the amount of metal ions in the water, the PAA technique was used. Unfortunately, the resulting spectrum did not give any conclusive results because all of the results were less than detection limits. The net counts under the desired energy peaks from the materials of interest are summarized in the Table 4.13. Water was found to contain some trace amounts of aluminum and tungsten, however, the statistical uncertainty was very poor. The relative uncertainty in the net counts under each energy peak exceeds 100% for all elements except for tungsten and aluminum $(60-70\%)$.

Radiolytic corrosion of metals depends upon various parameters such as radiation dose, temperature, time of exposure, pH of water, impurities in water, water solubility of metals, and so on [55]. The poor statistics in this study may be caused by relatively low radiation dose and a short time of exposure. With increased radiation dose and exposure time, one can increase the corrosion rate. The sensitivity of the detection instrument, a high purity germanium detector, is also important to detect such low concentrations.

In addition to the photon activation analysis, a surface study on irradiated foils by SEM, and a quantitative analysis of aqueous water solution by Inductively Coupled

Material	Expected nuclide	Energy, keV	Counts in mixed sample	Counts in blank sample	Net counts
Tantalum	Ta-180m	93	2244 ± 259	2262 ± 180	-18 ± 315
Titanium	Sc-47	159	-23 ± 143	126 ± 144	-149 ± 203
Zinc	Cu-67	185	1572 ± 211	1736 ± 113	-164 ± 239
St. steel	Cr-51	320	-158 ± 143	-10 ± 142	-148 ± 201
Tungsten	W-187	686	128 ± 37	-7 ± 74	135 ± 83
Copper	Cu-64	1345.8	28 ± 20	7 ± 39	21 ± 44
Aluminum	Na-24	1369	55 ± 21	-16 ± 40	71 ± 45

Table 4.13: Net counts for different energies corresponding to different isotopes of interest in mixed and blank samples.

Plasma-Mass Spectrometry (ICP-MS) were also done to measure the radiolytic corrosion of metal foils. Neither of these methods showed measurable radiolytic corrosion of metals of interest. SEM-EDS and ICP-MS results can be found in Appendix E.

Chapter 5

Conclusion

5.1 Optimization of Electron Energy and Current, Converter Thickness and the Zinc Target Geometry

Based on the MCNPX simulations and experiments performed at the IAC, we found the optimum electron energy and current for the IAC electron linear accelerator that is used in the photo-production of ^{67}Cu to be 36.4 ± 0.2 MeV and 134 ± 1 μA respectively. Optimization of photonuclear production strongly depends on the beam parameters of the electron linac one is working with. Thus we have optimized for a particular linac at the IAC, however, this optimization procedure can be generalized and adapted to any electron linac.

To maximize the bremsstrahlung photon yield while minimizing the zinc target heating, we chose tungsten as a converter and varied its thickness. The final converter design consisted of three 1.5 mm thick discs separated by 3 mm thick water channels.

To find the optimum shape of the zinc target, we investigated four different geometries: cylinder, semi-ellipsoid, sphere, and conical frustum. We chose to use a cylindrical geometry for practical purposes. The chosen geometry resulting in the highest ^{67}Cu yield was found to be a cylinder with a radius of 0.8 cm and a height of 2.8 cm. This target yielded 16 μCi/(g·kW·hr) of ^{67}Cu. The simulated yield was compared to experimentally measured ^{67}Cu yield for similar experimental set up using slightly different target dimension with the 0.9 cm radius and 2.2 cm height. The experimentally measured ^{67}Cu activity was 12.4 $\pm$ 0.6 μCi/(g·kW·hr), with the error representing the random (counting) statistical uncertainty as described in Section 3.4.3. The measured activity is $\sim$ 20% less than the MCNPX simulated value 15.8 μCi/(g·kW·hr).

Our result on ^{67}Cu yield was compared with the values reported by two other laboratories namely, Kharkov Institute of Physics and Technology (KIPT) and Argonne National Laboratory (ANL), where similar production method have been developed for the ^{67}Cu production. For a 40 MeV photon beam the production rate of ^{67}Cu at KIPT is 15.8 μCi/(g·kW·hr) [58], whereas, ANL has reported 16.6 μCi/(g·kW·hr) [13].

Our value for ^{67}Cu yield is less than that reported by KIPT. Differences in converter design, electron beam-quality and experimental set up can explain this disagreement. We used a 4.5 mm thick tungsten plate as bremsstrahlung converter, whereas KIPT used 4 mm thick tantalum plates. Also, in our work the target holder added extra distance, thus reducing photon flux, between the converter unit and the target. This extra distance is absent in the set up used at KIPT. The details on the ANL's experimental set up were not found in the literature for comparison, presumably due to intellectual property issues.

Comparison of photonuclear production of ^{67}Cu with other production methods is not trivial because each method is different in terms of physics limitations and cost trade-offs. Direct comparisons of these various techniques are problematic because the physics and engineering limitations of each technique are quite different. Positive ion production techniques, for example, are limited to thin targets and modest power because of the high stopping power of positive ions and the high power-density in the target. In contrast, photon-production techniques are limited by lower cross section, but much higher power beams and much greater target thickness are possible. Fast neutron reactor-based production poses yet another set of constraints.

A practical comparison of different production methods would be in terms of yield per cost. However, the cost analysis for various production schemes for ^{67}Cu production mentioned in this work is not available in the literature and is beyond the scope of this work.

The experimentally measured values for the activity of ^{67}Cu in all our experiments were $20 - 30\%$ less than the MCNPX-predicted values. Several contributing sources were investigated for this discrepancy between calculated and measured activity. In the simulations, the electron beam was assumed to be a monoenergetic pencil beam with uniform spatial distribution of electrons. The emittance and the energy spread of electrons in the beam were assumed to be zero. In practice, conventional copper linacs can never produce beams that are close to such ideal electron beams. The ideal electron beam in the simulation over-predicts photon flux through the target. The uncertainty in the theoretically modeled exclusive (γ, p) cross section is another contributor to the uncertainty of the calculated activity of ^{67}Cu. Some degree of target misalignment along the beam line axis during real measurements is also unavoidable. In addition, current measured at the converter was assumed to be the actual beam current during irradiation. However, the Faraday cup not only counts electrons that are actually present in the bunch, but also some of the scattered and backscattered electrons as well as sputtered electrons [59]. The Faraday cup also loses "out-scattered" electrons. This leads to uncertainty in the beam current measurement, and hence to the measured activity per current. We conclude that collective uncertainties and biases in these results are consistent with effects from non-ideal beams and their measurement.

5.2 High Power Issues

Our experiments on temperature of the zinc target during irradiation at various beam powers demonstrated that about 13% of total beam power is deposited into the zinc target. Under air cooling the target is "safe" ($\approx$ 400 °C $<$ melting temperature, 420 °C) up to 3 kW of beam power. However, increasing the beam power above 3 kW will require a more efficient cooling scheme of the target (for example, water cooling) to prevent the target from melting.

Numerous research groups [60] have shown that ionizing radiation causes material corrosion via production of reactive intermediates of water radiolysis. The effect of corrosion from high radiation fields was not observed in these experiments at few kilowatt power levels. We have performed PAA of the water in which metal foils were submerged while irradiated. The resulting gamma spectra did not show metal dissolution in the water. Therefore, radiation induced corrosion product was not observed in this study, most likely due to low power levels.

5.3 Future Work

Our study showed that the quality of an electron beam is one of the important factors determining the radioisotope yield. Therefore, real-time beam monitoring is extremely important to maintain high photon flux and, as a result, provide high ^{67}Cu yield. Better beam instrumentation and diagnostics of the beam properties (beam size, emittance, divergence, energy spread, position, etc.) would minimize the uncertainty in ^{67}Cu yield. Introduction of essential diagnostic tools in the IAC linac is left for further study.

Other accelerators which can result in higher quality electron beams such as, microtrons with very small energy resolution and superconducting linacs, can be used as well.

For future work on radiation induced corrosion, an alternative experiment should be performed to measure the effects of corrosion even at low power electron beams.

Such an experiment would include irradiation of metal foils with an actively-circulating water loop and a resin ion-exchange column to trap the ions dissolved via radiolytic reactions. Water radiolysis products depend highly on water quality such as pH, purity, oxygen level, and temperature. A careful study on the effect of these parameters on radiolytic corrosion is important to understand the possible long-term degradation of accelerator components and construction materials and should be included in future investigation.

Bibliography

[1] Exploring the table of isotopes. Lawrence Berkeley National Laboratory. http://ie.lbl.gov/education/isotopes.htm.

[2] National nuclear data center. Brookhaven National Laboratory. http://www.nndc.bnl.gov/chart/reCenter.jsp?z=52&n=76.

[3] Kahn, Jeffery. From radioisotopes to medical imaging, history of nuclear medicine written at berkeley. Technical report, Berkeley Lab Science Articles Archive, Sep 1996.

[4] Nuclear medicine & molecular imaging. Technical report, Society of Nuclear Medicine & Molecular Imaging, May 2012.

[5] Radioisotopes in medicine. World Nuclear Association, October 2011.

[6] Lodge, M. A, H. Braess, and F. Mahmoud. Developments in nuclear cardiology: Transition from single photon emission computed tomography to positron emission tomography. *J. invasive cardiology*, 17(9):146–150, Sep 2005.

[7] Radioisotopes in medicine. Technical report, World Nuclear Association, March 2014.

[8] Fast facts about radiation therapy. Technical report, American Society for Therapeutic Radiology and Oncology (ASTRO), Nov 2012.

[9] Zirkle, R. E. Biological effectiveness of alpha particles as a function of ion concentration produced in their paths. *Am. J. Cancer*, 23(3):558–567, March 1935.

[10] University of California. Radionuclide data sheet [copper].

[11] Shen, S., G. L. DeNardo, S. J. DeNardo, Q. Salako, G. Morris, D. Banks, and A. Yuan. Dosimetric evaluation of copper-64 in copper-67-2it-bat-lym-1 for radioimmunotherapy. *J Nucl. Med.*, 37(1):146–150, Jan 1996.

[12] Press, O. W., J. P Leonard, B. Coiffier, R. Levy, and J. Timmerman. Immunotherapy of non-hodgkin's lymphomas. *Hematology*, 221-240 2001. American Society of Hematology Education Program.

[13] Ehst, David, Delbert L. Bowers. Methods for making and processing metal targets for producing Cu-67 radioisotope for medical application. *U.S Patent 12/462,099*, Sep 2013.

[14] National Academy of Sciences. *Advancing Nuclear Medicine Through Innovation.* National Academies Press, 2007.

[15] NSAC. Isotopes for the nation's future: A long range plan. Final report, second of two 2008 NSAC charges on the isotope development and production for research and applications program, 2009.

[16] Use of isotopes in research, medicine, and industry. Nuclear Energy Research Advisory Committee (NERAC) Final Report, Apr 2009.

[17] Nuclear monitor. *A publication of World Information Service on Energy (WISE) and the Nuclear Information & Resource service (NIRS).*

[18] Ayzatskiy, N. I., N. P. Dikiy, A. N. Dovbnya, Yu. V. Lyashko, V. I. Nikiforov, B. I. Shramenko, A. Eh. Tenishev, A. V. Torgovkin, and V. L. Uvarov. Comparison of Cu-67 production at cyclotron and electron accelerator. In *Proceeding of Cyclotrons and Their Applications*, volume 18, pages 243–245, 2007.

[19] Dovbnya, A. N., V. I. Nikiforov, V. L. Uvarov, and V. F. Zhyglo. Optimization of electron linac operating conditions for photonuclear isotope production. In *Proceedings of EPAC08*, volume 8, pages 1308–1310, 2008.

[20] Bennett R. G., J. D. Christian, and D. A. Petti. A system of ^{99m}Tc production based on distributed electron accelerators and thermal separation. *Nuclear Technology*, 126:102–122, 1999.

[21] Starovoitova, Valeriia N., Lali Tchelidze, and Douglas P. Wells. Production of medical radioisotopes with linear accelerators. *Applied Radiation and Isotopes*, 85:39–44, 2014.

[22] Melville, Graeme, and Barry J. Allen. Cyclotron and linac production of Ac-225. *Applied Radiation and Isotopes*, 67(4):549–555, 2009.

[23] Mcgee, T., C. L. Rao, G. B. Saha, and L. Yaffe. Nuclear interactions of Sc-45 and Zn-68 with protons of medium energy. *J. Nuc. Phys.*, 150:11, 1970.

[24] Levkovskij, V. N. Activation cross section nuclides of average masses (A=40−100) by protons and alpha-particles with average energies (E=10−50 mev). 1991.

[25] Skakun, Ye., and S. M. Qaim. Excitation function of the ^{64}Ni(α, p)^{67}Cu reaction for production of ^{67}cu. *Applied Radiation and Isotopes*, 60, 2004.

[26] Kielan, D., and A. Marcinkowski. Cross sections for the (n, p) reaction on zinc isotopes in terms of the novel multistep compound reaction model. *Zeitschrift fuer Physik A*, 352, 1995.

[27] *IAEA, Handbook of Photonuclear Data for Application: cross sections and spectra.* IAEA-TECDOC-1178, March 2000.

[28] Habs, D., and U. Koster. Production of medical radioisotopes with high specific activity in photonuclear reactions with gamma beams of high intensity and large brilliance. *Appl. Phys. B*, 103:501–519, 2011.

[29] Berger, Martin. J., and Stephen. M. Seltzer. Bremsstrahlung and photoneutrons from thick tungsten and tantalum targets. *Phys. Rev. C*, 2:621–631, August 1970.

[30] Segebade, Christian, Hans-Peter Weise, and George J. Lutz. *Photon Activation Analysis*. Walter de Gruyter, 1988.

[31] Fultz, S. C., and B. L. Berman. Measurements of the giant dipole resonance with monoenergetic photons. *Reviews of Modern Physics*, 47(3):887–904, 1975.

[32] Beil, H., R. Bergere, P. Carlos, A. Lepretre, A. De Miniac, and A. Veyssiere. A study of the photoneutron contribution to the giant dipole resonance in doubly even mo isotopes. *Nuclear Physics*, 227(9):427, 1974.

[33] J. S. Levinger. The high energy nuclear photoeffect. *Phys. Rev.*, 84:43–51, Oct 1951.

[34] Tavares, O. A. P., M. L. Terranova. Nuclear photoabsorption by quasi-deuterons and an updated evaluation of Levinger's constant. Centro Brasileiro de Pesquisas Fisicas - CBPF/CNPq, 1991.

[35] Glenn F. Knoll. *Radiation detection and measurement*. John Wiley & Sons, 2010.

[36] Randy William Tompot. Engineering design of electron accelerator targets for the commercial production of isotopes. Master thesis, Massachusetts Institute of Technology, Feb 1997.

[37] Kirk D Hagen. *Heat Transfer with Applications*. Prentice Hall, 1999.

[38] N. B Vargafik. *Tables of the Thermo-physical Properties of Liquids and Gases*. John Wiley & Son, 2nd edition, 1975.

[39] Čuba, Václav, Viliam Múčka, and Milan Pospíšil. *Advances in Nuclear Fuel.* InTech., 2012.

[40] Cecal, Al., M. Goanta, M. Palamaru, T. Stoicescu, K. Popa, A. Paraschivescu, and V. Anita. Use of some oxides in radiolytical decomposition of water. *Radiat. Phys. Chem.*, 62:333–336, Oct 2001.

[41] Lukashenko, M. L., S. A. Kabakchi, O. P. Arkhipov, and A. I. Milaev. Characteristic features of the radiolysis of water irradiated under strictly fixed conditions and under conditions varying over a small range. *Atomic Energy*, 87:496–504, July 1999.

[42] X-5 Monte Carlo Team. *MCNP—A general Monte Carlo N-particle transport code User Manual, version 5*, volume I. Los Alamos National Laboratory, 2003.

[43] White, M. C., R. C. Little, M. B. Chadwick, P. G. Young, and R. E. MacFarlane. Photonuclear physics in radiation transport—ii: Implementation. *Nucl. Sci. Eng.*, 144:174–176, 2003.

[44] X-5 Monte Carlo Team. *MCNP — A General Monte Carlo N-Particle Transport Code User Manual, Version 5*, volume II. Los Alamos National Laboratory, revised edition 2008.

[45] Olsher, Richard H. A practical look at monte carlo variance reduction methods in radiation shielding. *Nuclear Engineering and Technology*, 38(3):225–230, Apr. 2006.

[46] The radiation heat transfer emissivity coefficient of some common materials as aluminum, brass, glass and many more. http://www.engineeringtoolbox.com/emissivity-coefficients-d_447.html.

[47] Temperature, density, specific heat, thermal conductivity, expansion coefficient, kinematic viscosity and Prandtl's number for temperatures ranging -150$-$400 ^0C. http://www.engineeringtoolbox.com/thermal-conductivity-d_429.html.

[48] Capacity of compressed air pipelines-applied pressure ranging 5$-$250 psi (0.5$-$17 bar). *The Engineering tool box*.

[49] Timothy John Gardner. Separation of Cu-67 from Zn-68 by sublimation and methods for recovery of Zn-68. Master thesis, Idaho State University, 2012.

[50] Debertin, K., and R.G. Helmer. *Gamma and X-ray Spectrometry With Semiconductor Detectors*. North-Holland, 1988.

[51] Molki, Arman. Simple demonstration of the seebeck effect. *Science Education Review*, 9(3):103–107, 2010.

[52] Chang, Byoung-Yong, and Su-Moon Park. Electrochemical impedance spectroscopy. *Annu. Rev. Anal. Chem*, 3:207–229, Feb 2010.

[53] Goldstein, Joseph. *Scanning Electron Microscopy and X-ray Microanalysis*. New York : Kluwer Academic/Plenum Publishers, 2002.

[54] Pinte, G., M. A. R. Veado, and A. H. Oliveira. Comparison of neutron activation analysis and ICP-MS used for river water pollution control. *J. Hydrobiologia*, 373:61–73, 1998.

[55] Roth, Olivia, and Jay A. LaVerne. Effect of pH on H_2O_2 production in the radiolysis of water. *J. Phys. Chem. A*, 115:700–708, Jan 2011.

[56] Sawkey, D. L., B. A. Faddegon. Determination of electron energy, spectral width, and beam divergence at the exit window for clinical megavoltage X-ray beams. *Med Phys*, 36(3):698–707, Mar. 2009.

[57] Howard, S., V. N. Starovoitova. Target optimization for the photonuclear production of radioisotopes. *Appl. Radiat. Isot.*, 96:162–167, Feb. 2015.

[58] Aizatsky, N. I., N. P. Diky, A. N. Dovbnya, D. Ehst, V. I. Nikiforov. Mo-99 and Cu-67 isotopes yields under production conditions of NSC KIPT electron accelerator KUT-30. *Problems of atomic science and technology*, Series: Nuclear Physics Investigations (53):140–144, 2010.

[59] Strehl, Peter. *Beam Instrrumentation and Diagnostics*. Springer, 2006.

[60] Lillard, R. S. Influence of water radiolysis products on passive film formation and reduction in a mixed radiation environment. *Corros. Eng. Sci. Techn.*, 38:1920–196, 2003.

Appendices

Appendix A

MCNPX input file for photon flux and energy deposition simulation

MCNPX Visual Editor Version X_24E Created on: Thursday, May 02, 2013 at 13:00

Cells

1 0 1 $ outside the universe

2 0 -2 3 -9 $ beam pipe

3 204 -0.001225 -1 #2 #5 #4 $ surrounding air

4 272 -19.3 -2 4 -5 $ tungsten converter

5 273 -7.14 -6 7 -8 $ zinc target

Surfaces

1 so 50

2 cx 1.5

3 px -11

4 px 0

5 px 0.25

6 cx 0.8

7 px 0.35

8 px 3.15

9 px -0.15

```
mode n p e
```

Materials

```
m204 7014.70c -0.755636 $MAT204 8016.70c -0.231475 18036.70c -3.9e-005 18038.70c
-8e-006 18040.70c -0.012842 m273 30064. -0.486 $MAT273 30066. -0.28 30067. -0.04
30068. -0.118 m272 74182.70c -0.260586 $MAT272 74183.70c -0.142269 74184.70c
-0.307531 74186.70c -0.289615
```

cell importance

```
imp:n 0 1 3r $ 1, 14
imp:p 0 1 3r $ 1, 14
imp:e 0 1 3r $ 1, 14
```

Energy cutoff

```
cut:e j 0.1
cut:p j 0.1
Physics phys:e 5j 10 j 0
phys:p 3j 1
```

Source define

```
sdef pos -9 0 0 axs 1 0 0 rad d1 ext d2 dir 1.0 vec 1 0 0 par e erg=40
si1 0 0.3
sp1 -21 1
si2 0 8.5
sp2 -21 0
e0 0.1 797i 40
```

Tally

```
f4:p 14 $ photon flux
f6:p,e 14 $ photon and electron deposition
print
prdmp j 1e6 1 3 1e6
nps 10E6
```

Appendix B

MCNPX input file for photon flux in rectangular mesh

```
MCNPX Visual Editor Version X_24E
Cells
1 0 1
2 0 -2 7 -23
3 208 -2.69 2 -3 7 -5
4 498 -4.54 -3 5 -6
5 486 -7.92 2 -9 6 -8
6 204 -0.001225 -1 #2 #3 #4 #5 #7 #8 #9 #10 #11 #12 #13 #14 #15 #16 #17 #18
7 498 -4.54 -4 8 -10
8 272 -19.3 -4 11 -12
9 272 -19.3 -4 13 -14
10 208 -2.69 2 -9 8 -18
11 208 -2.69 4 -2 8 -18
12 274 -4 (19 -20 -16 ):(15 -16 20 -21 ):(21 -26 -16 )
13 514 -1 10 -17 -4 #17 #8 #9
14 273 -7.14 -15 20 -21
```

15 514 -1 22 -5 -2

16 498 -4.54 23 -22 -2

17 272 -19.3 -4 24 -25

18 498 -4.54 17 -18 -4

Surfaces

1 so 50

2 cx 1.5

3 cx 2

4 cx 1.25

5 px 0

6 px 0.005

7 px -11

8 px 2.545

9 cx 3

10 px 2.595

11 px 3.299

12 px 3.449

13 px 3.703

14 px 3.853

15 cx 1

16 cx 1.2

17 px 4.153

18 px 4.203

19 px 5.203

20 px 5.403

21 px 7.403

22 px -0.43307

23 px -0.43807

24 px 2.895

25 px 3.045

```
26 px 7.603
mode n p e
```

Materials

```
m204 7014.70c -0.755636
8016.70c -0.231475 18036.70c -3.9e-005 18038.70c -8e-006 18040.70c -0.012842
m208 13027.70c -1
m498 22046.70c -0.076779 22047.70c -0.071584 22048.70c -0.739078 22049.70c -0.056228
22050.70c -0.056332
m494 73181.70c -1
m486 24050.70c -0.00793 24052.70c -0.159032 24053.70c -0.018378 24054.70c -0.004661
25055.70c -0.02 26054.70c -0.039605 26056.70c -0.638496 26057.70c -0.01488 26058.70c
-0.002019 28058.70c -0.064024 28060.70c -0.025321 28061.70c -0.001115 28062.70c -
0.003599 28064.70c -0.000942
m273 30064. -0.486 30066. -0.28 30067. -0.04 30068. -0.118
m274 13027. 2 8016. 3
m236 6000.70c -1
m514 1001.70c -0.111894 8016.70c -0.888106
m272 74182.70c -0.260586 74183.70c -0.142269 74184.70c -0.307531 74186.70c -0.289615
```

cell importance

```
imp:n 0 1 16r $ 1, 18
imp:p 0 1 16r $ 1, 18
imp:e 0 1 16r $ 1, 18
```

Energy cutoff

```
cut:e j 0.1
cut:p j 0.1
phys:e 5j 10 j 0
phys:p 3j 1
```

Source define

```
sdef pos -9 0 0 axs 1 0 0 rad d1 ext d2 dir 1.0 vec 1 0 0 par e erg=40
si1 0 0.3
```

```
sp1 -21 1
si2 0 8.5
sp2 -21 0
e0 0.1 797i 40
print
prdmp j 1e6 1 3 1e6
nps 1e6
```

Mesh tally

```
tmesh
rmesh1:p flux
cora1 5.403 199i 7.403
corb1 -0.005 0.005
corc1 -1 199i 1
endmd
```

Appendix C

MATLAB program for yield calculation

```
clear all;
load bm.txt;
load cs.txt;
% bm.txt is a bremsstrahlung photon spectrum. It is a text file with two columns.
% The first column is a photon energy in MeV, the second column is number of photons
% per cm2̂ per electron and per 50 keV energy interval.
% cs.txt is Lorentz-fitted cross section data of a reaction of interest. It is a text file
% with two columns. The first column is a photon energy in MeV (has to be the same as the first
% column of bm.txt), the second column - cross section in mbarns.
% Note: All calculations are done for 30 MeV electron beam, 1 kW of beam % power.
% Parameters (target parameters) (need to be entered every time program is compiled)
% Below enter target mass in grams;
M = 1;
% Below enter target average atomic mass in amu;
```

m = 95.94;

% Below enter natural abundance of an isotope of interest;

abundance = 0.0963;

% Below enter a half-life of the isotope of interest in hours:

halflife = 66;

% Below enter irradiation time in hours:

t = 15;

% Activity calculation is conducted below (don’t edit)

% Average number of electrons per second is calculated and stored in variable N (for 1 kW of beam power and 30 MeV electron beam):

$N = (1 * 10^{-3}/(30 * 1.6 * 10^{-19}))$;

% Photon flux - cross section overlap integral I (in s^{-1}) is calculated and stored in variable I:

I = 0;

for i = 1:length(bm),

I = I + bm(i,2)*cs(i,2);

end

$I = I * N * 10^{-27}$;

% Total number of the isotope of interest in the target is calculated and stored in variable Tot;

Tot = M * abundance / $(m * 1.6605 * 10^{-24})$;

% Production rate (in s^{-1}) is calculated and stored in variable R:

R = Tot * I;

% Activity obtained in uCi:

A = (R * (1 - exp(-log(2)* t / halflife))) / (37000);

sprintf(’Activity obtained is %g uCi/(g kW %g hours)’, A, t)

Appendix D

Inductive loop used to measure in-line current.

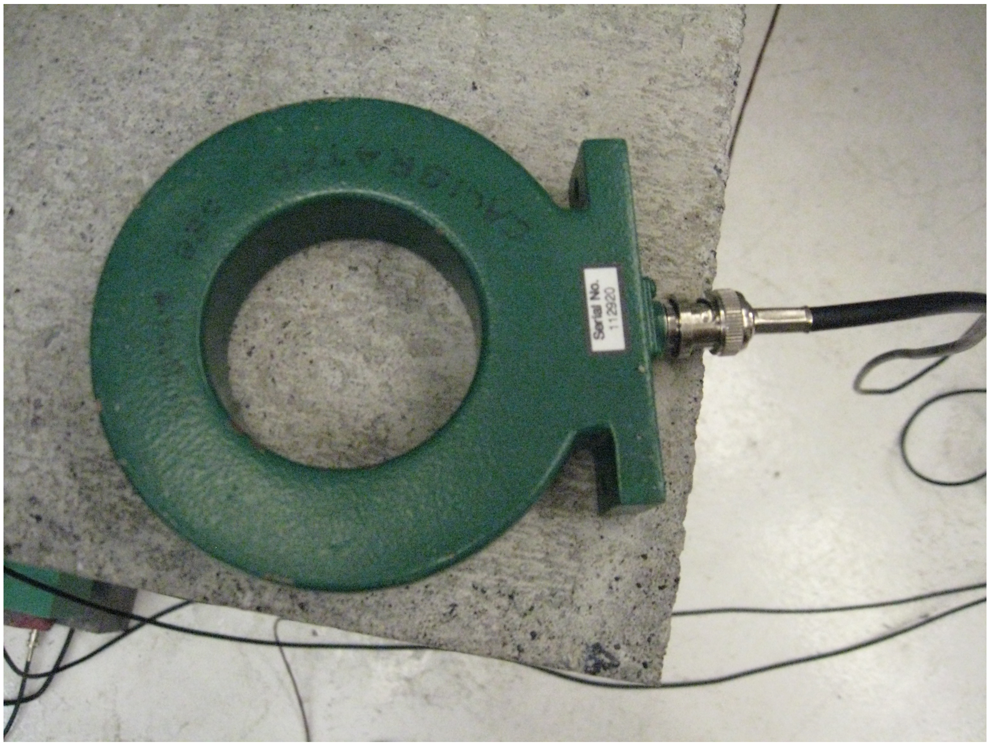

Appendix E

Corrosion measurement on metals using SEM/EDS technique.

Seven different metal foils (W, Ta, Ti, Al, Cu, Zn, St. Steel) were wrapped partially in aluminum foil and submerged in an aluminum tank full of water in such a way that the foils did not touch each other. The tank was irradiated with bremsstrahlung from a 330 Watt beam power electron beam for an hour, using a 38 MeV beam energy with the pulse width−1.5 μsec, rep. rate−82 Hz, and peak current−70 mA. Another set of identical non-irradiated foils were prepared. Both radioactive and non-radioactive foils were imaged using JSM-6610LV Scanning Electron Microscope. Only two sample results are presented here.

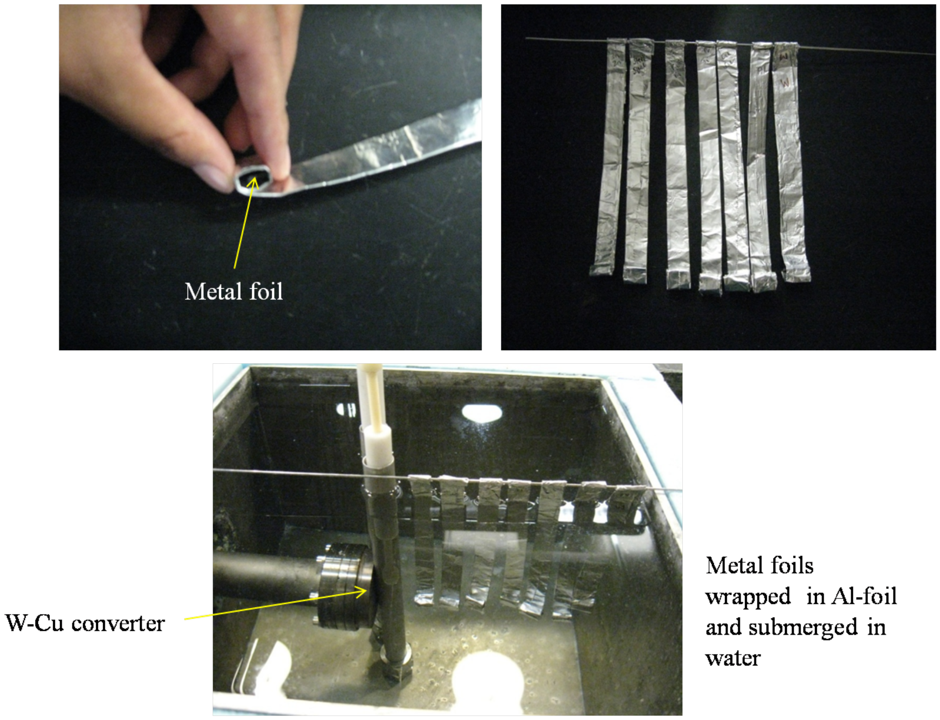

Figure E.1: Activation setup for corrosion experiment of metal foils.

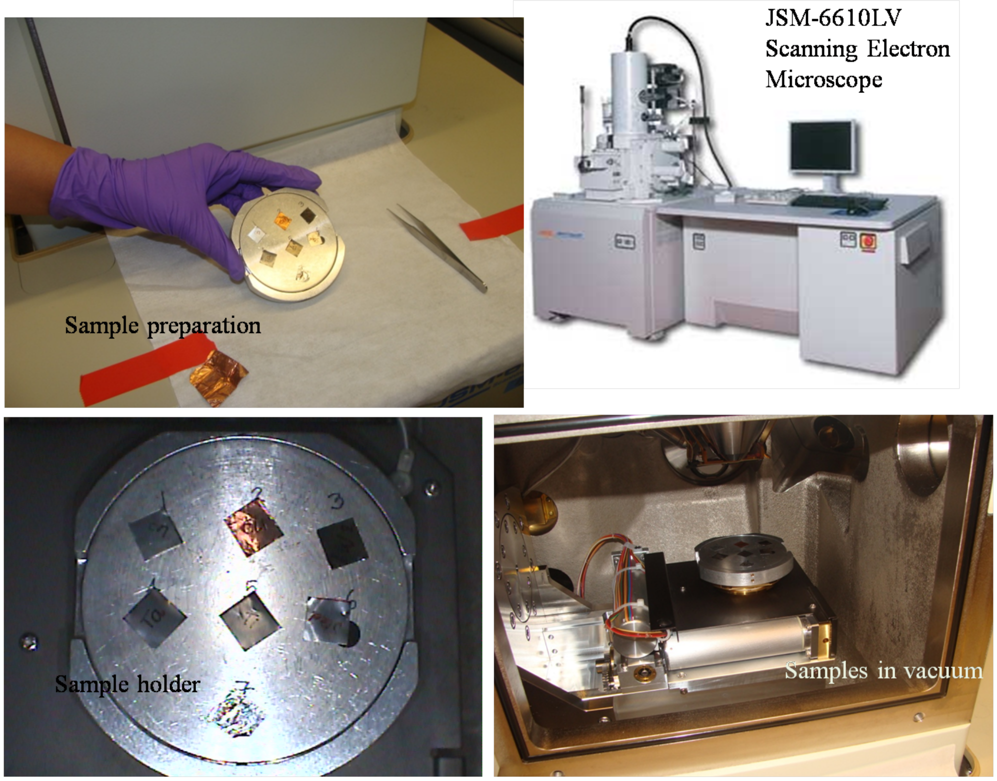

Figure E.2: Scanning Electron Microscopy (SEM) imaging setup.

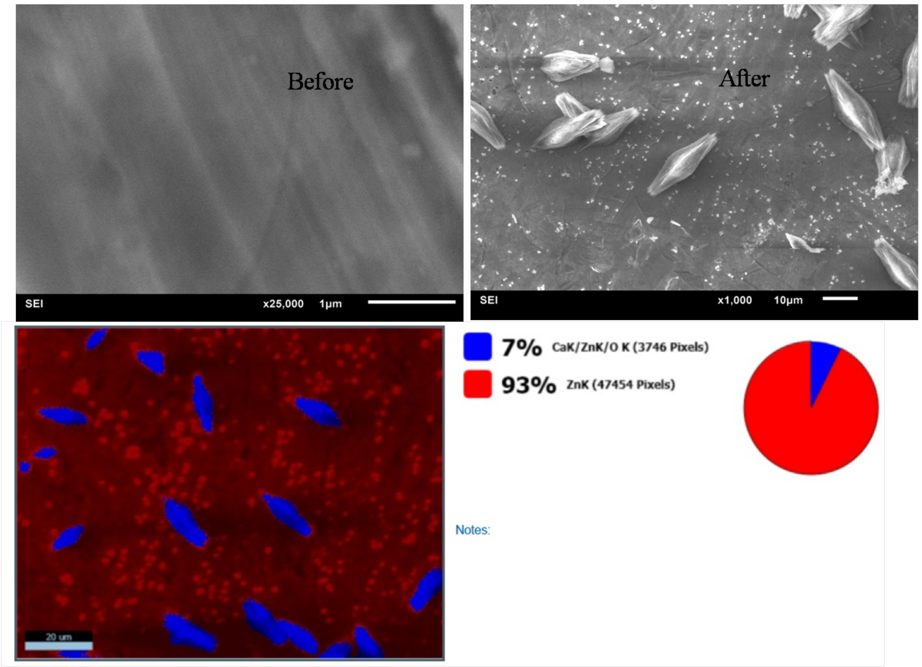

Figure E.3: SEM images of zinc foil before and after the irradiation (top two figures), EDS analysis of irradiated zinc foil.

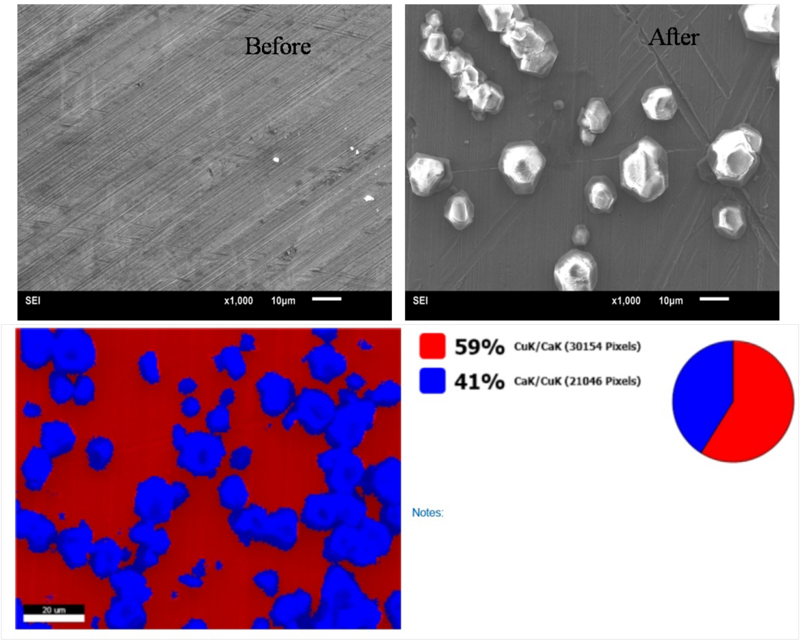

Figure E.4: SEM images of copper foil before and after the irradiation (top two figures), EDS analysis of irradiated copper foil.

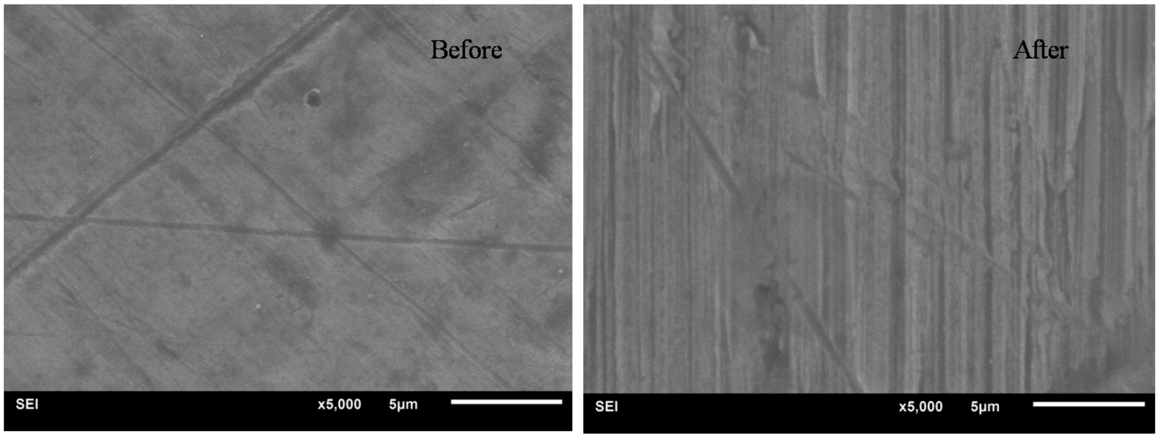

Figure E.5: SEM images of Aluminum foil before and after the irradiation (no trace of oxide layer was observed).